INTRODUCTION

This report summarizes the work done by members of the Tracking Study Group. The group's efforts were focused in two main directions. First, we have considered the design of a central tracking chamber suitable for studies of e^+e^- collisions at 100 GeV. Solid angle, momentum resolution, and segmentation requirements were studied in conjunction with members of the Parameters Group. In addition, we have considered the limitations imposed by current drift chamber techniques. The second effort was to explore the possibility of studying and identifying short-lived particles in very high resolution vertex detectors. We have considered the physics accessible to such devices, resolution and segmentation requirements, and looked into several techniques for doing such measurements.

Accordingly, we have divided this report into two sections. The first discusses the design of a central tracking chamber; the second, secondary vertex detection at the SLC.

During the course of the workshop, group members shared expertise, experience, and ideas on topics ranging from tracking algorithms to emulsion techniques and solid state particle detection. It has not been possible to include all these efforts here; but we acknowledge the usefulness of these discussions, the pleasure they brought, and the general education they have provided.

CENTRAL TRACKING CHAMBER FOR S. L. C.

I. Introduction

We discuss in this report the constraints imposed on the design of a central tracking device, of the drift chamber variety, by the energy and event characteristics at the Z^o as well as by the drift process itself. The discussion has been strongly influenced by the detectors which presently exist, although no attempt has been made to provide a comprehensive summary on this subject.[1]

II. Dimensions for a Central Tracking Chamber

A. Requirements on Momentum Resolution

The dimensions of a central tracking chamber will be determined by the requirements of momentum resolution and pattern recognition. The cost one can tolerate for the system surrounding the tracking device provides a further limitation. To look at the momentum resolution required we have examined several physics topics likely to require good momentum resolution. For high momentum tracks we parametrize the momentum resolution as $\frac{\Delta p_\perp}{p_\perp{}^2} = f$, for a track crossing all layers of the detector.

1. $Z^o \to \mu^+\mu^-$ (Muon Asymmetry).[2,3]

A measurement of the muon asymmetry as well as the τ lepton polarization will check the axial and vector couplings of the Z^o to leptons, as discussed in the parameters section of the SLC report. We assume that $\Delta p/p = 50\%$, for each muon, is the minimum requirement for telling the charge-which is all that is needed for this measurement. This gives a requirement:

$$\frac{\Delta p}{p^2} = 1\%, \text{ or } f = 1\% \text{ (units will always be GeV}^{-1}\text{)}.$$

For a chamber of length = diameter the above figure will be good only over about 70% of the solid angle. To extend this to about 90% of the solid angle, allowing for the degradation in resolution because of both the shorter track length and the fewer number of measurements, requires:

$$f = .3\%.$$

Note, the number of events is increased by about 50% by increasing the solid angle coverage from 70% to 90%.

2. $\underline{\tau \rightarrow \pi\nu}$ (Tau Polarization Measurement).[4]

The slope of the pion spectrum in this decay provides an excellent measurement of the deviation from zero of the vector coupling to the Z^o for the τ (and thereby the Weinberg Angle). The spectrum is expected to look as follows:

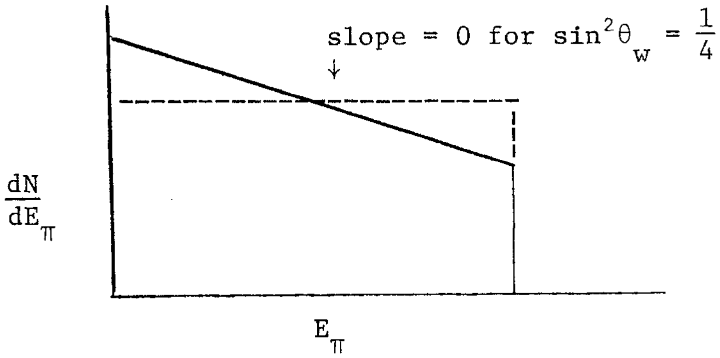

To estimate our ability to determine $\sin^2\theta_W$, we look at <x> the mean of the fractional momentum distribution, where $x = p_\pi/P_{max}$. $\langle x\rangle \simeq .5 + 1.3 \quad (\sin^2\theta_W - \frac{1}{4})$ in the Standard Model. For an event sample containing N events there are three effects which limit the <x> measurement.

(a) Statistical Fluctuations: $\sigma_{\langle x\rangle} = \frac{1}{\sqrt{12N}}$ for a flat distribution.

(b) Fluctuations due to the momentum measuring error: $\sigma_{\langle x\rangle} = \frac{f\ P_{max}}{\sqrt{5N}}$.

(c) Systematic shifts in <x> because the momentum error isn't Gaussian. This is nearly independent of $\sin^2\theta_W$ and is correctable by a Monte Carlo simulation. Requiring (b) << (a) gives $f \lesssim .5\%$. For this case one can expect to measure $\sin^2\theta_W$ with an error of .005 in one year of running (30,000 τ pairs).

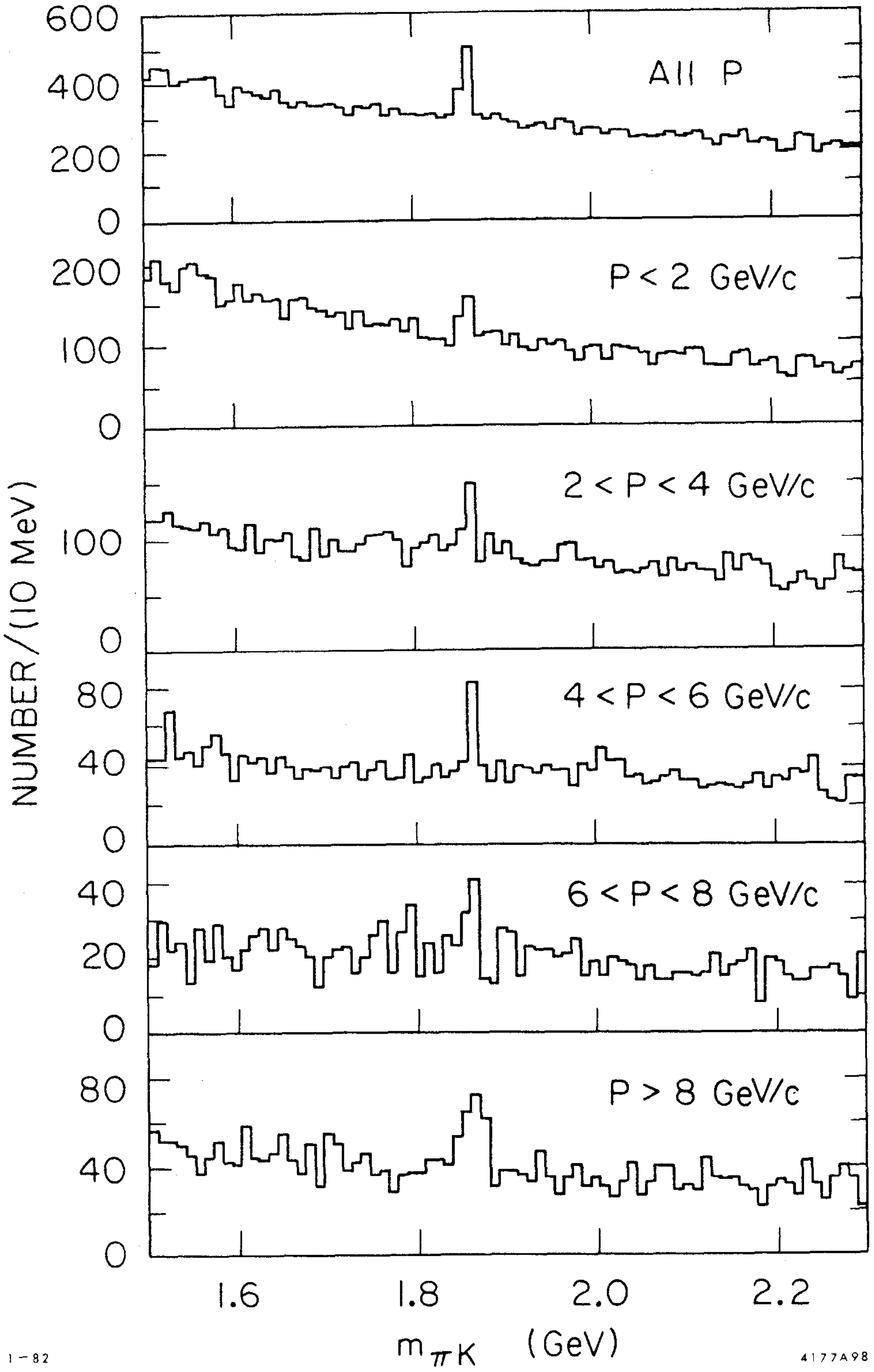

Fig. 1(a). Reconstructed invariant mass of all charged πK combinations for a momentum resolution given by f = 0.1% and assuming perfect particle identification. Event sample is 5,000 hadronic events.

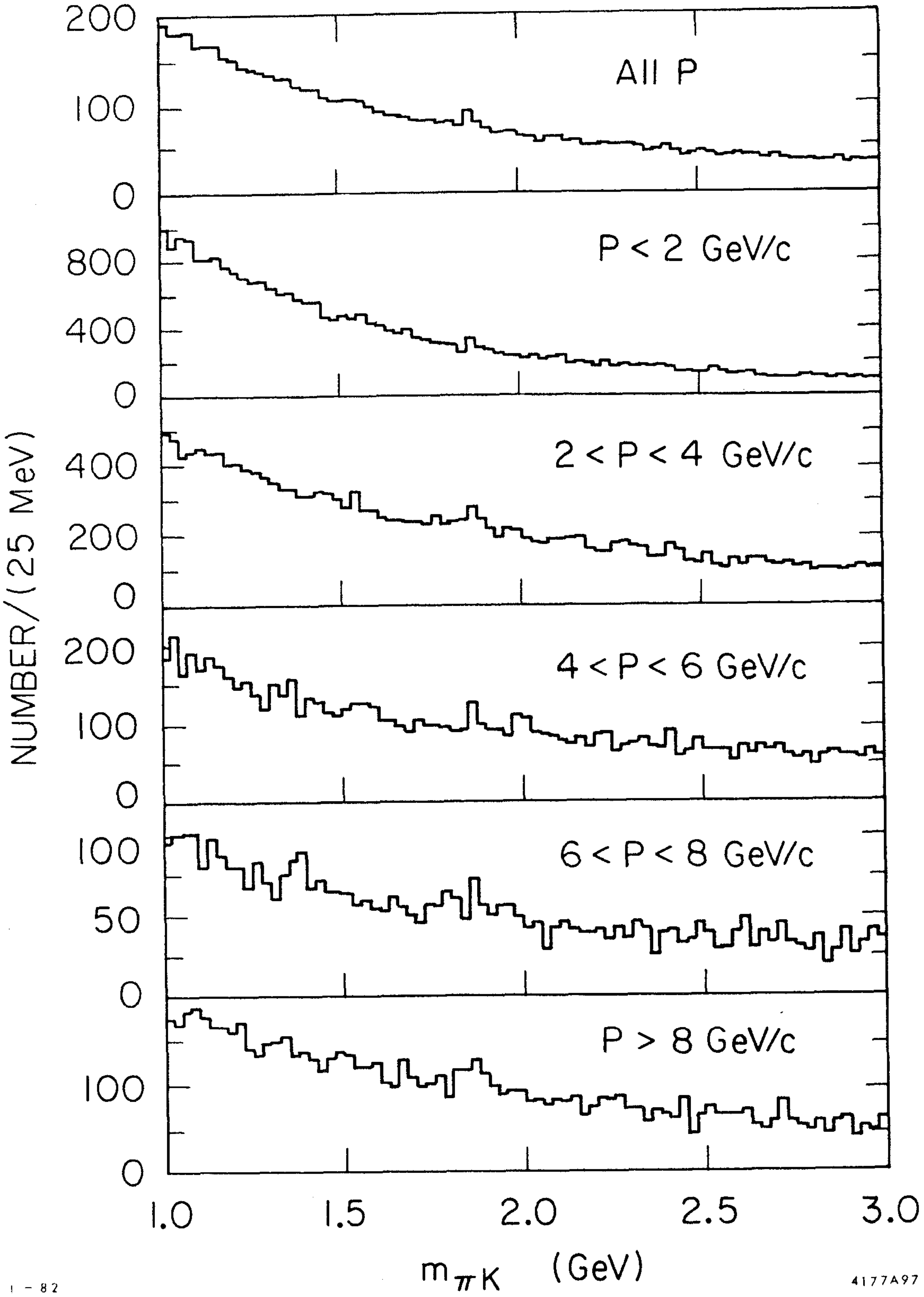

Fig. 1(b). Same as Fig. 1(a), but with f = 0.3%.

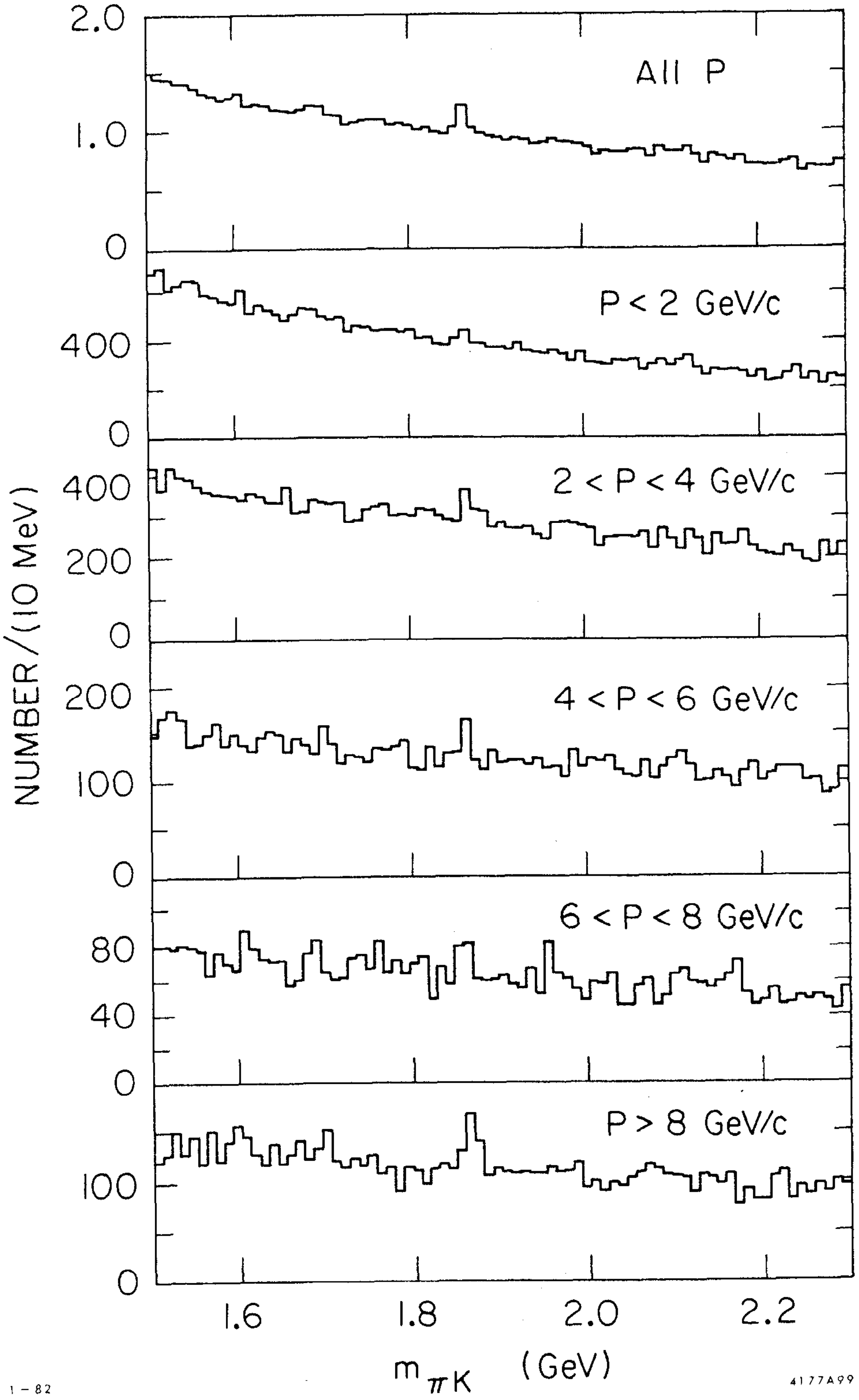

Fig. 1(c). Same as Fig. 1(a), but with no particle identification.

3. Multi-particle Invariant Masses[5]

The reconstruction of invariant masses may be useful in looking for the production of unstable particles or in conjunction with other information (e.g., secondary vertex detection) as a tag for specific types of events.

Looking at a two body decay:

$$M \rightarrow m_1 + m_2$$

and ignoring the angular errors as well as the masses of m_1 and m_2 (presumably light mesons) we get the mass reconstruction error:

$$\frac{\sigma_M}{M} = \frac{f}{2} \sqrt{E_1{}^2 + E_2{}^2} \quad , \text{ where}$$

E_1 and E_2 are the final particle energies. For multi-body final states, we might expect $\sqrt{E_1{}^2 + E_2{}^2}$ to be $\lesssim$ 10 GeV, so that:

$$\frac{\sigma_M}{M} \simeq 1\% \text{ requires } f = .2\%.$$

Figure 1 shows the expected invariant mass distribution for $K\pi$ combinations, assuming perfect particle identification for f = .1%, .3% and with no identification for f = .1%. It will be very hard to tag D's without further information (especially without perfect particle identification), however, an inclusive production cross section can be gotten for the lowest f value.

4. $Z^o \rightarrow H^o e^+ e^-$, $H^o \mu^+ \mu^-$.[6]

The Higg's rate, if it exists, is expected to be very small, giving:

- 25 events/year/lepton channel for m_H = 10 GeV
- 5 events/year/lepton channel for m_H = 30 GeV.

If we measure the lepton momenta we can search for a bump at the recoil Higgs mass. The resolution, if E_1 and E_2 are the lepton energies is:

$$\delta m_H = \frac{1}{m_H}\left[(m_Z - (1 - \cos\theta)E_2)\ \delta E_1 + (m_Z - (1 - \cos\theta)E_1)\delta E_2\right] \sim 1 \text{ to a few } (\delta E_1 + \delta E_2)$$

since $E_1 + E_2$ is usually close to $m_Z - m_H$. For $m_H = 10$ GeV, this gives a large error, ~ 5 GeV, even for f = .1%. For $m_H = 30$ GeV, $\delta m_H \simeq 4$ GeV for f = .3%, a useable number. Given the small number of events reconstructed, the muon mode would be useful corroborating evidence if a few events showed up in the electron mode (which gives best resolution using electromagnetic calorimetry). Note, the background from hadron pairs requires ~ 1000 to 1 rejection for the pair, which should be feasible for both muons and electrons.

We conclude from the above that the central tracking chamber should have:

$$f \leq .3\%.$$

A practical lower limit, as we shall see from the numbers in the next section is about

$$f = .1\%.$$

This range of $.1\% \leq f \leq .3\%$ corresponds in the elastic limit to a 5 to 15% momentum error which should also be adequate for inclusive measurements out to near the kinematic limit.

B. Consequences of the Momentum Resolution Requirements[7]

We consider a chamber with N wire layers, with successive layers equally spaced, giving a measurement in projection with spatial accuracy σ for each layer. The parameter f, used in the previous section, can then be calculated to be:

$$f = \frac{8\sqrt{5}\ \sigma}{.03\ BR_0^{\,2}\sqrt{N}}\ , \text{ where}$$

B = magnetic field and R_o = chamber outer radius.

A minimum solution giving f = .3% would therefore be:

$$R_o = 1.5\text{m},\ B = 5\text{kG},\ N = 30,$$

for σ = 200 μm. The value of f depends on the product $\dfrac{\sigma}{BR_0{}^2\ \sqrt{N}}$. A system with f = .1% would require, for example, R_o = 1.75m, B = 10kG, N = 45.

III. Hadronic Events

A. General Characteristics

A typical hadronic event at the Z^o is expected to have on the average about 20 charged tracks. The momentum spectrum for the hadrons is very broad and peaks at ~ 850 MeV. Among the charged tracks, one expects to find tracks originating from ~ 2 neutral vees/event (mostly at small radii) and ~ 1 kink/event. For chambers with radii between 1.4 - 2.0m, fields between 4 and 8kG one can expect on the average ~ 1/2 - 1 track trapped in the magnetic field/event. If such swirling tracks are expected to be a nuisance, it is important to try and minimize the amount of material preceding the chamber, since conversion electrons and positrons have a very soft spectrum. One can expect 2 - 3 extra swirling tracks/event for every 0.1 X_o of material traversed by photons before entering the chamber.

B. Segmentation Requirements for Track Finding in Axial Drift Chambers[7,8]

The main inherent track reconstruction pathologies at the Z^o are expected to be due to the difficulties in reconstructing many closely spaced tracks.

The Monte Carlo data has been analyzed using several different detector parameter values and a simple track reconstruction model. The detector model used consists of uniformly spaced layers of sense wires in a cylindrical geometry. Layers are spaced 3.75 cm in radius and the first layer is at 30 cm radius. Two choices for the outer chamber radius were looked at:

(1) 1.4 meter radius, 8kG, 30 layers.

(2) 2.0 meter radius, 4kG, 45 layers.

Several chamber lengths were also looked at. Little difference was found between (1) and (2), in terms of pattern recognition, so results will be quoted mainly for (1). No cuts were made on the jet directions.

The track acceptance criteria were as follows: A track generates a useable hit on a given layer if there are no other tracks within a certain "confusion distance" in projection, otherwise the hit is lost. This is actually more restrictive than is necessary since the first hit arriving on a wire should not be confused, it however avoids the necessity of defining the exact wire configuration and should give a reasonably good indication of the length scale where confusion starts becoming a problem. The "confusion distance", called ε, is taken to be a parameter of the calculation. A track is then considered to be accepted if the number of points for that track is greater than a certain minimum number, n_{min}, also taken as a parameter. The results are given in Table 1 for several n_{min} values and shown in Fig. 2 as a function of n_{min}. The values for $\varepsilon = 0$ give the geometrical losses. For these calculations the chamber length was 3m. Another important question is whether the tracks lost carry a substantial part of the energy of the charged tracks. The fractional reconstructed energy for various n_{min} and ε values is shown in Fig. 3.

These calculations indicate that a chamber with confusion distance $\simeq$ 2.5 mm would allow reconstruction of nearly all tracks within the detector solid angle while a value $\gtrsim$ 1 cm would lead to significant losses. Although difficult to achieve, a dual-track resolution of $\simeq$ 2.5 mm should be possible through the extension of present techniques. This will require that the pattern recognition program be able to choose which track a point lies on unambiguously if there are no neighboring hits within the confusion distance.

ε Confusion Distance (mm)	n_{min}	Percentage of Tracks Found	Percentage of Charged Energy Found
	8	89	89
0.0	16	80	80
	24	69	70
	8	89	88
2.5	16	78	78
	24	65	63
	8	87	86
5.0	16	76	74
	24	58	54
	8	84	81
10.0	16	69	64
	24	47	40
	8	76	69
20.0	16	57	49
	24	34	27

TABLE 1. This table shows how track finding is affected by changing the values of n_{min} and ε, the two parameters of the track finding model. These results are for the 1.4 m × 3 m, 8 kG detector model.

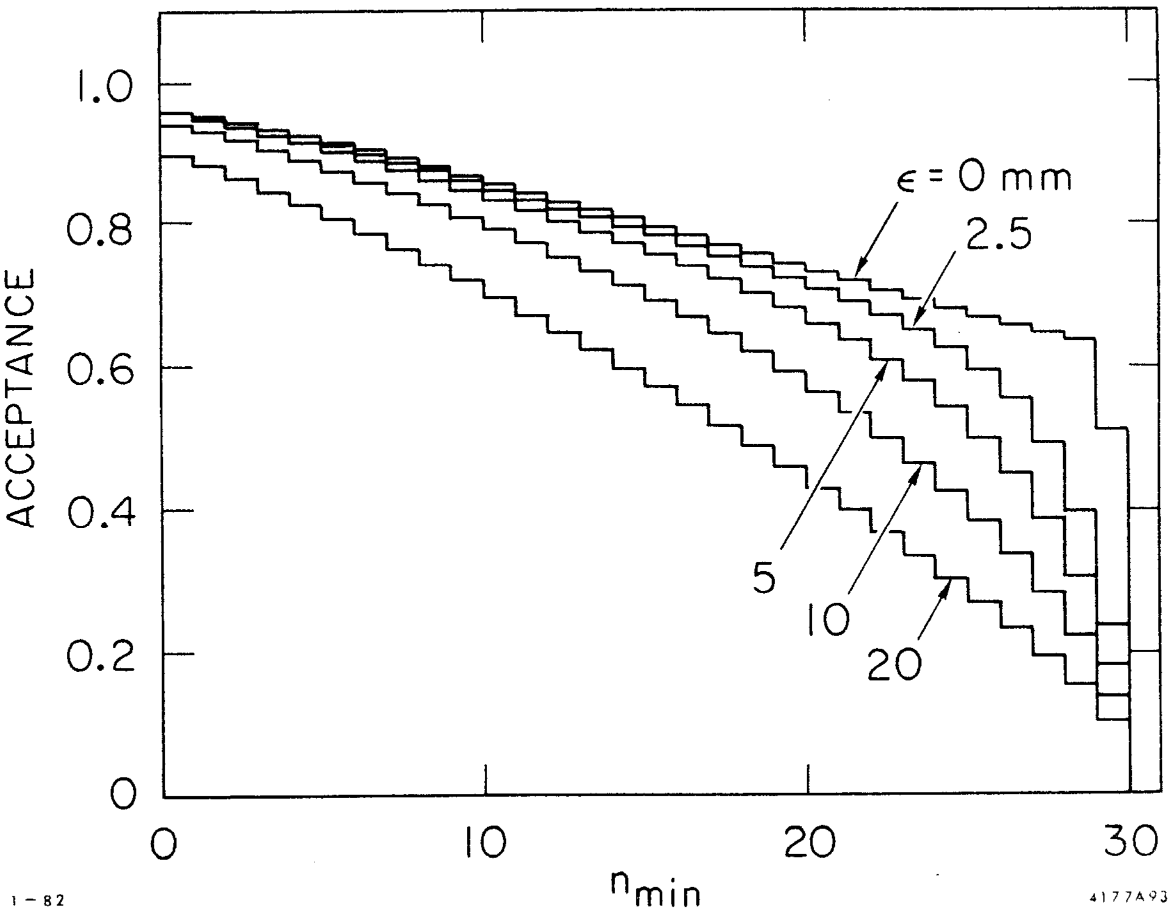

Fig. 2. Charged particle acceptance versus the confusion distance ε and the minimum numbers of layers, n_{min}, needed to consider the track found. Curves start below 1.0 because of tracks crossing no layers of the detector which has an inner radius of 30 cm.

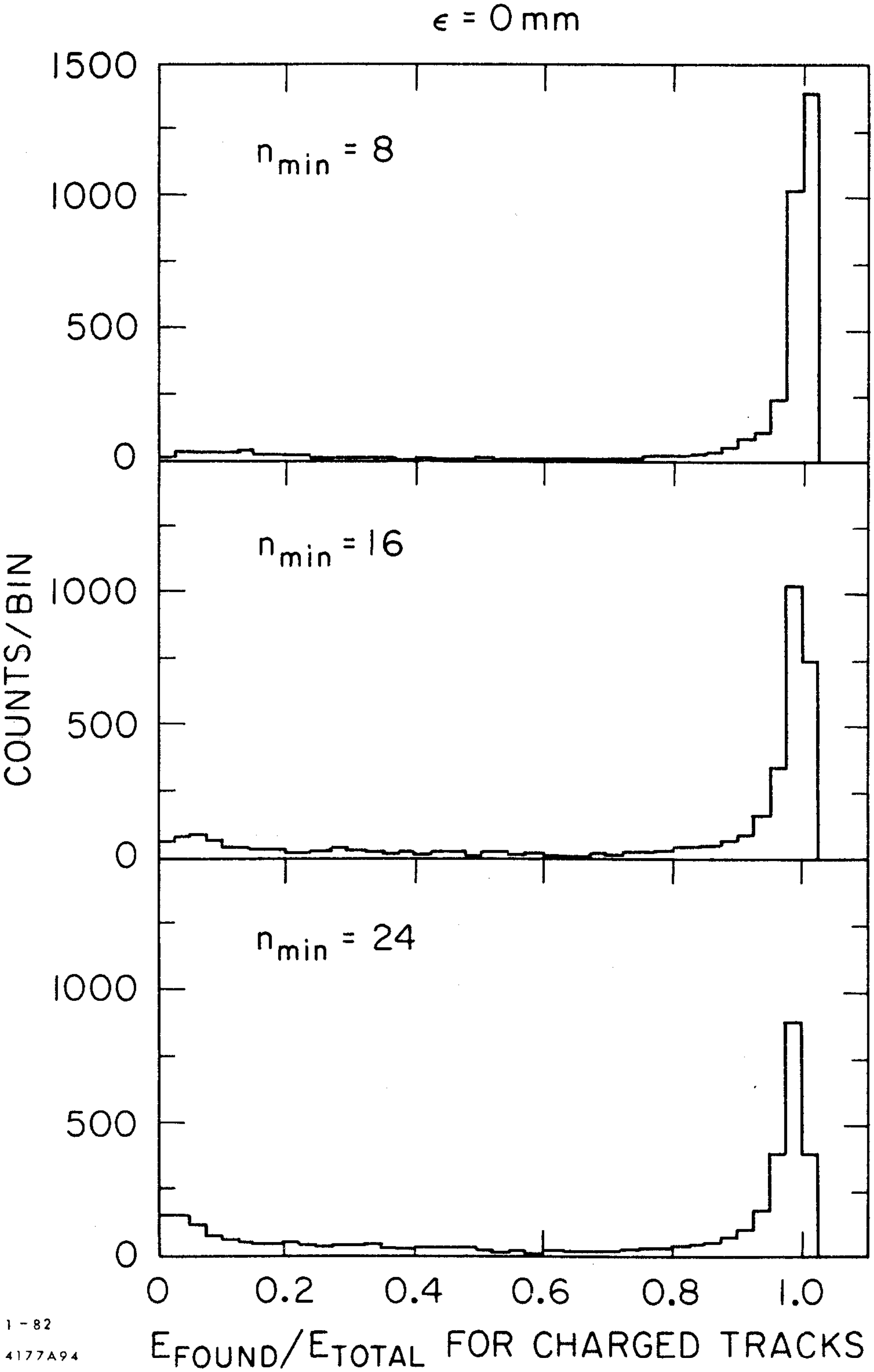

Fig. 3(a). Fraction of charged energy found for $\varepsilon = 0$ and various values of n_{min}.

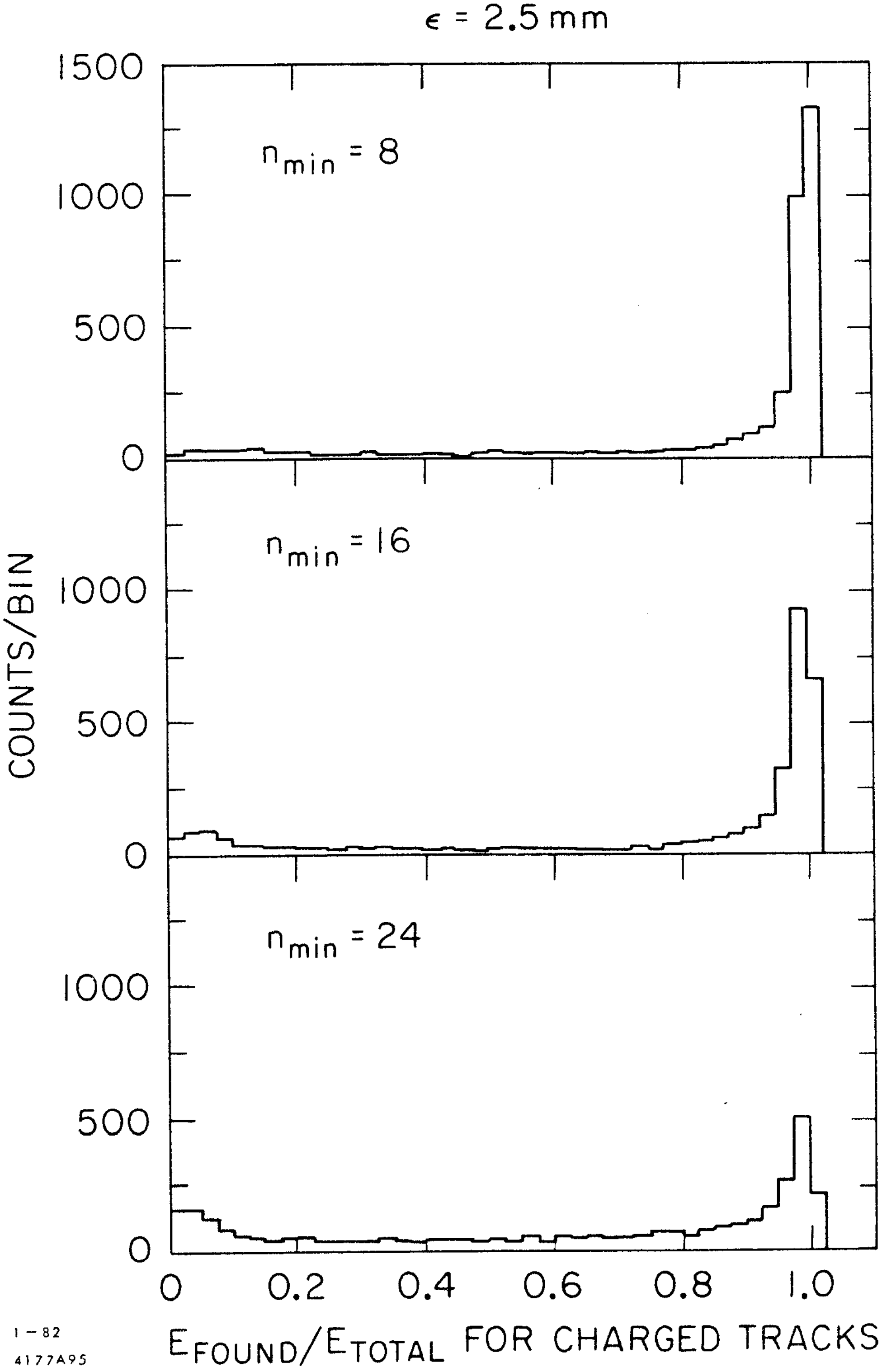

Fig. 3(b). Same as Fig. 3(a), but with $\varepsilon = 2.5$ mm.

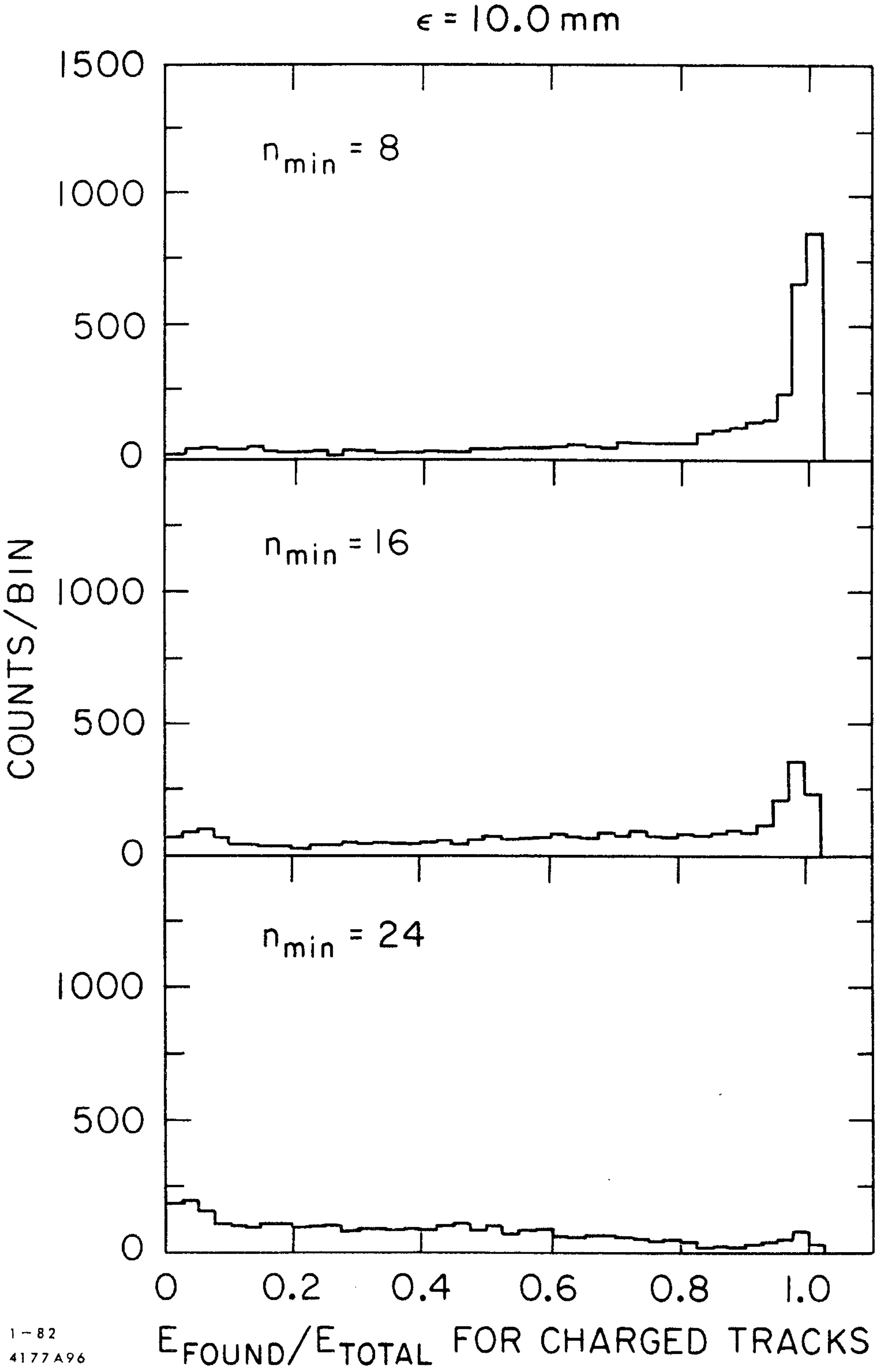

Fig. 3(c). Same as Fig. 3(a), but with ε = 1.0 cm.

IV. Limitations Imposed by the Chamber

A. Limits to Spatial Resolution[9]

Many factors, ranging from the physics of electron drift in gases to the mechanical tolerances of chamber construction contribute to drift chamber spatial resolution. We have investigated the limitations imposed by the physics of the drift cell and its timing electronics via a simple -- but hopefully realistic -- Monte Carlo model. The predictions are in good agreement with the data obtained with the MARK II vertex detector prototype. Large chamber systems will be seen to have roughly a factor of two to three times worse resolution than the predictions, indicating a need for improvement in the techniques of wire location, calibration, and determination of the time to space conversion as a function of position and angle for these systems.

The Monte Carlo model works as follows:

(1) A track is taken to pass a wire at impact parameter b.

(2) Along the track, distributed via a Poisson distribution, are n ionization events/cm (the mean value of n is 30 for Argon at 1 atm.).

(3) The electrons drift radially toward the wire (as is characteristic for the region near a wire for all chambers) in an electric field sufficiently high to saturate the drift velocity at a value w.

(4) During collection, they diffuse radially according to a gaussian with $\sigma = .5\sigma_t$, where σ_t characterizes the transverse diffusion. Note, the factor of 1/2 for the longitudinal/transverse ratio has been measured recently and is not in general accurately known for all gases.

(5) At the wire each electron is independently amplified by a factor A_i which is distributed according to:

$$P(\eta) = \frac{3}{2}\,\eta e^{-\frac{3\eta}{2}}, \quad \eta = A_i/\bar{A}$$

(6) The chamber acts as a transmission line driven by a current source giving a voltage pulse which is, to within a constant:

$$V(t) = A_i/(t_o + t), \; t_o = 1 \text{ nsec}$$

for typical chambers.

(7) The amplifier which amplifies this signal is characterized by a rise time t_r. This is approximated by assuming the amplifier response to a step-function input is a ramp of duration t_r, followed by a plateau. This gives for the final output signal a voltage:

$$V(t) = \frac{A_i}{t_r}\,\ell n(1+t/to) \text{ for } t < t_r$$

$$V(t) = \frac{A_i}{t_r}\,\{\ell n(1 + \frac{t}{to}) - \ell n(1 + \frac{(t - t_r)}{to})\} \text{ for } t > t_r.$$

(8) The final signal which is fed to a discriminator is just the sum of the individual pulses delayed relative to each other by the electron arrival times at the sense wire. The dispersion in discriminator firing times can then be calculated as a function of b, σ, t_r, and discriminator threshold, V_t suitably normalized to the units used above.

The results are shown in Fig. 4 where $V_t = .2$ is a value characteristic of the MARK II vertex detector (corresponds to triggering on a single average ionization event). $V_t = .8$, $t_r = 10$ns, also shown, is characteristic of the main MARK II drift chamber and requires on the average three or more closely time correlated ionization events to trigger the discriminator. We see that within about 5mm of the sense wire the resolution is sensitive to the amplifier-

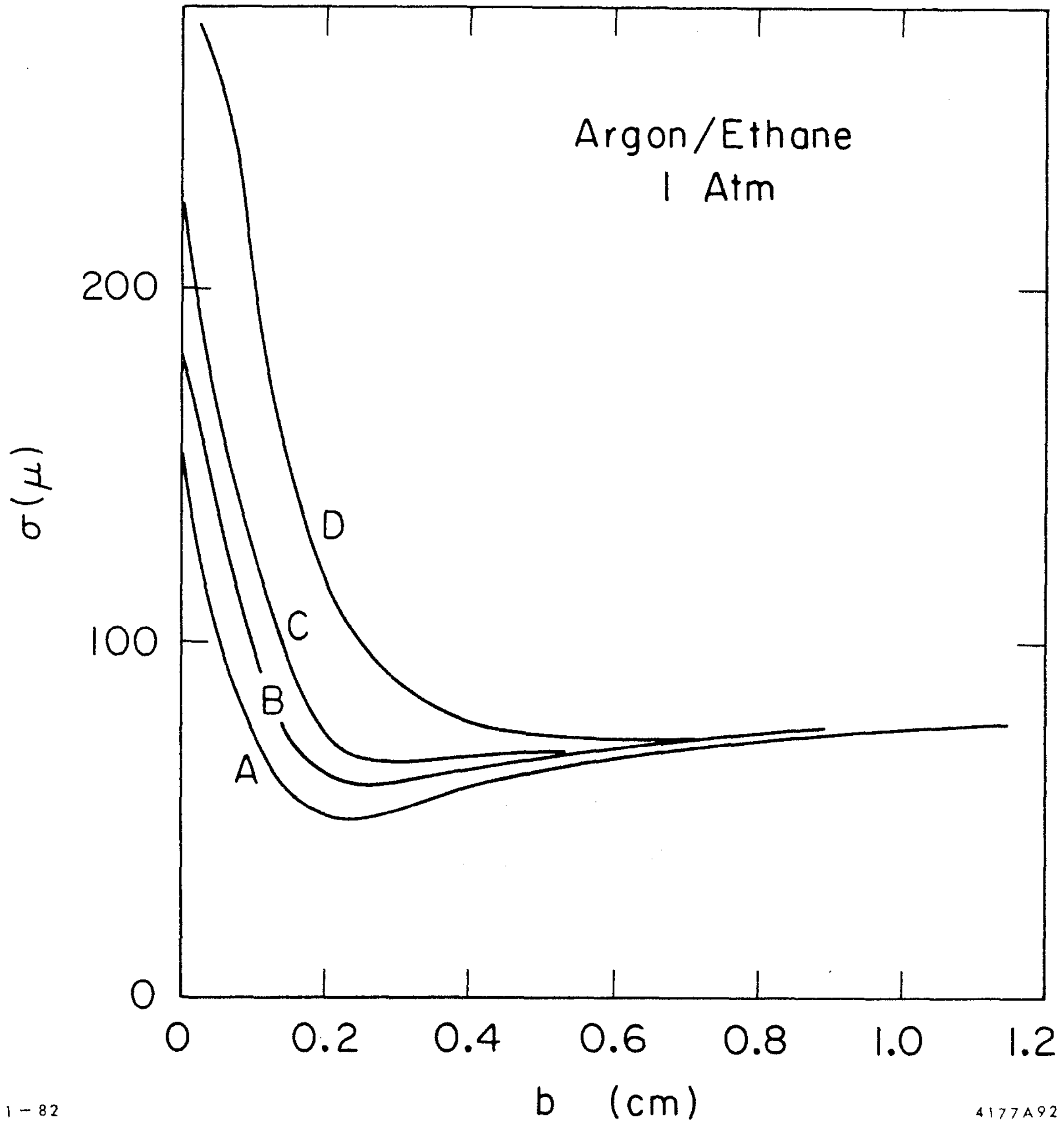

Fig. 4. Predicted drift chamber resolution versus impact parameter for 50/50 Argon/Ethane gas at 1 atm. Longitudinal diffusion has been taken to be characterized by $\sigma = 120\ \mu\text{m}\ \sqrt{\text{Distance(cm)}}$. Curves are predictions for: (A) Statistics plus diffusion; (B) $v_t = .2$, $t_r = 5$ nsec (MARK II vertex detector); (C) $v_t = .2$, $t_r = 10$ nsec; (D) $v_t = .8$, $t_r = 10$ nsec (MARK II central drift chamber).

discriminator choice, for larger distances the resolution is dominated by diffusion and statistics and should be about 80 μm out to about a 2 cm distance for 50/50 Argon-Ethane gas. The dependence of the resolution on the type of gas and the pressure are shown in Fig. 5. We see that none of the large systems presently operating are exploiting the potential chamber accuracy to the fullest.

B. Chamber Gases[10]

This is a much studied, complicated subject and we will focus mainly on one topic here. That topic is the choice of a drift chamber gas which is most suited to the severe dual-track resolution requirements at the SLC. This question is mainly relevant to a design in which multiple-hit electronics is used.

To minimize the interference of neighboring tracks on each other, for a given chamber geometry, we would like to spread the ionization electron arrival times so that the $1/(t+t_0)$ pulse tail from the first hit, seen by the second hit, is minimized. Also it would be very advantageous to minimize the Lorentz-Angle for the drift since this typically widens the dispersion in arrival times for each hit and makes the cell left-right asymmetric.[11]

These two requirements can be satisfied by a gas with slower drift-velocity than the canonical 5 cm/μsec. Fig. 6 shows the drift velocities for several common gas mixtures. Several gases have reasonably flat drift-velocity curves, with velocities in the 2.5 - 3.0 cm/μsec range. These, with 90/10 Ar-CH_4 having the smallest value, require a drift field in the 1.5 to 2.0 kV/cm range. This drift field, which is higher than presently typical values, further reduces the Lorentz-Angle which depends on $v_{Drift}B/E$. For presently operating chambers

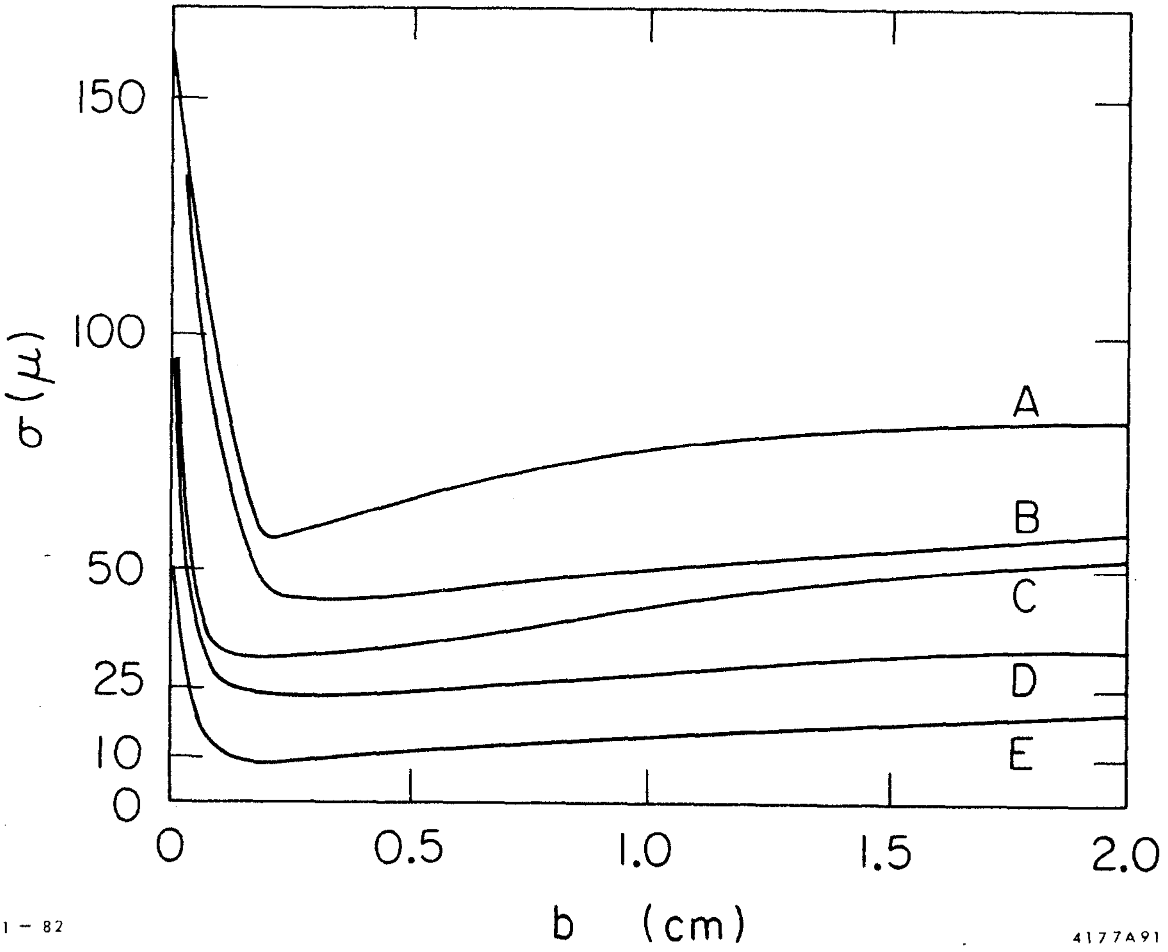

Fig. 5. Model calculations for resolution versus track impact parameter. Curves are: (A) 50/50 Argon/Ethane at 1 atm; (B) Pure Ethane at 1 atm; (C) 50/50 Argon/Ethane at 2 atm; (D) Pure Ethane at 2 atm; (E) Isobutane at 3 atm.

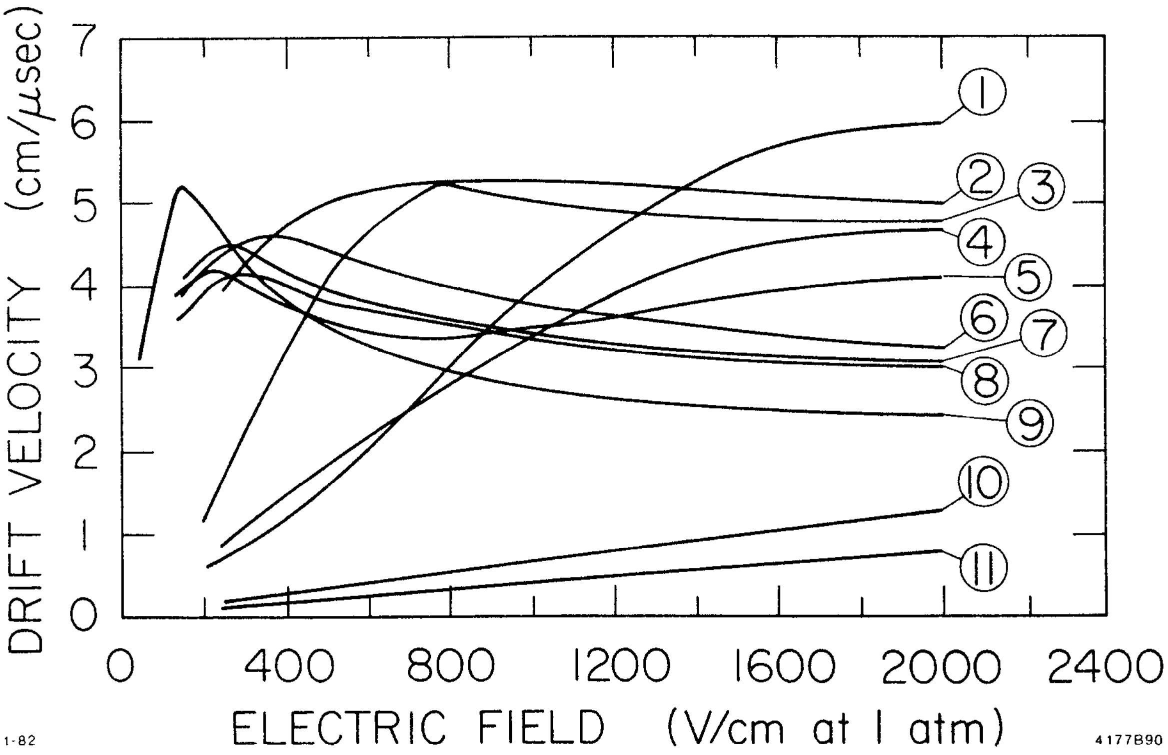

Fig. 6. Drift velocity versus the electric field for various gases. Gases are: (1) 80/20, Ar/CO_2; (2) 50/50, Ar/C_2H_6; (3) 90/10, Ar/CO_2; (4) i-C_4H_{10}; (5) 90/10, Ar/C_2H_4; (6) 90/10, Ar/i-C_4H_{10}; (7) 90/10, Ar/C_2H_6; (8) 90/10, Ar/C_3H_8; (9) 90/10, Ar/CH_4; (10) CO_2; (11) Ar.

with B = 4kG, the Lorentz-Angle ≃ 18^{o} for a drift field of 1kV/cm. The use of a slow gas would be essential if one wanted to use multi-hit electronics for a chamber system in a much larger magnetic field.

The larger drift field needed for a slow gas need not imply a larger field on any of the wires in the chamber and arises naturally if one tries to adjust the chamber geometry to improve dual-track resolution in one cell. This question will be addressed in a later section.

The difficulty with using 90/10 $Ar-CH_4$ is the large transverse diffusion, σ_t, for that gas. Calculated values of σ_t for several gases are shown in Fig. 7. Unfortunately these values do not tell us what the longitudinal diffusion coefficient is. As mentioned earlier it may be substantially less. Addition of some CO_2 would reduce the diffusion but one would have to measure how the drift velocity is affected. If one wanted to use a slow gas a measurement of both velocity and resolution for various $Ar-CH_4-CO_2$ mixtures would be very useful. We have repeated the drift chamber spatial resolution Monte Carlo calculation discussed in the previous section for a gas with drift velocity = 2.5 cm/μsec and longitudinal diffusion given by $\sigma = 300$ μm for a 1 cm drift. The spatial resolution in such a chamber, due to the effects included in the calculation, is < 200 μm out to a drift distance of 2 cm.

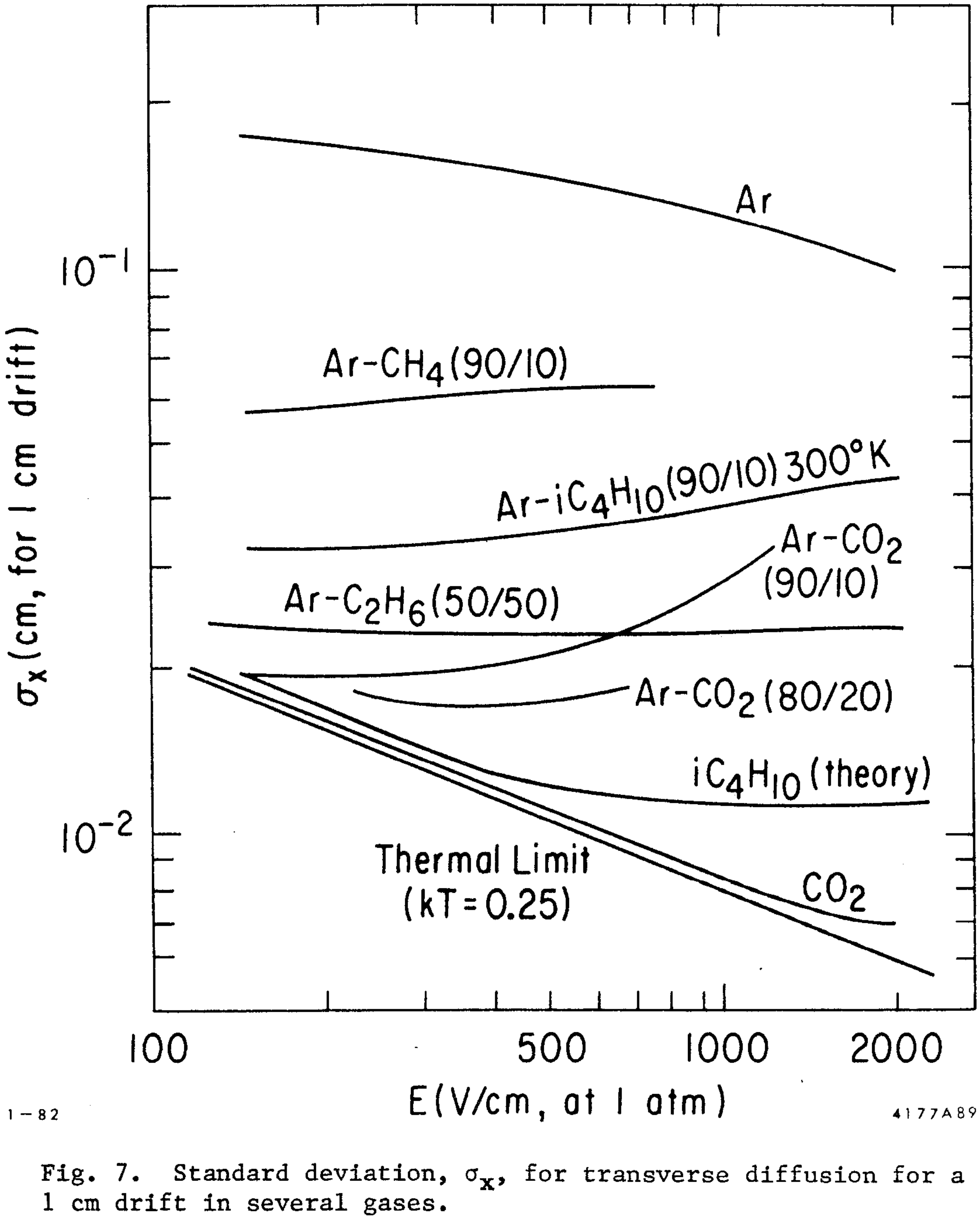

Fig. 7. Standard deviation, σ_x, for transverse diffusion for a 1 cm drift in several gases.

C. Current-Division[12]

The use of current division provides one of the main techniques for measuring the z-coordinate and dip angle for tracks in a chamber. The technique has the advantage of allowing z to be measured simultaneously with r and ϕ. For reasonably stiff tracks the tangent of the dip angle, t, is given by:

$$t = z/r$$

where the z coordinate is measured at radius r in cylindrical coordinates. If we measure z, with accuracy σ_z, at m successive, equally spaced radii, then fitting a straight line to the measurements gives an error

$$\sigma_t = \frac{\sqrt{3}\,\sigma_z}{R_o\sqrt{m}}\text{, for large m, where } R_o = \text{Outer Radius.}$$

If we assume the chamber has a wire length = L = $2R_o$, then:

$$\sigma_t = 2\sqrt{\frac{3}{m}}\left(\frac{\sigma_z}{L}\right).$$

If z is measured on 30 layers then:

$$\sigma_t = .6\left(\frac{\sigma_z}{L}\right).$$

For $\sigma_z/L = .5\%$, a typical value, this gives a 3mrad error. If one could achieve $\frac{\sigma_z}{L} = .25\%$, then $\sigma_t = 1.5$ mrad, a value close to the accuracy in measuring σ_ϕ for most tracks, given the contribution of multiple-scattering. The error in the momentum $p = p_\perp\sqrt{1 + t^2}$, is insensitive to the error in the t measurement for the values above.

The resolution achieved with the current division technique in large experiments is typically $\sigma_z/L \simeq .5\%$ for a chamber gain $\simeq 4 \times 10^4$. This requires that the amplifier be on the chamber and is limited by the noise generated by the resistance of the wire itself, which provides a minimum noise level. Operating at twice the gain, the resolution can be pushed to .25%, but requires that various systematic effects, discussed below, be kept to the .1% level. The higher gain would however degrade the measurement of dE/dx if that is desired.

In the current division technique one determines the position along a wire by measuring the charges collected on both ends of the wire with low impedance amplifiers. The technique is thus sensitive to feedback across the wire, the presence of pulse tails from earlier particles passing at different positions, and the division of cross-talk pulses from particles at different positions in neighboring cells. The scheme can be schematically written as

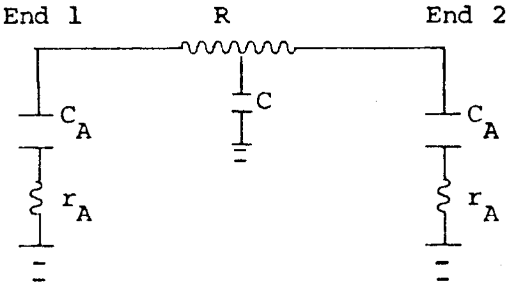

R,C = total resistance and capacitance to ground for the wire, C_A and r_A are the equivalent series capacitance and resistance of the amplifier.

We define the ratio for the charge collected on one side of the wire over the total by:

$$\text{Ratio} = Q_1/(Q_1 + Q_2)$$

Then, measuring distances (= z) from End 2, Ratio is a linear function of z (to better than .1% accuracy) provided we integrate over a time $\gtrsim$ RC which is a time characteristic of the diffusive division process. Typically RC $\simeq$ 50 nsec. For a δ-function current source at $t = 0$, we measure:

$$\text{Ratio} = (1-2\beta)\frac{z}{L} + \beta, \text{ where } L = \text{wire length.}$$

The intercept $\beta = \frac{1}{2}\left[\frac{(1-e^{-t/\tau})R + 2r_A}{R + 2r_A}\right]$ where: t = integration time (assumed >> RC), $\tau = \frac{(R+2r_A)C_A}{2}$. The exponential term comes from the discharge across the wire of one capacitor into the other (because of their difference in potential) and the other term comes from the finite resistance of the amplifier. Since the real pulse shape is quite variable, the exponential term introduces an uncertainty into the z-calculation, as well as degrading the multi-hit capability, since the capacitive discharge will contribute to later charge measurements. If we wish to keep such systematics < .1%, t/τ should be $\lesssim 10^{-3}$; or τ = 50 μsec for t = 50 nsec.

A similar, but more serious problem is posed by the long 1/t tail of a realistic drift chamber pulse. The time dependence of such a pulse is given by $1/(t+t_o)$, where:

$$t_o = \frac{r_w^2}{2\mu^+ \ (E_w r_w)} , \ \mu^+ = \text{positive ion}$$

mobility ≃ 1.8 $cm^2V^{-1}sec^{-1}$, r_w = sense wire radius, E_w = electric field on the wire surface. t_o is typically ≃ 1 nsec. Minimizing r_w will result in the smallest t_o, however, the effect on the integrated pulse tail is logarithmic. Similarly, a slow drift velocity is helpful in spacing-out in time the ionization arriving from two distinct tracks, but again the effect is logarithmic.

Integrating the above pulse shape from t = 0 to t = 50 nsec (signal) and comparing to the integral from t = 100 to t = 150 nsec (tail), gives a signal to tail ratio ~ $\ln(50/t_o)/\ln(150/100)$ for two nearby tracks. We can therefore estimate that the tail (if not suppressed) would contribute ~ 10% to later signals. Although this can be roughly corrected for off-line it would be preferable to suppress this tail electronically -- with a factor ~ 100 desirable. This suppression can be achieved by cascaded pole/zero circuits -- as described in reference 13.

A final problem is the cross-talk (positive induced pulse) between sense wires which can be expressed in terms of a coupling matrix. These pulses are divided by the current division technique like a normal pulse. With the large number of hits at the Z^o, the likelihood of hits in neighboring cells, with similar drift distances, is non-negligible. For these cases the induced pulse would couple the two z-measurements. For drift cells with multiple sense wires, as for example in the MARK III drift chamber, the coupling between sense wires in neighboring cells is about .2% -- an acceptably small value. For small cells, such as the smaller cells of the MARK II drift chamber the nearest neighbor coupling is about 3%. This value is large enough to degrade the resolution for such interfering hits.

V. Specific Solutions

A. TPC[8]

The TPC, unlike the axial chambers discussed in the previous sections, can be characterized by a three dimensional confusion distance when evaluating tracking efficiency. We have repeated the track finding calculation done earlier, with a confusion distance in projection = 2 cm and one in z also = 2 cm. This was done for a detector of the same dimensions (R_o = 1.4m) and with the same number of layers (30) as before. This TPC would provide excellent track finding capability, about as good as an axial chamber with ε = 2.5 mm. It would of course also provide $\frac{dE}{dx}$ information allowing particle identification. This question is addressed further in the report of the subgroup on Particle Identification. We have not investigated the other aspects of this solution, such as the limit to precision, since data from the TPC in the PEP environment should be available in the near future.

B. Small Cells[14]

One solution which is both well understood and would give enough hits to allow good track finding would be to build a chamber with many small cells, for example cells with a full width = 1.5 cm. This suffers principally from requiring many sense wires, and therefore many electronics channels, as well as the left-right ambiguity for each measurement. If we assume the chamber has N equally spaced wire layers up to a radius R_o, with cell half-width = w, then the total number of wires in the system is given by:

$$\frac{\pi R_o (N+1)}{2w}$$

For N = 30, R_o = 1.5m, 2w = 1.5 cm we get 10,000 sense wires.

In order to solve the left-right ambiguity one could organize the 30 layers into 15 pairs or 10 triplets of nearby closely spaced cells, successive cells staggered by w. Triplets have the advantage over doublets that they allow a check of the consistency of the measurements associated with one track. A disadvantage of this scheme is that the dual-track segmentation for solution of the left-right ambiguity is worsened since several cells are involved. A further discussion of the use of such a chamber can be found in Ref. 15.

In the existing chambers of the MARK II type, the z coordinate has been measured using small angle stereo, with 3^o a typical stereo angle. Assuming at least 10 of the layers in the chamber are stereo layers, with a 4 mm precision in z/per measurement, the tangent of the dip angle can be measured to a precision of about 1.5 mrad for tracks crossing all layers of a 1.5 m chamber.

The question of track finding in such a chamber has been looked at using the Z^o events and the following scheme:

(1) Follow tracks, generating hits on N axial layers.

(2) Keep only unconfused hits, drop all confused or missing hits. A

confused hit is one which has a neighbor closer than 2.5 mm, where it is assumed that this separation is needed at the pattern recognition level. For n hits in a cell, a probability = 1/n is assigned for finding a specific hit. This corresponds to a randomized cell geometry.

(3) A track is considered found if at least six axial hits on the track provide good hits.

Taking a chamber with 20 axial layers, inner and outer radius = .3 m and 1.5 m respectively, and 2 cm size cells, gives at least 95% track finding efficiency at all momenta for tracks crossing all layers using the track finding criteria above. Another relevant parameter is the number of "confusing hits", i.e., hits from tracks in the same cell as the given track and separated by less than 2.5 mm. 88% of all tracks have fewer than two such "confusing hits" among the 20 potential hits.

C. Large Cells with Multi-Hit Electronics[12]

Given the large number of wires involved in a system with small cells, an attractive alternative would be to use larger cells and multiple hit electronics. In such a large cell it is important to maintain rather uniform drift properties so that a reasonable space-time relation exists and so that pulse widths are not too great. One can achieve this by grouping several sense wires into one cell so that the cell dimensions along the radial direction are $\gtrsim$ cell half-width w (a minimum value for sufficiently uniform behavior in the cell is actually 1.5 w).

Figure 8 shows a part of a multi-wire cell, which is taken as rectangular in shape for simplicity. The main parameters are:

r_w = radius of a sense wire.

r_f = radius of a field wire.

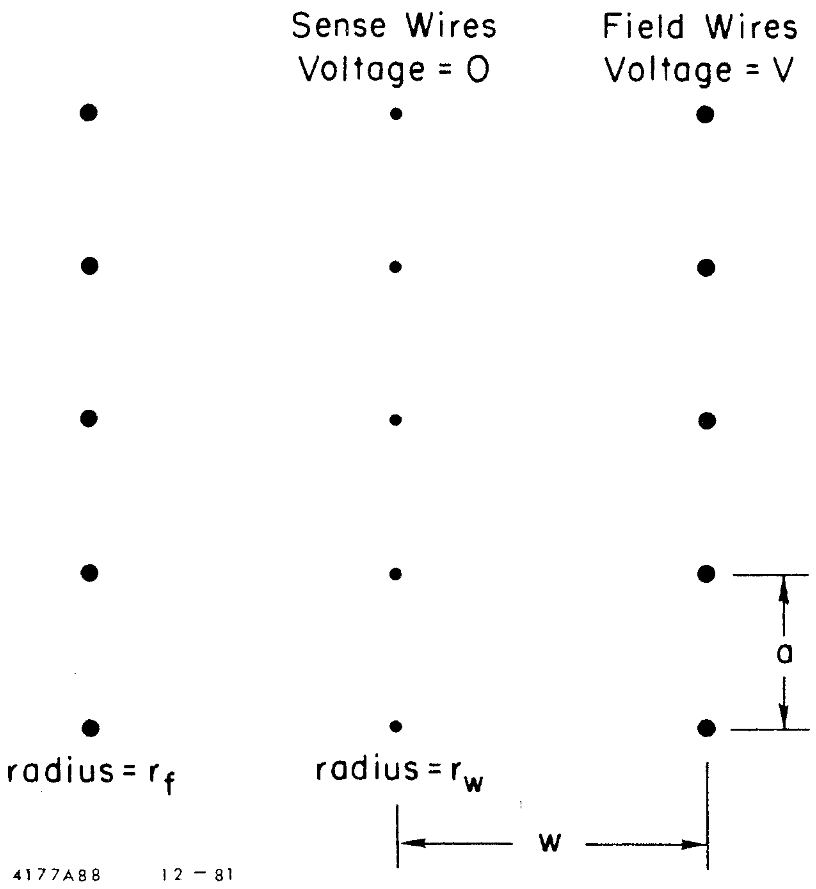

Fig. 8. Multi-sense-wire drift cell.

E_w = electric field at the surface of a sense wire.

E_{cell} = nearly constant drift field over the bulk of the cell.

a = spacing between wires along the sense wire plane (radial direction).

w = cell half-width.

In the following discussion all field wires and sense wires are assumed to be at a potential V and at ground respectively. To reduce cross-talk, every second wire in the sense plane can be taken to be thicker so it does not amplify and thus is not read-out. In this case the spacing between the sense wires used is actually = 2a. We do not discuss here in detail the case of negative voltage on these thicker wires, which can be used to reduce V, and which can be explored as an interesting added degree of freedom.[16] The case of no negative voltage gives the best dual-track resolution for a given spacing a.

This type of cell is sufficiently simple that its behavior can be thought of as follows: (for simplicity in the discussion we chose the same radius r_w for all sense plane wires)

(1) Near each wire we have a roughly radial field varying as 1/r. This near region extends to a radius = a/π.

(2) The rest of the cell has a nearly constant drift field E_{cell}. Using Gauss' law the field on the sense wires and E_{cell} are related by:

$$E_{cell} = \left[\frac{\pi\, r_w}{a}\right] E_w$$

Note: E_w is fixed by the chamber gain for a given r_w. $r_w E_w$ is ~ 250-350 volts for typical wires, gains and gases. Thus for a = 1 cm we expect E_{cell} = 1kV/cm which is a typical value.

(3) The cell dimension w enters only into the determination of the absolute voltage, V, on the field wires. Integrating from a sense

to a field wire using a $1/r$ field within a/π of a wire and E_{cell} elsewhere gives a good estimate:

$$V = E_{cell}\left[(w - \frac{2a}{\pi}) + \frac{a}{\pi}\ \ell n\ (\frac{a}{\pi r_w}) + \frac{a}{\pi}\ \ell n(\frac{a}{\pi r_f})\right]$$

(4) The trajectories of typical drifting ionization electrons are shown in Figure 9 for the case of no magnetic field. For the inner wires in the cell the trajectories are parallel straight lines till they reach the near region. Looking at the figure the maximum path difference among the ionization electrons produced by one normally incident particle is $\approx a/2$. If we want the arrival of all ionization electrons from two normally incident particles to be separated in time, then the two particles must be incident at impact parameters separated by $> a/2$. Thus $a/2$ is approximately the dual-track separation distance for the cell.

(5) For incidence at an angle θ, the maximum path difference is $\frac{a}{2}$ $(1+\tan\theta)$. The dual-track resolution is therefore not seriously degraded by non-normal incidence. For example, $\tan\theta = 1/2$ for 26° which is a large bend angle. Note, the Lorentz-Angle acts as an additional angle adding or subtracting from θ depending on the track orientation.

With these characteristics in mind, we have looked at a drift cell containing three sense wires with $a = 6$ mm (the useable sense wires are spaced by 2a) and $w = 3$ cm. For this case $E_{cell} = 1.5$ kV/cm, making 90/10 Ar-Methane with $v_{Drift} = 2.5/\mu sec$ a possible gas choice. Using the program discussed earlier, which generates and follows ionization electrons produced in the cell, Figure 10 shows the distribution of collected electrons from two normally incident tracks whose hit positions differ by 3mm. The calculation

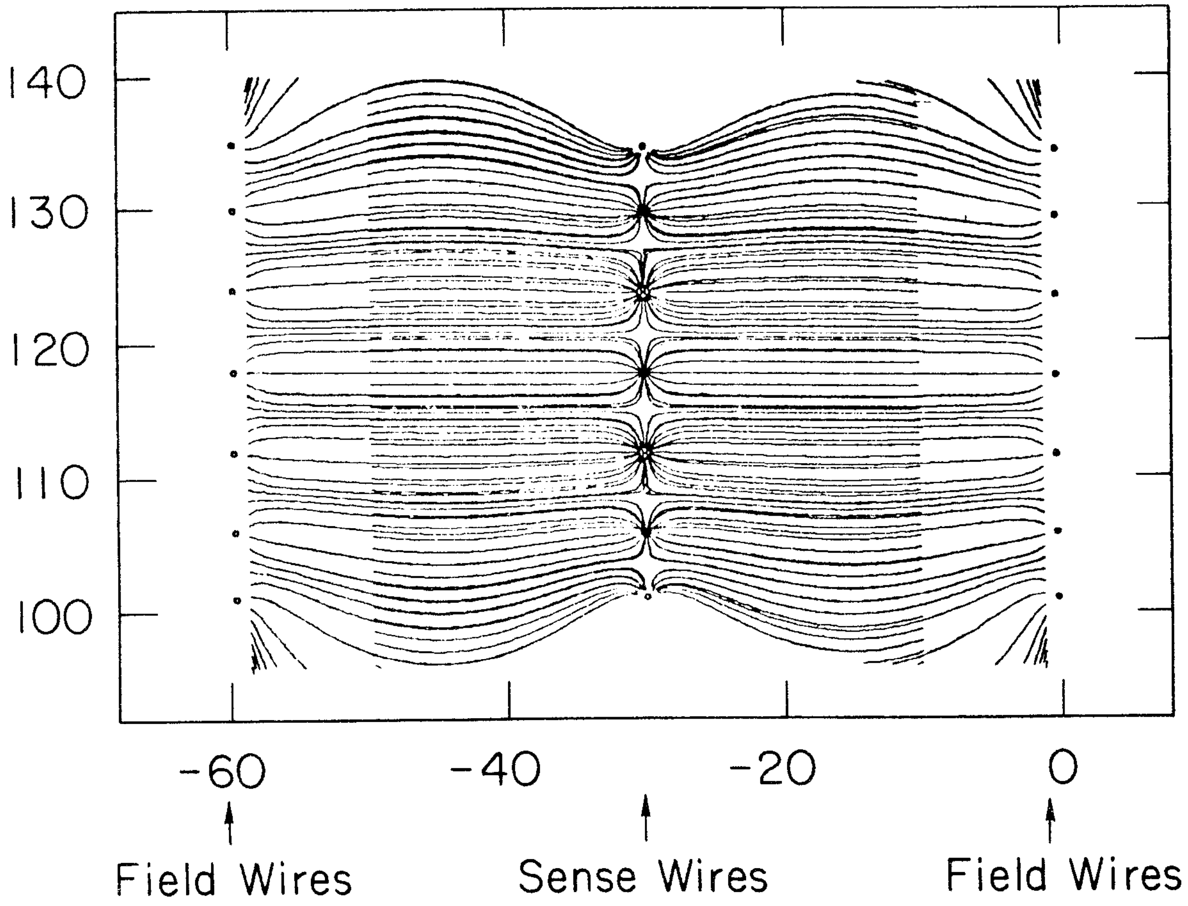

1-82

4177A151

Fig. 9. Representative electron drift trajectories for several normally incident tracks. Cell half-width is 3 cm for this example. For simplicity we have taken the case of no magnetic field.

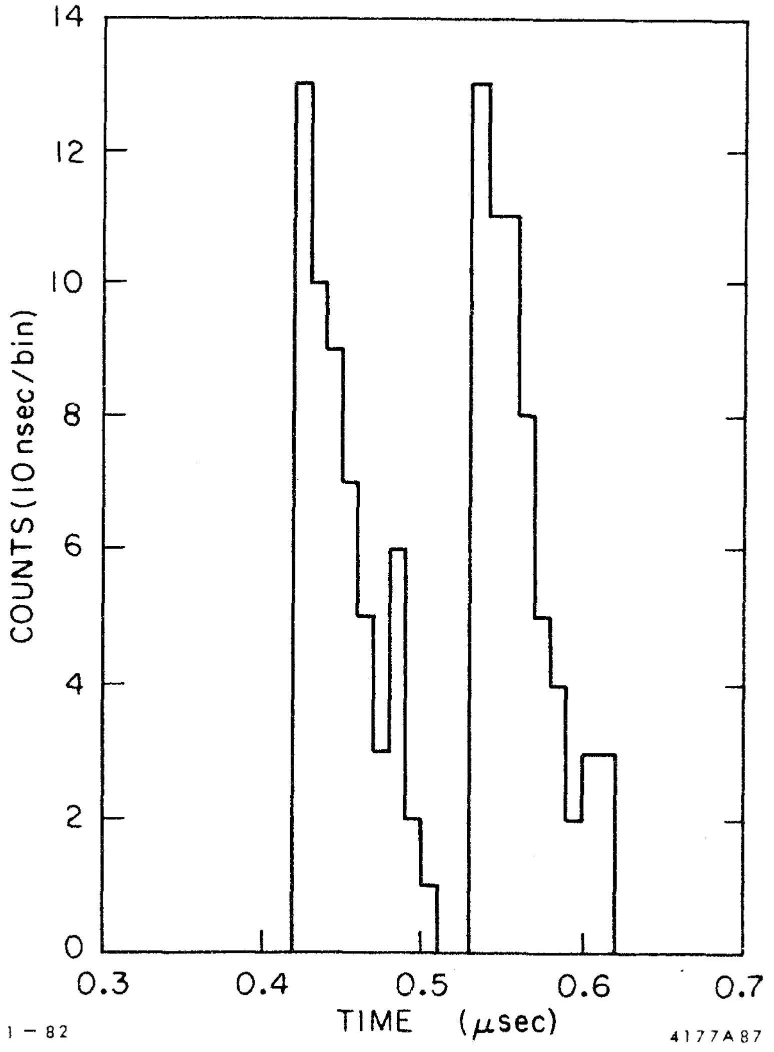

Fig. 10. Ionization electron arrival time spectra produced by two normally incident tracks whose impact parameters are separated by 3 mm in space. Cell is that shown in previous figure, but now with a 5 kG magnetic field.

has been done with a 5kG field for 90/10 Ar-CH_4 gas. The variation of the drift velocity with the local electric field as well as the local Lorentz-Angle have been included in the calculation.[17] A confusion distance ~ few mm should be attainable for such a cell.

A further advantage of multi-sense wire cells is that by staggering alternate sense wires by $\pm\delta$ we can resolve the left-right ambiguity in an individual cell before pattern recognition. Taking the example of wire triplets, the quantity

$$\Delta = v_{\text{Drift}} \left[\frac{t_1 + t_3}{2} - t_2 \right]$$

where the t_i are the measured times, is centered at $\pm 2\delta$ with the sign giving the side of the cell traversed. Thus if $4\delta >>$ error on Δ we can resolve the left-right ambiguity. Using $\sigma_\Delta = \sqrt{\frac{3}{2}}\,\sigma_x$, with σ_x = usual 200 μm, gives $\delta \simeq 280$ μm if we want $4\delta = 5\sigma_\Delta$. Note, δ is small enough that it does not significantly enlarge the dual-track confusion distance for left-right ambiguity resolution. Also, the comparison of the three times allows the use of the very good resolution of the chamber for the rejection of spurious hits (multi-pulsing, single bremsstrahlung hits, poorly measured points due to δ-rays, confused points due to crossing tracks in the cell) before pattern recognition begins. This could be particularly useful in an environment containing many soft photons or neutrons which might give a fair number of single hits but very few valid triplets.

VI. Pattern Recognition

For an event at the Z^o the vast majority of tracks emanate from a well defined point. This constraint is very useful in devising track finding schemes. For a track emanating from the origin, in a constant B field, we can write the track's equation in cylindrical coordinates (r, ϕ, z):

$$r = 2R \sin(\phi-\phi_o)$$

$$z = t\left[2R(\phi-\phi_o)\right] = rt \left[\frac{\phi-\phi_o}{\sin(\phi-\phi_o)}\right] \simeq rt \text{ for most momenta.}$$

R, ϕ_o, t are the parameters describing the track, where R = track's radius of curvature, ϕ_o = azimuth at the origin, t = tangent of the dip angle. The curvature K = 1/R is frequently a preferable variable.

Since three points determine a circle, one needs only two drift chamber hits on a given track, in conjunction with the origin, to predict all the other hits on the track. Thus, for example, the MARK II track finding strategy is to cycle over hits in two distinct layers, with the correct pair choice having associable hits on the other layers.

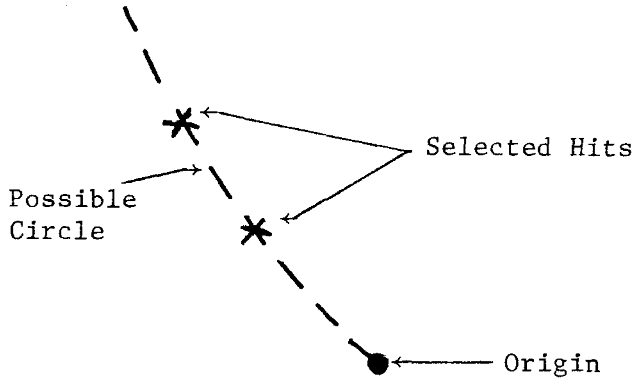

An alternative, but somewhat similar scheme, is used by the MARK III detector. In this case the two layers keyed on are associated into one multi-wire cell, which actually contains three wires. A multi-wire cell can then be thought of as measuring a position and tangent vector to the track, locally. This reduces the precision in predicting the other hits which are subsequently picked up, however it has the advantage that the group of hits keyed on essentially always do belong to the same track, the left-right ambiguity can be solved before looking for other hits, and the presence of three rather than two wires provides a very stringent consistency check that the hits are sensible.

Both of the schemes discussed above have drawbacks when extended to the Z^o energy range. The first scheme has the problem that the left-right ambiguity multiplies the number of choices and the high particle density significantly increases the number of wrong-to-right pairs to choose from. The second scheme gives a rather wide road in space (~ few cm) when predicting, so again the high particle density will give multiple choices to try.

There are several ways to reduce the choices in the track finding procedure. The first method sticks closely to the MARK II procedure but includes the advantages of the second scheme. Suppose the chamber is built in a way that allows a local resolution of the left-right ambiguity (via, for example, wire triplets in one cell or half-cell staggered small nearby cells). Then each group of wires used to solve the left-right ambiguity provide also a local tangent. The track parameters can be evaluated locally within the group via:

$$R = \frac{1}{2} \sqrt{r^2 + \left(\frac{dr}{d\phi}\right)^2}$$

$$\phi_o = \phi - \sin^{-1} \left(\frac{r}{2R}\right)$$

$$t = z/r$$

where the numerical evaluation of the derivative requires several local measurements -- that's where the multiple wires are important. It is assumed that current division is used for z, if not, one can use the other two variables alone. Each wire group then has a rough measurement of the track parameters associated with it. We now repeat the MARK II track finding procedure, however, requiring that the sets of hits associated in pairs are only used if they have associated crude track parameters which are compatible. This will reduce very substantially the number of pairs which can be used since the errors on the crude track parameters are actually rather small compared to the typical separation of tracks in parameter space, as we shall see below.

Another alternative approach for the same chamber geometry would be to forget about point association in space altogether and deal with the crude track parameter measurements themselves as the data sample for each event. The scheme, for a multi-sense wire cell composed of wire triplets, would work as follows:[12]

(1) Cycle over triplets of hits.

(2) Each triplet (with current division), if the hits are compatible, yields a value of K, ϕ_o, t which is saved.

(3) The family of all "measured" K, ϕ_o, t values is then searched for clusters of closely spaced measurements which are then associated as belonging to one track. The space points yielding parameter space values in one cluster are then carefully fit in real space yielding the final track parameters. Track finding in this scheme becomes cluster finding in the three dimensional parameter space.

If we take wire triplets with sense wires separated by 1.2 cm, then one triplet gives errors whose order of magnitude is:

$$\delta K \simeq .02\text{m}^{-1}$$

$$\delta\phi_o \simeq 10\text{mrad}$$

$$\delta t \simeq 10\text{mrad.}$$

The intrinsic track separations in parameter space are typically much larger. Figure 11 attempts to display the expected results from pattern recognition for a simulated event for a chamber with 15 sense wire triplets with sense wire spacing = 1.2 cm, σ = 150 μm accuracy for the drift measurement, σ = 1.7 cm for the current division measurement. Although the two-dimensional projections are shown in the figure to help visualize the three-dimensional distribution, the distribution can be binned in three dimensions directly. In associating neighboring points into clusters, it is useful to note that, in the absence of backgrounds, the expected number of points in a cluster is predetermined by its parameters (e.g., 15 for tracks hitting all chamber layers). The clusters are easily picked out. The figure also indicates that the error on each parameter measurement, relative to the spacing of tracks in that parameter, is considerably smaller for the angular variables than for K. The presence of current-division thus provides a good extra constraint on the measured points for this type of scheme.

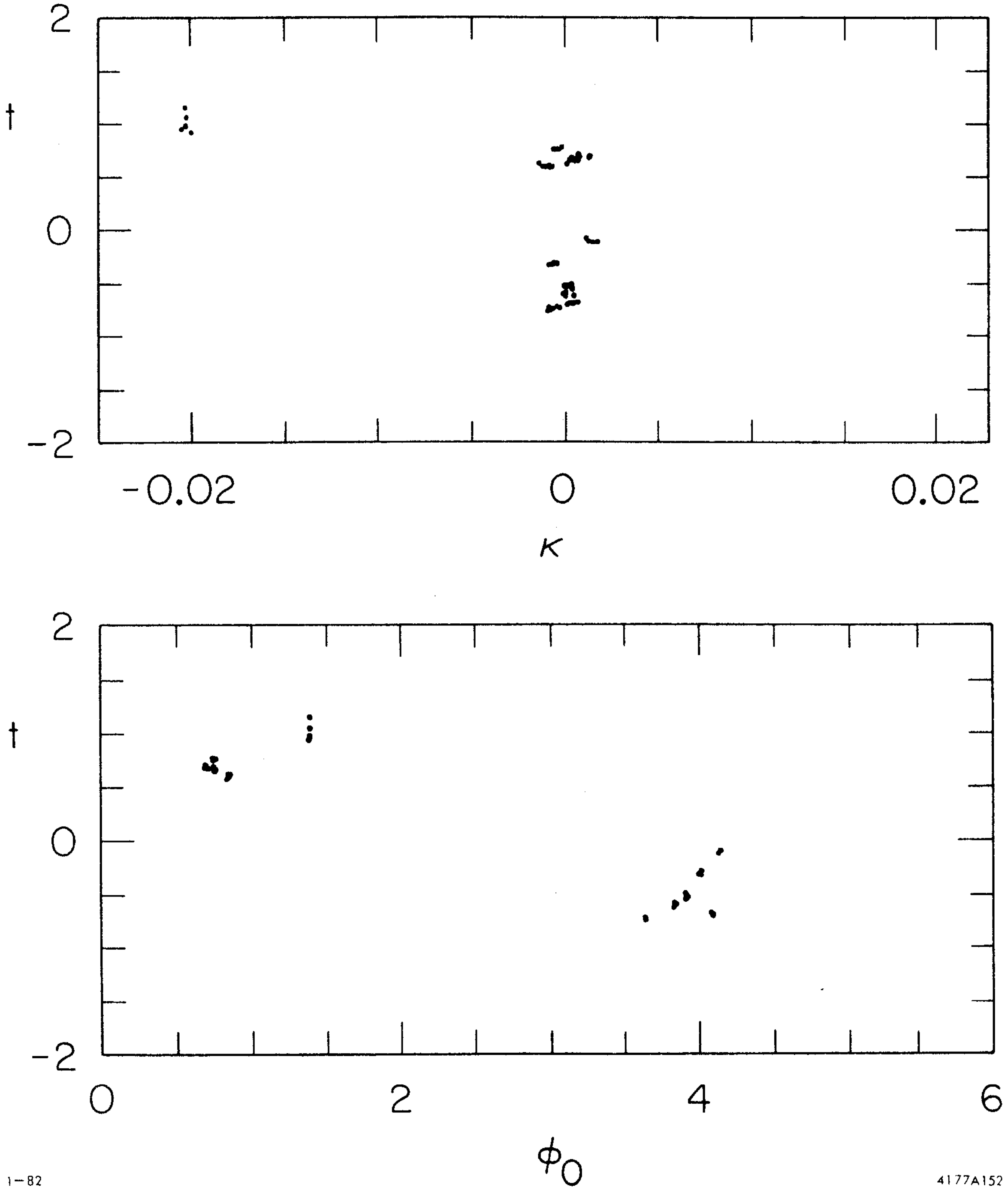

Fig. 11. Two dimensional scatter plots in parameter space for the triplet calculated crude track parameters for one low multiplicity event containing tightly bunched particles. Clusters have typically 15 associable points coming from one track.

REFERENCES

1. A good reference for presently operating detectors are the articles in Physica Scripta Vol. 23, 1981.
2. H. Ogren, S.L.C. Note #22
   H.F.W. Sadrozinski, S.L.C. Note #23
   J. Button-Shafer, S.L.C. Note #28.
3. H.F.W. Sadrozinski, S.L.C. Note #58.
4. J. Brau and G. Tarnopolsky, S.L.C. Note #41.
5. H. Lynch, S.L.C. Note #40.
6. P. Kooijman, S.L.C. Note #57.
7. G. Trilling, S.L.C. Note #13.
8. R. Fabrizio, S.L.C. Note #30.
9. J. Jaros, S.L.C. Note #51.
10. G. Baranko, S.L.C. Note #45.
11. J. Va'Vra, S.L.C. Note #12.
12. F. Grancagnolo, A. Seiden, D.B. Smith, S.L.C. Note #36.
13. R. A. Boie, et al., IEEE Trans on Nucl. Sci. NS-28, 603 (1981).
14. G. Trilling, S.L.C. Note #46.
15. K. Berkelman, Cornell Z^o Workshop, CLNS 81-490, p. 58.
16. J. Va'Vra and L. Roberts, S.L.C. Note #31.
17. The electrostatics and electron drift simulation program has been worked on by several individuals. Those responsible for various aspects of the program are: K. Bunnell, F. Grancagnolo, J. Jaros, Y. Unno, and J. Va'Vra.

SECONDARY VERTEX DETECTION AT THE SLC

I. Introduction

The vertex topology of a high energy e^+e^- interaction contains a wealth of information. These interactions copiously produce the τ lepton and hadrons containing the c and b quarks; all these particles decay within a millimeter or so of the primary interaction point, giving these interactions a rich secondary (and tertiary!) vertex structure. With suitable detectors, one can hope to reconstruct these vertices and so tag events with τ's, c's and b's; measure lifetimes and mixing angles; and perhaps directly measure the flavor of c and b jets. The spatial resolution and track-pair resolution required of such detectors demand detector development, but several techniques, including solid state microstrip and CCD detectors, pressurized drift chambers, and holographic bubble chambers look promising. The art of secondary vertex detection at fixed-target machines is maturing rapidly, and a variety of techniques including emulsion stacks, high resolution bubble chambers, high pressure streamer chambers and microstrip arrays have been used to tag charm decays and measure lifetimes. Vertex detection in the colliding beam environment is a newer twist, but has already yielded a measurement of the τ lifetime. The SLC, with its micron-sized beam and one-centimeter sized beam pipe is uniquely suited for these studies. Compared to conventional storage rings, it offers a well-defined and minute primary interaction point, the possibility of locating a detector within a centimeter of the interaction (an order of magnitude improvement over LEP), negligibly thin beam pipes, and a repetition rate low enough to permit novel detectors and readout schemes.

This report will summarize the secondary vertex detection studies done in the course of the SLC Workshop. It is organized as follows: Section II discusses the physics accessible with vertex detectors. Section III depicts the physics environment at 100 GeV - particle multiplicities, momenta, angular correlations, and topologies of charm decays. The fourth section sketches the elements of a vertex detector, and, through some model studies evaluates the spatial resolution and track-pair resolution requirements. Section V summarizes the detector technologies which seem most promising for vertex detection. Concluding comments are presented in Section VI.

II. Physics Possibilities (1)

The physics one would hope to do with a vertex detector would include:

1) Lifetime measurements
2) Tagging c and b decays
3) Determination of weak mixing angles
4) Neutral current coupling measurements
5) Gluon and quark jet studies
6) New particle searches

The lifetimes of the τ, charmed mesons and baryons, and the mesons and baryons containing the b quark may all have been measured when the SLC turns on. However, the abundant production of these states at the Z^0 may permit new levels of precision in these measurements. For example, the τ lifetime is expected to be 2.8×10^{-13} sec.(2) It can be written as

$$T_\tau = \frac{B\left(\tau \to \nu_\tau e \bar{\nu}_e\right)}{\Gamma\left(\tau \to \nu_\tau e \bar{\nu}_e\right)} \quad ,$$

where the partial width $\Gamma(\tau \to \nu_\tau e \bar{\nu}_e)$ can be computed in terms of the coupling of the τ to the charged weak current. Accurate determinations of the τ lifetime will test the universality of the lepton coupling. Since the interaction point and the decay point can both be known at the SLC with high precision, it should be possible to measure the τ-couplings to the per cent level or better with low systematic errors. Since the b mesons and baryons are expected to have their decays Cabibbo-suppressed in the K-M six quark model(3), their lifetimes should be roughly comparable to charmed mesons and baryons. Lifetimes in the range 2×10^{-13} to 10^{-14} sec have been derived by several authors(4) using measured quantities like the CP violation parameter ε in K_L^o decay to estimate the K-M angles. They are unlikely to have been measured elsewhere and might be possible at the SLC. The production rate is expected to be high at the Z^o (greater than at Υ''', for example), the boost substantial, and the primary vertex position well-known, so the measurement possibilities at SLC are enhanced. Measurements of the b lifetimes should allow tests of enhancement mechanisms involving spectator quarks. Mesons and baryons containing the t quark, if they should be produced, are expected to be Cabibbo-allowed and enhanced by a factor m_t^5. Lifetimes in the neighborhood of 10^{-18} s are expected, so direct measurement looks impossible.

The efficiency of a secondary vertex detector in tagging events with separated vertices depends on aspects of the physics of these events which are not well known: fragmentation functions, charged particle multiplicities in c and b jets, lifetimes, etc. As we see below, however, preliminary Monte Carlo studies of charm tagging look promising, albeit technically challenging. Such a tag could, first of all, measure the flavor of the leading quark when $Z^o \to b\bar{b}$ or $Z^o \to c\bar{c}$. B decays could be distinguished by their high multiplicity, the high invariant mass of the charged secondaries, and their frequent association with charm decays. Such a tag would aid in reducing the combinatorics problems in invariant mass combinations and would allow direct measurements of semi-inclusive lepton and proton yields in the decays.

If the event topology can be cleanly reconstructed, one can determine the K-M angles and explore their relationship to the quark masses. One would directly measure the fraction of times b decays into c and into u. Similarly, if $Z^o \to t\bar{t}$, one can study the relative branching ratios for $t \to b$, $t \to s$, and $t \to d$.

Both the vector and axial vector couplings of the c and b quarks to the weak neutral current can be determined once the leading quarks have been identified. The total rate $\Gamma(Z^o \to q\bar{q})$ measures $(a_q^2 + v_q^2)$ and, if the quark jet can be distinguished from the antiquark jet, the forward-backward asymmetry measures $a_q v_q$ according to

$$A_{FB} = \frac{3a_e v_e a_q v_q}{(a_e^2 + v_e^2)\ (a_q^2 + v_q^2)} \quad .$$

Jet studies should benefit from jet flavor identification. It should be possible to deduce the c and b fragmentation functions and search for the associated production of $c\bar{c}$ or $b\bar{b}$ from the sea. A double tag in a three jet event would, by elimination, isolate the gluon jet.

New particle searches at the Z^o can be significantly aided by vertex detection. The Higgs mesons are presumably responsible for generating the masses of elementary particles, so their appearance or non-appearance will be of great importance in determining the nature of symmetry-breaking. Unitarity bounds the Higgs mass from above at 1.2 TeV, but there is essentially no lower bound.(5) Since the coupling of the Higgs to x is proportioned to m_x, one expects it to decay to the heaviest particles it can. Thus, perhaps

$$H^o \to \tau^+\tau^-,\ c\bar{c},\ b\bar{b},$$

$$\text{or } H^- \to \tau^-\nu_\tau,\ \bar{c}s,\ \text{etc.}$$

and the Higgs decays can be tagged by secondary decay vertices.

The alternative scheme of dynamical symmetry breaking(6) would also involve decays that could be tagged by a vertex detector. At the Z^o one would expect $Z^o \to \Pi_T \Pi_T$ at a 1% level, and the technipions (or hyperpions) would again decay to the highest mass available:

$$\Pi_t \to t\bar{b},\ \bar{b}c,\ \bar{c}s \quad .$$

Whatever the situation, a vertex detector will be extremely helpful in disentangling it.

Finally, vertex detectors will be sensitive to the decays of new particles with lifetimes in the range 10^{-9} to 10^{-14} sec. Since any particle with weak or electromagnetic couplings and mass < $m_{Z/2}$ will be produced at the Z^o, we may hope for some surprises.

III. The Physics Environment (7)

What sort of detector is needed to see secondary vertices? Tracks emerging from decay vertices will appear to miss the primary vertex by an impact parameter of order $c\tau$, where τ is the lifetime of the decaying particle. As the following table shows, these impact parameters will be in the 10 - 100 μ range for the particles of interest.

Particle	$\bar{b} \approx c\tau$ (μ)
τ	75
D^o	75
D^+	200
B	3 - 300 ?

Clearly track resolutions below 50 μ will be necessary to catch these decays, and additional resolution is essential to depict complex events cleanly. The detection problem is complicated by the high track density expected in jets at the Z^o; good track-pair resolution is needed in a vertex detector. To quantify these detector requirements, we have undertaken Monte Carlo studies of $Z^o \to c\bar{c}$ using the 'standard' SLC development Monte Carlo. It uses the Ali fragmentation procedure to produce 2, 3, and 4 jet events. For the purpose of this study, the D^o and D^+ lifetimes were set to 3.1×10^{-13} s and 9.5×10^{-13} s respectively.

Some of the general features of the events are shown in Figures 1a, b, and c. The momentum spectrum of the decay products of the D's are expected to be fairly hard compared to hadrons generally. Figure 1a shows the spectrum for D decay products; figure 1b shows the spectrum of all charged tracks produced when $Z^o \rightarrow c\bar{c}$. The average momentum of the D decay products is 2 to 3 GeV/c. Even decay products coming from the cascade decays of B mesons, shown in Fig. 1(c), are relatively hard. Multiple coulomb scattering errors, depending on particle momentum, are thus relatively unimportant at the SLC compared to storage rings at lower energies.

Placing a detector within 1 cm of the interaction point at Z^o energies has its own problems, however, as shown in Fig. 2. The probability that a decay product from a D overlaps with another track is shown as a function of the track separation for a detector 1 cm from the interaction. Twenty per cent of the secondaries have another track within 100 μ in the familiar axial geometry where only ϕ coordinates are readout; adding a second coordinate to the readout helps considerably, but the segmentation requirements are still severe. A one dimensional (i.e., ϕ coordinate) system needs to resolve tracks separated by 5 mr.

The distribution of impact parameters for the secondaries in both charged and neutral D decays is shown in Fig. 3(a). Figure 3(b) shows the distribution of the largest impact parameter per D decay. A typical decay has at least one charged track with an impact parameter of order 100 μ ; but, of course, there are decays with very short flight paths and decay products which deviate very little from the primary interaction vertex. Since both the typical decay angles in the laboratory and the average flight path scale with the energy, the distribution of impact parameters is essentially Lorentz invariant. Thus Figures 3(a) and 3(b) are an appropriate guide to all relativistic D

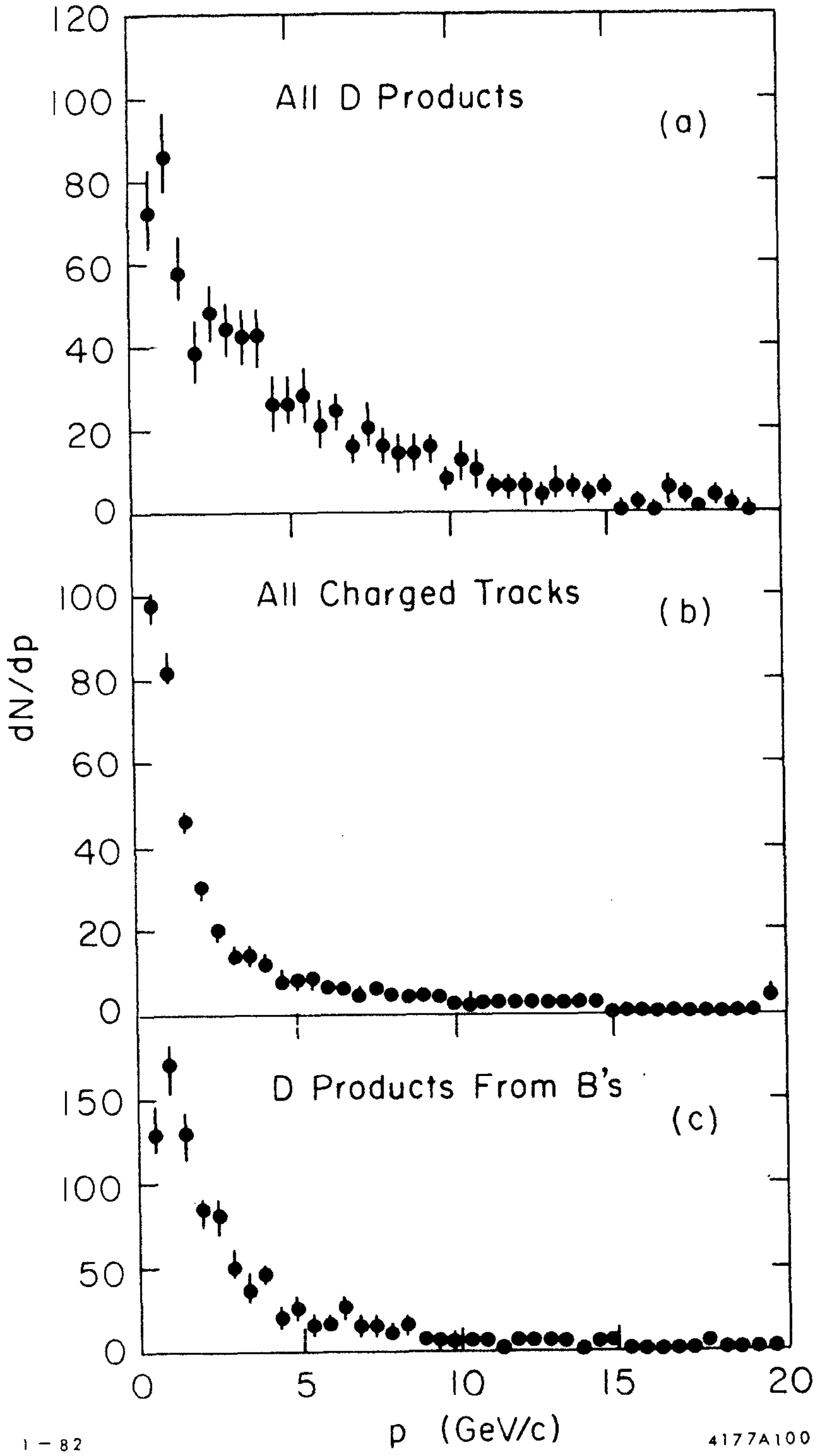

Fig. 1. Estimated momentum spectrum of (a) charged decay products from D mesons produced in $Z^0 \to c\bar{c}$ jets; (b) all charged tracks produced in $Z^0 \to c\bar{c}$; (c) charged decay products from D mesons produced in $Z^0 \to b\bar{b}$, with subsequent $b \to c$ decays.

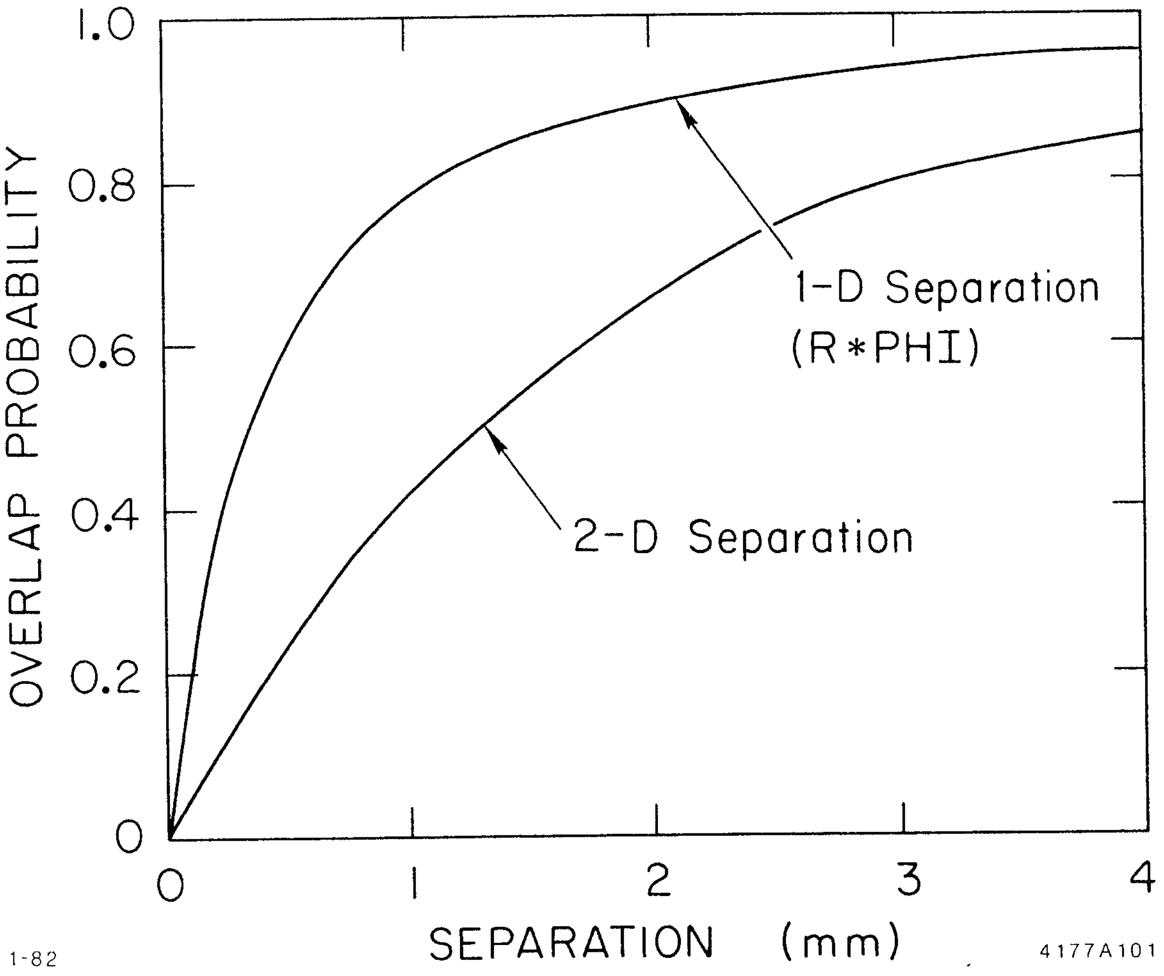

Fig. 2. Probability that a track from a D decay overlaps with another track as a function of track separation for a detector 1 cm from the interaction point.

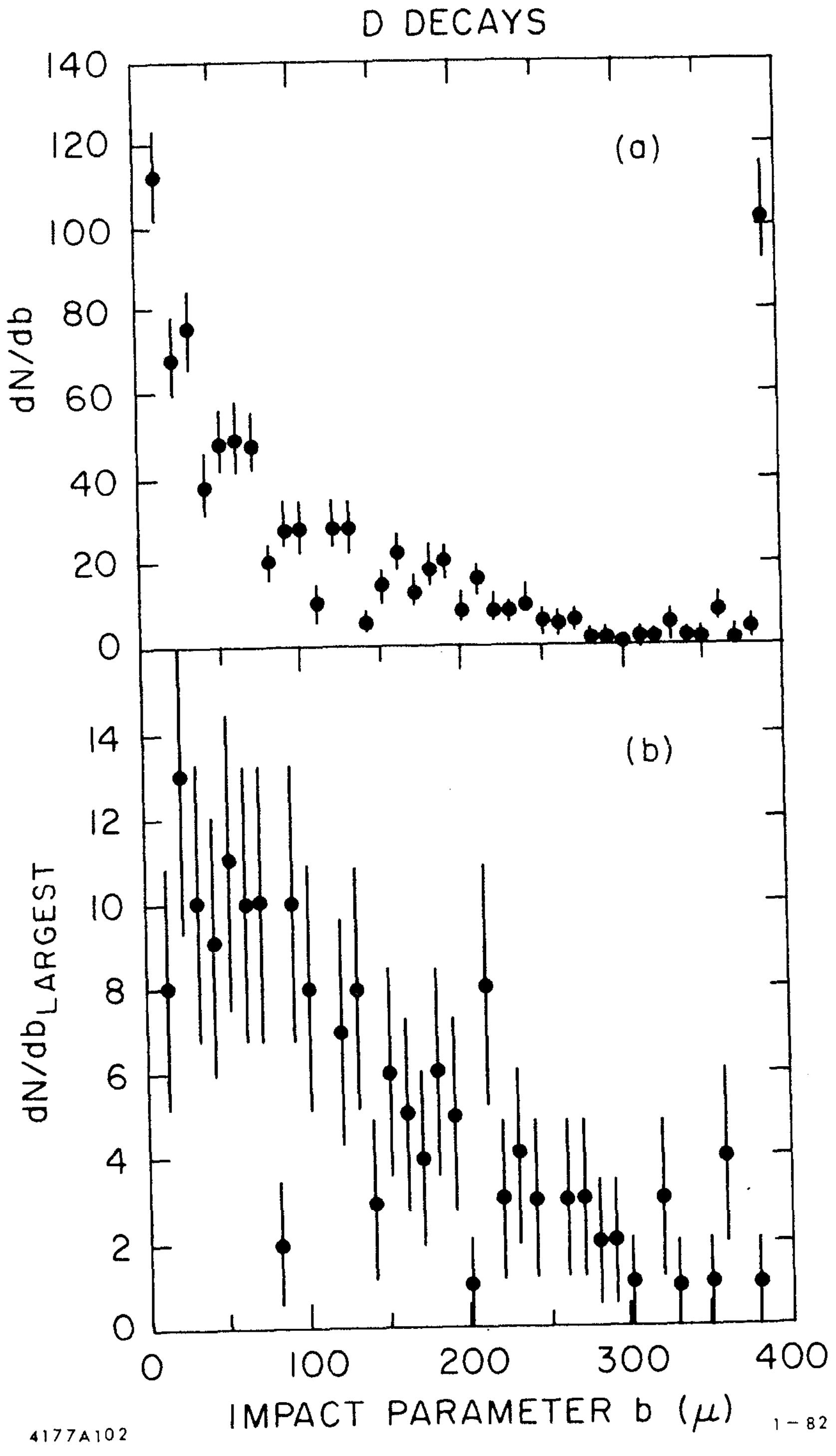

Fig. 3. (a) Distribution of impact parameters for all tracks from D decays; (b) distribution of the largest impact parameter per D decay.

decays, irrespective of their source. Other processes like $K^{\pm}$, K^o_S, and hyperon decays will also make tracks with large impact parameters, so this simple charm decay signature isn't perfectly clean.

IV. Detector Requirements for D Tagging

The figure of merit for a vertex detector is the expected error on a track which has been extrapolated to the vicinity of the primary vertex. This error has essentially two components, one due to multiple coulomb scattering in the material in the detector and beam pipe, and the other arising from the extrapolation procedure and finite measurement errors. For simplicity we consider a detector which measures a track at two radii, r_1 and r_2, with measurement errors σ_1 and σ_2. The error on the extrapolated track σ_x can be written

$$\sigma_x^2 = \sigma_{MCS}^2 + \sigma_{CH}^2$$

where the measurement error from the chamber is

$$\sigma_{CH}^2 = \left(r_1{}^2\sigma_2{}^2 + r_2{}^2\sigma_1{}^2\right)\Big/\left(r_2-r_1\right)^2 \quad \text{and}$$

the error from multiple coulomb scattering is

$$\sigma_{MCS}^2 = \int_o^{r_1} r^2 d\theta^2 + \frac{r_1{}^2}{\left(r_2-r_1\right)^2}\int_{r_1}^{r_2} (r_2-r)^2\, d\theta^2 \quad .$$

In these expressions $d\theta^2$ is the differential mean square multiple coulomb scattering angle coming from material between r and r + dr. We take

$$d\theta^2 = \left(\frac{.015}{p\beta}\right)^2 \frac{dr}{x_o} \qquad \text{(P in GeV/c)},$$

where x is the radiation length of the material at radius r.

What resolution is required for vertex detection? How efficiently can D's be tagged? How much material can be tolerated in a vertex detector? To begin to answer such questions we have Monte Carlo'd the response of the simple detector outlined above.(8) It consists of track detectors at two radii, 1 and 2 cm. We assume its first plane dominates the multiple scattering, which is likely since small beam pipes can be made quite thin, and consider its performance as a function both of its thickness (in radiation lengths) and its resolution. We assume the device has perfect track-pair resolution. We tag D's by looking for tracks which miss the interaction point significantly, where we take the ratio of the measured impact parameter and the extrapolated error, b/σ_x, as a measure of the significance of the miss. Figure 4(a) shows how the tagging fraction depends on this quantity for various detectors. When $\sigma_x \approx 10\ \mu$, 70% of all D decays have charged tracks which miss the origin by at least 3 standard deviations. Figure 4(b) shows what fraction of the tracks which miss the origin are actually from D decays. In the example above, about 80% of the 3σ misses are from D decays.

The simple tag discussed above is not optimal -- one can do better by looking for correlated misses or actually reconstructing vertices and looking for events where they are significantly displaced from the origin. But we hope it is instructive. The figures show that the cleanliness of the D sample and the efficiency of the D tag improve markedly with resolution. In the example, a spatial resolution of at least $10\ \mu$ is called for at each detection plane; this corresponds to an extrapolated track resolution, σ_x, of about 25 μ. As long as the multiple scattering error is less than or at worst comparable to this level, obviously the resolution won't suffer too much. A 300 μ silicon wafer has $x/x_0 \approx .004$; the multiple scattering error is just

$$\sigma_{MCS} = 10^{-3}\ r_1 \,/\, P(\mathrm{GeV/c}),$$

and is thus negligible in the examples shown in the figures. Multiple scattering does limit resolution, however, and its effects are obviously more noticeable if a detector plane cannot be placed so close to the interaction point.

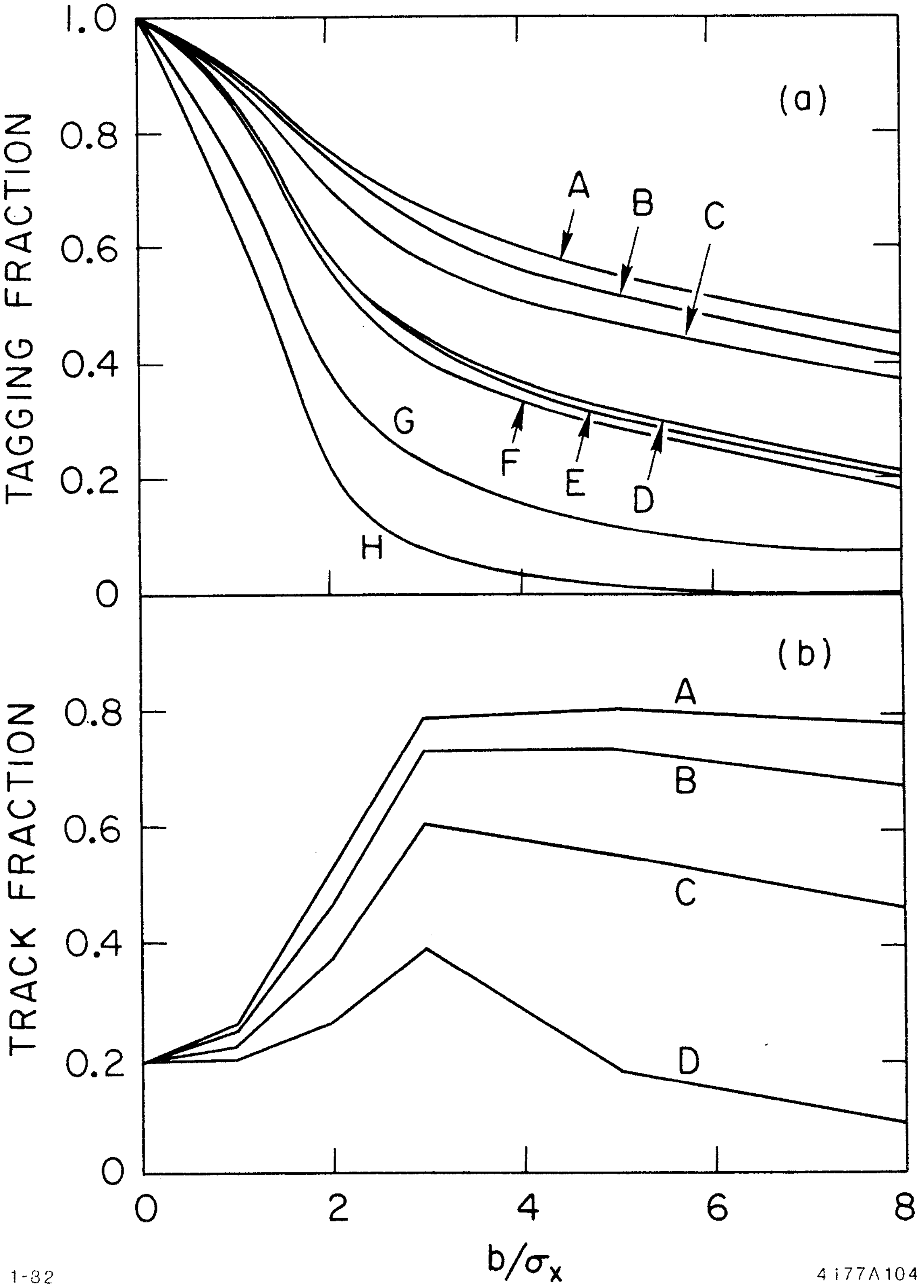

Fig. 4. (a) Fraction of D decays which can be tagged vs b/σ_x, the number of standard deviations by which a track misses the origin. Curves A thru H label different combinations of detector resolution (in microns) and thickness (in radiation lengths): (A) 3μ, .001; (B) 3μ, .004; (C) 3μ, .016; (D) 10μ, .001; (E) 10μ, .004; (F) 10μ, .016; (G) 30μ, .016; (H) 100μ, .016.

(b) Fraction of tracks which miss the origin that come from D decays vs b/σ_x in $Z^0 \rightarrow c\bar{c}$ events: (A) 3μ; (B) 10μ; (C) 30μ; (D) 100μ.

In summary, a vertex detector should have extrapolated track resolution at the 25 μ level or better to study charm decays. Spatial resolution is at a premium here; greater resolution will significantly improve tagging efficiency and will probe shorter lifetimes. Equally important, a vertex detector must have track-pair resolution at the 100 μ level; specifically, an axial device should resolve particles separated in azimuth by 5 mr. A detector with two dimensional segmentation should resolve tracks separated by more than 25 mr. There are other general considerations in vertex detector design. It is essential that tracks seen in the tracking chamber can be reliably linked to the tracks reconstructed by a vertex detector. This is necessary so that track curvature corrections can be applied, momentum dependent errors evaluated, and particular particles associated with particular vertices. From the standpoint of the general tracking chamber, it is important that the entire vertex detector present little material to the emerging tracks, to minimize conversions, interactions, and multiple scattering.

V. Detector Technologies

Several techniques show promise in meeting the ambitious requirements outlined above. None of them is mature; vertex detection at colliding beam devices especially is a new development and the bugs have yet to be discovered, let alone worked out. Recently, there has been substantial progress with solid state detectors, both CCD's and strip-array devices. Much of this work has been motivated by the development of fixed target vertex detectors. Optical techniques, especially small, high precision bubble chambers, are being used as fixed target vertex detectors for charm studies. Small chambers have been operated at 90 expansions per second, not far from the 180 Hz operation of the SLC. Drift chambers have achieved 10 - 20 μ resolutions in pressurized gases and should also be adaptable to vertex detection. In the following, we discuss these approaches in more detail and attempt to summarize their performance limits, strengths and weaknesses.

a. Solid State Micro Strip Detectors[9]

The "typical" detector shown in Figures 5a and 6 is hexagonal in shape with four planes per side, the inner 2.5 cm and the outer 5.5 cm from the beam. Slots are opened every 120° to permit extraction of leads for coordinates transverse to the beam, and Z-coordinate leads are taken from both ends of the 15 cm long detector. A magnified view of one end of the detector is shown in Fig. 6. Strips are spaced at a 30 micron pitch, and by employing the technique of charge division only every fifth strip need be read out. Spatial resolution will be comparable to that obtained by reading out every strip provided amplifier noise is kept below 0.2 femtocoulombs, and fewer than 12% of the tracks will be masked by having double hits in the 150 micron region between readouts. The number of readout amplifiers could be limited to approximately 16,000 by wire-bonding mosaics of silicon detectors, as shown in Fig. 5b.

The detectors radially are quite thin. Four detectors (each 300 microns thick) comprise only 0.013 radiation lengths, and would convert only 1/4 gamma per interaction.

Present detectors are unaffected by 10^{13} minimum-ionizing particles/cm^2, but an equivalent flux of heavily ionizing particles would be catastrophic.

Below neutron production threshold, detectors have received x-ray dosages of as much as 10^9 rem without serious consequence. By switching to P-type silicon (present designs are based on N-type) it may be possible to increase detector radiation resistance by another order of magnitude. However, as receipt of the full beam would be fatal, these detectors must be protected.

Two small high-resolution detectors have operated successfully in a beam at the single detector level; precision track-fitting has yet to be demonstrated. Heijne of CERN has measured minimum ionizing tracks through a 0.5 x 3.0 cm

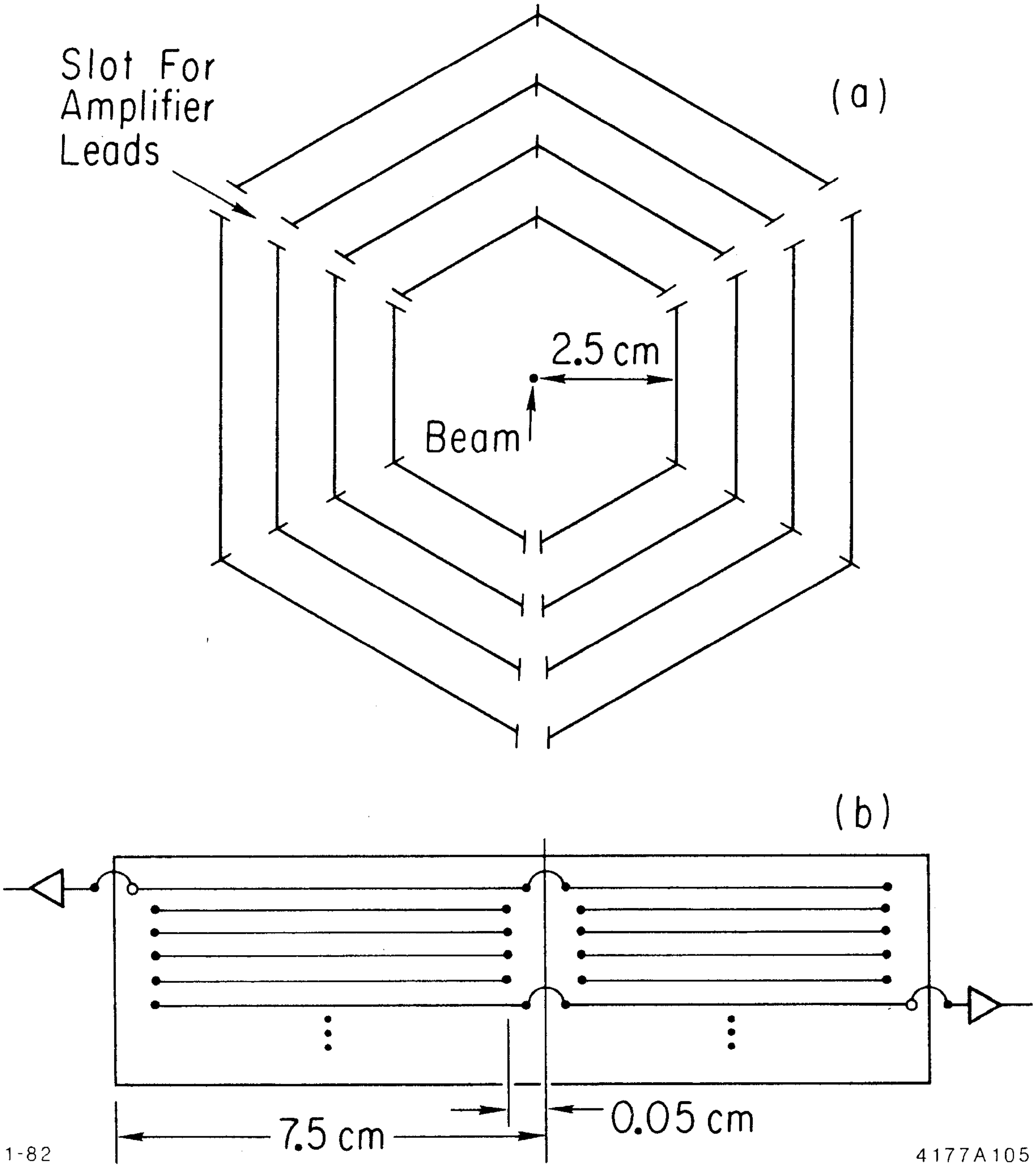

Fig. 5. (a) "Lifesize" end view of vertex detector assuming double-sided planes. The length of the detector along the beam should be 15 cm. (b) A wire-bonded mosaic of silicon wafers forms a larger detector requiring fewer amplifiers.

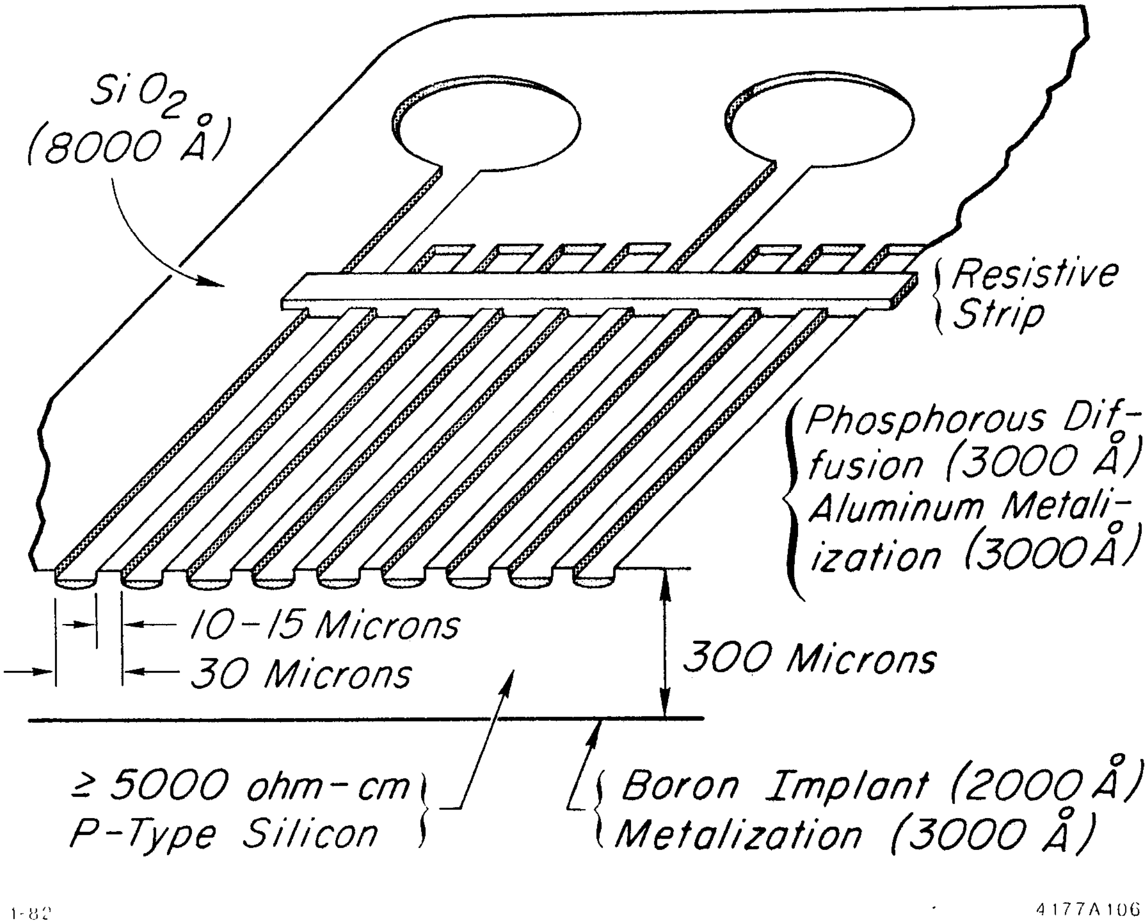

Fig. 6. Cut-away view of a micro-strip detector.

detector with 50 micron pitch in which every wire is read out. The devices are made by ENERTEC using 300 micron thick N-type wafers and 2 inch silicon technology.(10) The Hyams group has tested a 2.5 x 3.5 cm device with 20 micron pitch in which every third strip in the central region and every sixth strip in the wings is read out and capacitive charge division is employed to obtain spatial resolution. This detector was made by Centronics, Ltd. using 2 inch technology on 300 micron thick wafers of N-type silicon.(11)

Concerning electronics, cheap hybrid amplifiers have been developed which have 0.1 femtocoulomb "stand-alone" noise, and 0.2 femtocoulombs noise when connected to the detector. Work on this front still is progressing; very little has been done on making enormous numbers of low-mass connections between detectors and amplifiers, and on multiplexing the extensive number of signals into computers. However, a mass production cost between detector and computer of $50/strip appears feasible. For the long range future, several manufacturers have expressed preliminary interest in developing the tiny amplifier-plus-multiplexed readout systems which could be wire-bonded onto the detector. Lecroy already has developed a suitable prototype integrated amplifier and expects to have prototype analog multiplexing chips by May, 1982. "On-board" amplifier-plus-readout systems would vastly reduce the number of connections needed external to the detectors and would have less noise, permitting the use of somewhat thinner wafers.

The performance of the detector is summarized in Table I.

b. CCD Particle Detectors[12]

Interest is growing in the use of commercial charge-coupled devices as very high resolution particle detectors. A typical CCD is a matrix of semiconductor detectors several hundred on a side, each of order 20 μ x 20 μ, all placed on a single substrate. Thus a CCD offers the sort of segmentation required by the high particle densities at the SLC. CCDs are read out serially, which keeps the number of external connections to an absolute minimum at the expense

TABLE I

Comparison of Possible Vertex Detectors

	μ STRIP	CCD	BUBBLE CHAMBER	DRIFT CHAMBER
σ PER MEAS.	9 μ	3-9 μ	5-10 μ	10-20 μ
σ_{MCS} xP(GeV/c)	40 μ	10 μ	10 μ	7 μ
σ_x (@ 2 GeV/c)	20 μ	10-20 μ	15 μ	15-25 μ
TRACK-PAIR RESOLUTION	150 μ	60 μ	50 μ	200 μ
READOUT DIMENSIONS	1d	2d	3d	1d
THICKNESS (x/x_o)	1-2%	1-2%	5%	1/2%
RADIATION HARDNESS	SOFT	SOFT	HARD	MODERATE
POTENTIAL PROBLEMS	16K CONNECTIONS	CHIP-TO-CHIP REGISTRATION READOUT SPEED LIVE AREA FRACTION	REP RATE VIBRATIONS VISUAL SCAN	SEGMENTATION 100ps TIMING

of readout time. However, readout times are comparable to the 5.5 ms available between pulses at the SLC for even the largest arrays now commercially available. Serious development of the device as a minimum ionizing particle detector is just beginning, and results so far are preliminary.

Commercially available CCDs range in size up to 1.2 cm × 1.2 cm device which has been developed for the Jet Propulsion Laboratory of Cal Tech for optical imaging. This device has 15 μ × 15 μ pixels in an 800 × 800 array. The silicon substrate is about 200 μ thick, but only the depleted region, of 10 μ depth, is useful for charge collection. About 1000 electrons are generated when a minimum ionizing particle passes through the depletion layer; this signal is small enough that refrigeration to about 200° K is necessary to reduce thermal noise to an acceptable level. Noise levels well below the 50 electron level are expected, so the device should be efficient. The so-called channel stops demarcate the pixels in a CCD and obscure perhaps 10% of the surface area. The efficiency for detection in this channel stop area has not yet been measured. There is an additional 10 - 20% dead area associated with the readout function of the chip. The ionization electrons are expected to diffuse by about 20 μ as they are collected. This limits the track separation ability of such a device to about 60 μ, but may actually enhance the resolution. Monte Carlo(13) studies suggest that 3 μ resolution is possible if one uses the charge distribution observed in several cells to center-find. The radiation hardness of some CCDs is comparable to that for solid state strip arrays; total fluxes of order 10^{13} min ions / cm^2 can be tolerated.

A vertex detector built up of several hundred CCDs arranged in several layers around the interaction point would have excellent track-pair resolution. The extrapolated track resolution would be multiple scattering limited to

$\sim 10\ \mu$ level. The overall thickness of the detector would be a few per cent of a radiation length. Radiation damage occurs at the 10^5 rad level, so the device must be shielded. A rather serious question is whether the devices work well in magnetic fields. There are, of course, many other open questions: how efficient is the device? what resolution will be realized? how quickly can a high resolution device be read out?

c. Holographic Bubble Chambers[14]

The low repetition rate of the SLC admits detection techniques unfamiliar in colliding beam physics. One novel idea is to adapt rapid cycling bubble chambers for SLC work. By employing holographic readout techniques, very high resolution tracking would be possible throughout the volume of the device. The potential information storage capacity of a visual device is immense, easily equal to the high track density of jets at Z^0 energy. Pattern recognition should be unambiguous and relatively easy.

A conceptual design for a bubble chamber vertex detector is given in Fig. 7. The chamber would surround the 1 cm radius beam pipe and run with propane at 50° C and 20 atmospheres. Figure 8 shows how chamber illumination could be arranged. The fiducial volume would be a cylindrical shell of liquid, 1 cm thick radially, and 5 cm long. The entire device would be 5% of radiation length thick.

Rapid cycling chambers somewhat larger than considered here have operated with hydrogen at $\sim$ 50 Hz, and even briefly at 900 Hz. The propagation of the pressure wave is slower in propane, and even slower in another possible filling, helium, but calculation suggests that for a chamber of the size considered, uniformity of pressure should be adequate in these liquids. Nonetheless rapid cycling has yet to be demonstrated adequately in propane and helium. It must also be achieved with small bubbles and with a large number of bubbles per unit length. Although the transmission

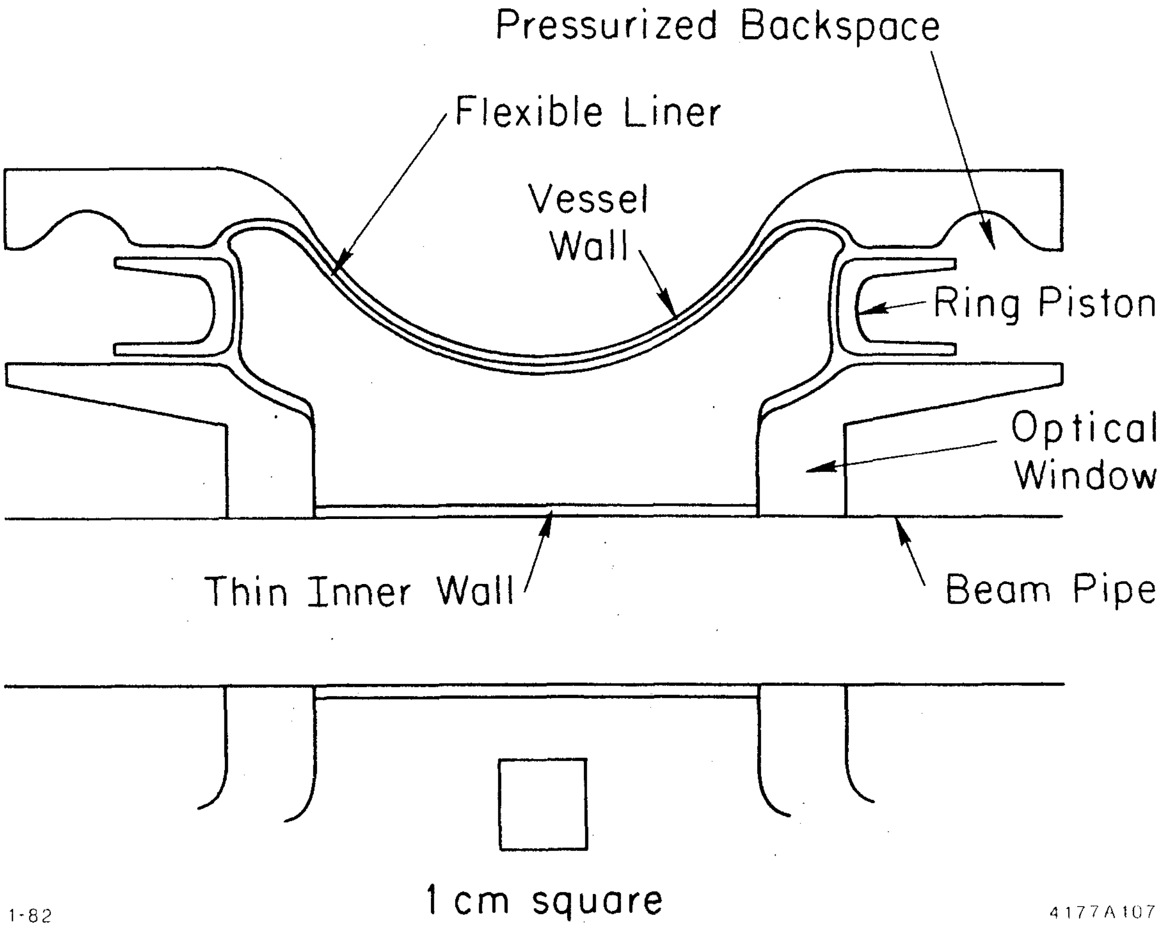

Fig. 7. Conceptual design of a propane bubble chamber vertex detector.

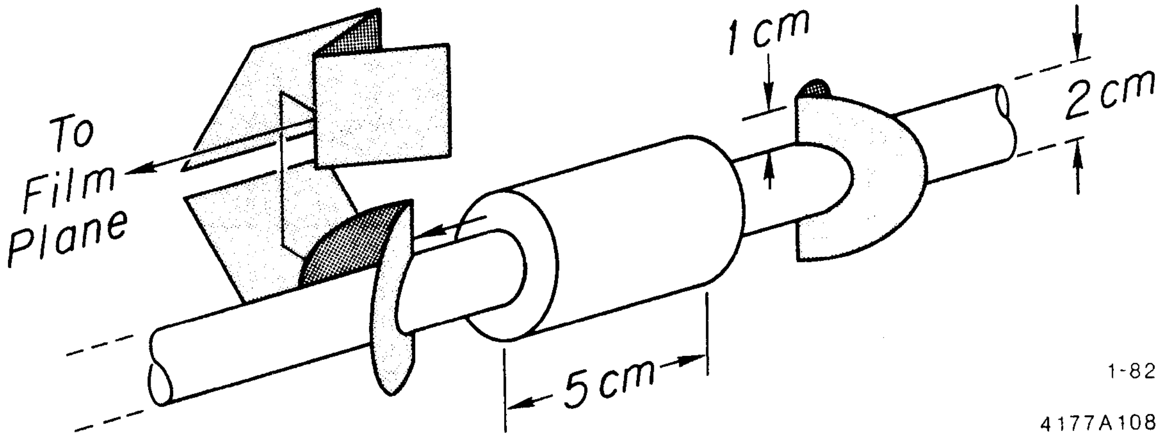

Fig. 8. Illumination of a bubble chamber vertex detector.

of vibrations from chamber expansions to beam magnets is potentially worrisome, it can be eliminated by properly distributing the mass and using couplings with the right frequency response.

Propane, hydrogen, and helium chambers have been considered. In propane, the operating point of $\sim 50^{\circ}C$ allows the use of flexible materials and relatively easy bench development. The need for 20 atmospheres pressure is a major drawback both from the point of view of the more massive expansion system and the scattering in the containment vessel. The cryogenic chambers complicate the design of optics, especially so in the case of helium which would need multiple radiation shielding. Hydrogen, operating at $\sim$ 10 atmospheres, also requires a substantial pressure vessel, with the added complication of a high pressure bellows design for the equivalent of a piston. The beam pipe is the major complication here, since a piston in the form of a ring, coaxial with the beam, seems most practical. This requires bellows at the inner and outer radii, which must not interfere with the optical path. In many ways helium is the most attractive medium, but the least understood. It requires pressures $\lesssim 1$ atmosphere and is not explosive. Its major difficulty is the $3^{\circ}K$ operating point and its very small heat of vaporization. For a small chamber with a high surface to volume ratio, refrigeration design would be challenging. Multiple cooled layers of refrigerant might be needed, removing the advantage of thin pressure vessel walls, but retaining the relative ease of constructing the low pressure bellows.

Figure 9 shows the extrapolated track resolution in hydrogen and propane fillings as a function of the thickness of liquid used in the measurement. It's assumed that 10 measurements are made, equally spaced along the trajectory. Resolutions in the 10 - 20 μ range look possible. Bubble chambers have achieved track widths of 20 μ and setting errors in the 5 - 10 μ range, as assumed in the figure.

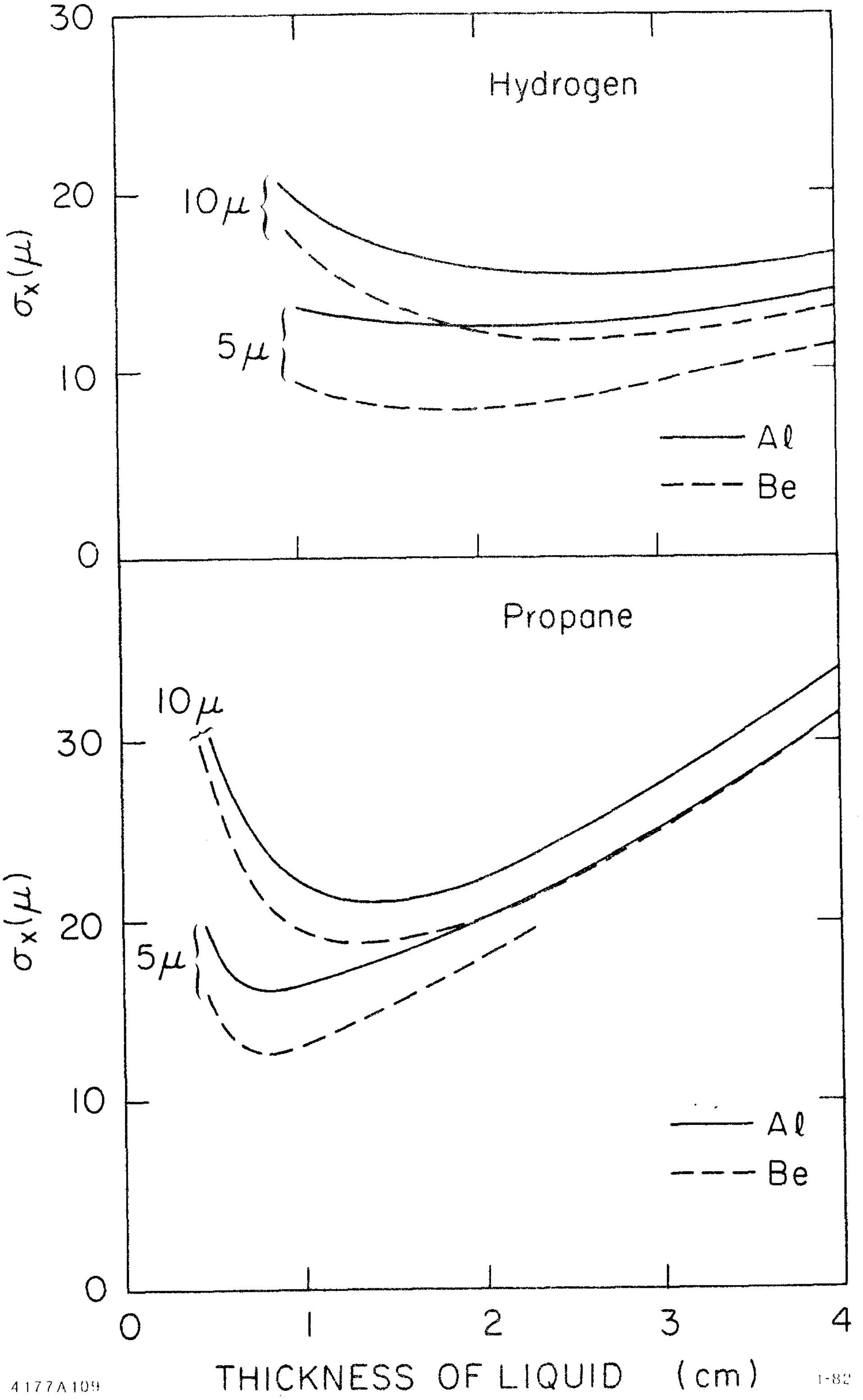

Fig. 9. Extrapolated track resolution vs thickness of liquid used in the measurement in hydrogen and propane. The resolution is shown for both aluminum and beryllium pressure vessels and for both 5 and 10μ setting errors.

The strengths of the technique are the high spatial resolution and tremendous information density. The track-pair resolution is superb; it would allow the device to be placed within a millimeter or so of the interaction region, if it were possible to avoid synchrotron radiation backgrounds. Moving the chamber closer than the 1 cm radius considered above could improve the extrapolated track resolution to 5 μ or so. The device is radiation hard; a beam dump near the chamber would not be catastrophic. It would, however, be susceptible to moderate fluxes of MeV photons, especially if heavy liquids are used. These properties are summarized in Table I.

d. Drift Chamber Vertex Detectors (15)

The high spatial resolution and track-pair resolution requirements for vertex detection would seem to exclude drift chamber techniques from consideration. Most large drift chamber systems have ∼ 200 μ resolution and can only resolve tracks separated by 5 mm or more in space. These limits are not fundamental, however, and recent work has demonstrated that 10 - 20 μ resolution, and track-pair resolution of at least 1000 μ is possible in small chambers with pressurized gases. Computer studies indicate further improvements in track-pair resolution are possible. The very low mass and radiation hardness of gas detectors make them suitable for vertex detection.

One possible geometry would be a miniature Jet Chamber. Twenty-four pie-like segments would make up a cylindrical chamber roughly 10 cm in diameter and 15 cm long. Each segment would have axial sense and field wires strung in a plane. Cathode wires or thin foils could be used to isolate one segment from another. The sense wires would be spaced on 2 mm centers; larger diameter field wires are placed between the sense wires and serve both to collect unwanted ionization and to shield one wire from another. The cell would be active between r = 2.5 and 5.3 cm. Multihit electrons with 50-100 ps resolution records the hits from each of the wires in the system. The chamber is pressurized to 3 atm with an organic gas.

Two factors limit track-pair resolution in drift chambers. First, not all the electrons created along a charged particle's track are collected at once. Instead their arrival times reflect just where they were created. Figure 10 shows a computer simulation of these electron arrival times for two tracks separated by 500μ in space and about 5 mm from the sense wire. Although most of the signal is concentrated in the first few nanoseconds occasionally an electron can arrive as much as 8 ns late. Obviously, the electrons from one bunch can't overlap the other if we are to distinguish (and time) two separate tracks. The track-pair resolution of this example is in the 300 μ range and is achieved by accepting ionization from only a small segment of the track. The second factor is equally fundamental. The current pulse from a drift chamber has a 1/t tail, which if not suppressed, will cause one pulse to overlap with the next. However, electronic solutions to this problem have been demonstrated by the use of zero pole filters.(16) Figure 11 shows the response of such a circuit to the pulse depicted in the previous figure. The response was generated assuming a preamplifier with 2 ns risetime, two zero pole filters and the gaussian integration with FWHM = 8 ns as designed by R. A. Boie et al. It allows clean separation at the 500 μ level; further improvement to 200 μ should be possible.

Spatial resolution in large drift chamber systems is frequently limited by systematic effects: wire placement inaccuracies, calibration problems, and the difficulty of extracting a space-time relation. The fundamental limits imposed by ionization statistics and diffusion have been approached in small chambers, however, and resolutions in the 10 to 20 μ range have been reported in organic gases at several atmospheres pressure.(17) Monte Carlo calculations(18) of resolution in small drift cells are given in Fig. 12 for a variety of gases,

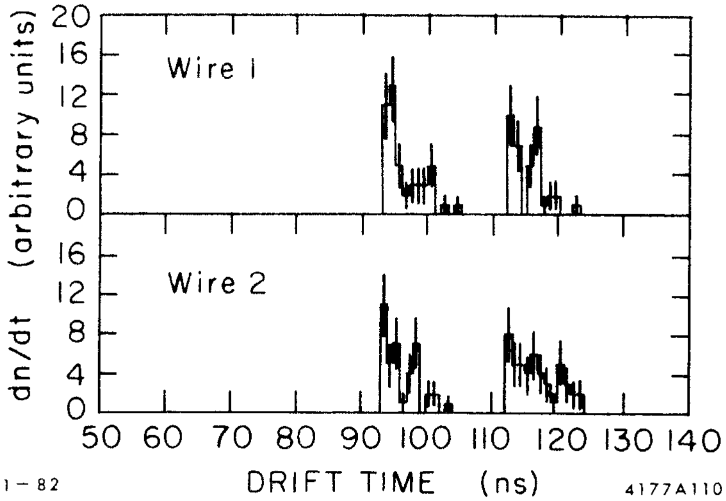

Fig. 10. Arrival times of electrons in a mini-jet chamber from two closely-spaced tracks.

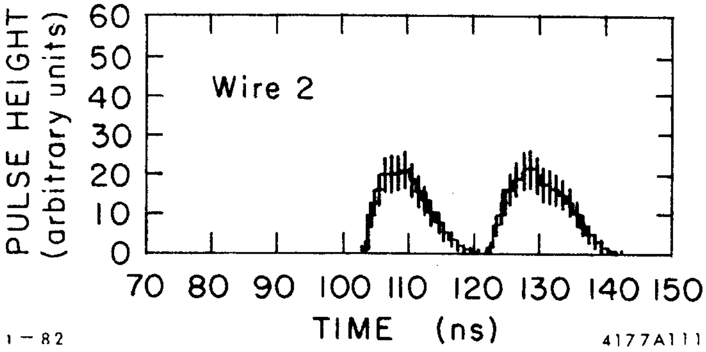

Fig. 11. Drift chamber pulse after amplification and shaping. Note suppression of the 1/t tail.

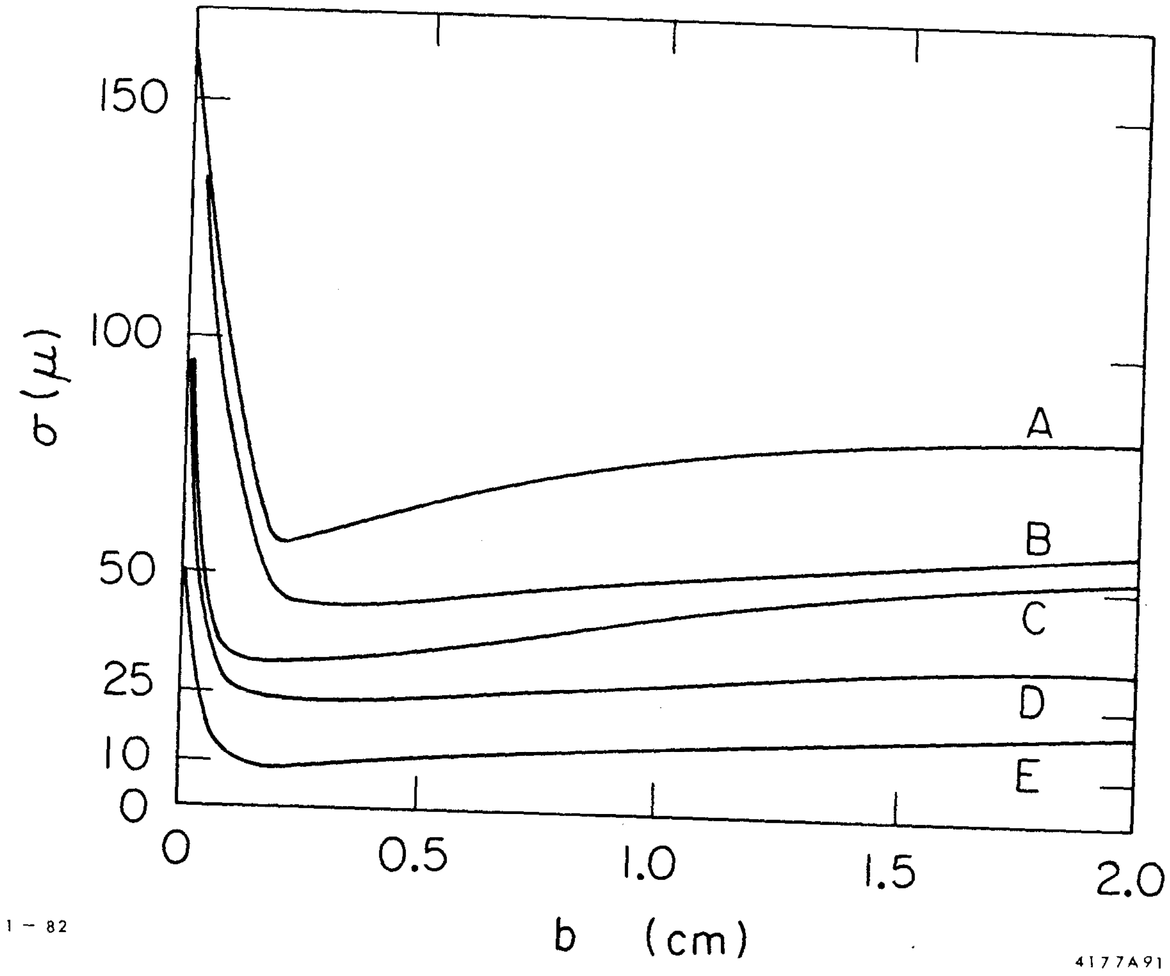

Fig. 12. Model calculations of resolution vs drift length in: (A) 1 atm argon/ethane (50/50); (B) 1 atm ethane; (C) 2 atm argon/ethane (50/50); (D) 2 atm ethane; (E) 3 atm isobutane.

pressures, and drift lengths. The calculations include electronic effects and describe the behavior observed in the Mark II vertex detector quantitatively. They indicate that 10 μ resolution is possible with conventional amplifiers by using isobutane at 3 atmospheres pressure. Slower gases, gases with lower diffusion, more intelligent timing strategies, or a good new twist may also help.

The extrapolated track resolution in such a chamber is

$$\sigma_x = \sqrt{\left(\frac{7.1}{p}\right)^2 + (1.2\sigma)^2} \qquad (\sigma \text{ in microns})$$

where p is in GeV/c and σ is the spatial resolution per measurement. Thus resolution in the 15 to 25 μ range looks feasible. The very low mass of the device is a plus, both because the multiple scattering is very low and because there is little material for photon conversions. The major uncertainty is whether very good pulse-pair resolution can be obtained without compromising spatial resolution.

VI. Conclusions

Detectors capable of measuring the vertex topology of high energy e^+e^- interactions to the 10 μ level can do interesting and exciting physics. They should be able to tag flavor directly, measure particle lifetimes, and aid in new particle searches. Detectors need 10 - 20 μ spatial resolution and 100 μ track-pair resolution to do the job; despite these severe requirements, several techniques look promising.

Future work is needed in several areas. Monte Carlo studies should proceed with realistic vertexing algorithms and should evaluate tagging efficiencies and physics backgrounds in general hadronic events. Careful thought must be given as to how to integrate a vertex detector to the beam pipe and to beam pipe design. Studies of beam-related electrical noise[19] indicate that the direction penetration of the fields from the beam have not been the cause of the pickup problems at SPEAR and PEP. How can sensitive electronics be shielded from beam pickup? Beam related backgrounds must be considered. How will they affect the lifetime and performance of various detectors? Last and most important, detectors of high spatial and track-pair resolution must be developed.

References

1. John Layter, SLC Workshop Note #61.
2. Y. S. Tsai, Phys. Rev. D4, 2821 (1971).
3. M. Kobayashi and T. Maskawa, Prog. Theor. Phys., 49 (1973), 652.
4. H. Harari, SLAC-PUB-2234 (1978); B. Gaisser, et al., SLAC-PUB-2523 (1980).
5. C. Llewelyn-Smith, LEP Summer Study.
6. S. Dimopoulos, et al., University of Michigan preprint UMHE80-22 (1980).
7. Blair Ratcliff, SLC Workshop Note #59.
8. Blair Ratcliff, SLC Workshop Note #59.
9. Neville Reay, SLC Workshop Note #54.
10. E. Heijne, private communication to N. Reay.
11. B. Hyams, private communication to N. Reay.
12. A. Bross, SLC Workshop Note #62.
13. C.J.S.Demerell, et al., Rutherford Lab preprint RL-80-082, (1980)
14. R. C. Field, SLC Workshop Note #50.
15. J. Va'Vra, SLC Workshop Note #60.
16. R. A. Boie, et al., IEEE Trans. on Nucl. Sci. NS-28, 603 (1981).
17. W. Farr, et al., Nucl. Instr. and Meth. 154, 175 (1978); T.W.L.Sanford, "Performance of a High-Precision-Mini-Drift Chamber During a High Intensity Test Run," International Conference on Miniaturization of High Energy Physics Detectors, Pisa, September, 1980; B. Dainese, et al., "Development of a Flat Wire Chamber with Very High Position Accuracy," INFN/TC-80/13, October, 1980.
18. J. A. Jaros, SLC Workshop Note #51.
19. S. Parker, SLC Workshop Note #63.

CALORIMETRY

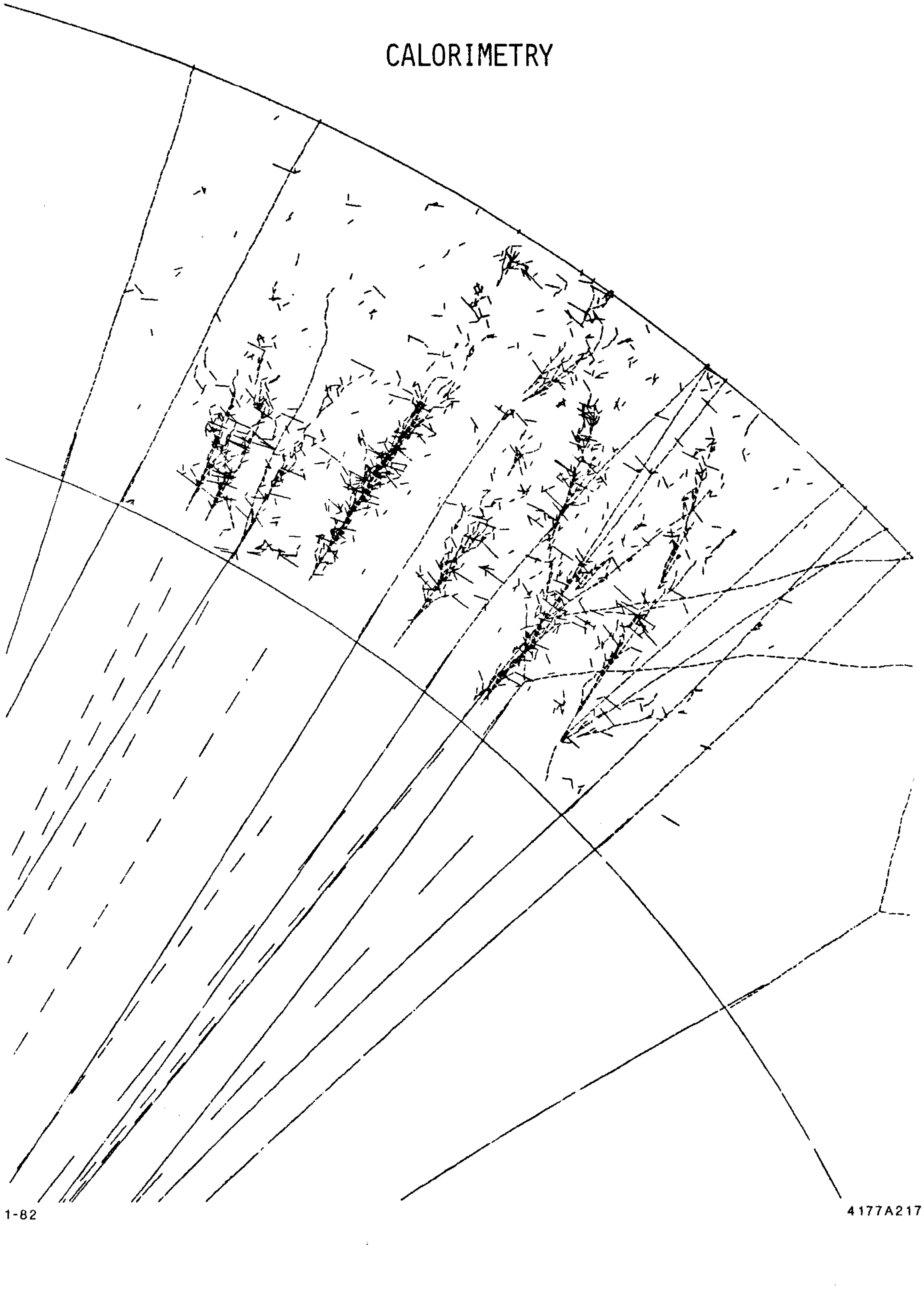

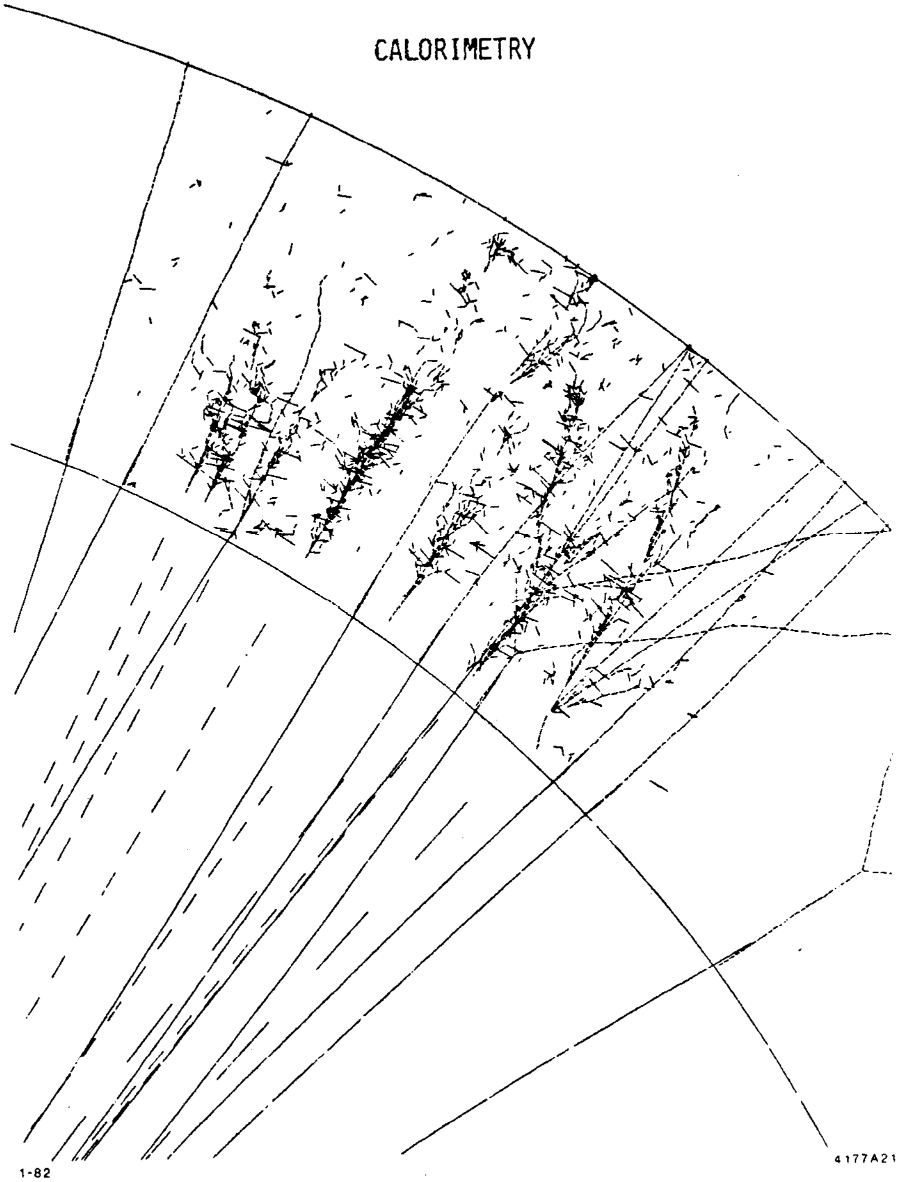
CALORIMETRY
1-82
4177A217

I. INTRODUCTION

We have divided this study of calorimetry at the SLC into five topics:

- physics with calorimeters,
- readout geometries,
- performance of existing detectors,
- calorimeter technologies, and
- new calorimeter designs.

The first topic is a review of the Z^0 physics in which calorimetry would be important. We discuss the Monte Carlo model and the general features of the events which it generates. We consider how the physics affects the design of the electromagnetic and hadron calorimeters in energy resolution, segmentation, solid angle coverage, and general performance. Several inverse questions, such as how the physics is compromised if only the endcaps are outfitted with hadron calorimeters, are also considered.

The two ways of reading out a calorimeter, strips and towers, are the basis of the second topic. Strips provide signals in orthogonal coordinates which are highly segmented, but with ambiguities for multiple hits. Towers are independent blocks and hence have no multi-hit ambiguity; such a system is generally less finely segmented, however. We discuss a model which makes quantitative comparisons of these two schemes, with particular reference to electromagnetic calorimeters. These programs should be useful in other studies of calorimeter performance as well.

There are six detectors at PEP and SPEAR with calorimetric elements. The third topic is a review of their performance at present energies and an evaluation of the problems which would arise at SLC energies. These existing detectors provide both lessons in design and realistic numbers for practical performance.

The new technologies which may be mature enough for use in an SLC detector are considered as the fourth topic. Some are now being built into $\bar{p}p$ detectors, others are in test beam stages, and others are still bright ideas. We review ten techniques and include references for further pursuit. We look in more detail at the question of compensation in hadron calorimeters as a method which promises significant improvement in energy resolution.

The last section combines the physics goals, readout schemes, and present and future techniques into sensible calorimeter designs which sharpen the issues. Six models resulted. We discuss their strengths, weaknesses, feasibility, and rough costs.

II. STUDY OF Z^0 DECAYS WITH CALORIMETERS

Assuming standard weak couplings, the Z^0 will decay predominantly to fermion-antifermion pairs,

$Z^0 \longrightarrow$ quark pair 73% (1)

$Z^0 \longrightarrow e^+e^-, \mu^+\mu^-, \tau^+\tau^-$ 9% (2)

$Z^0 \longrightarrow \nu_i\bar{\nu}_i$, $i=e,\mu,\tau$ 18% (3).

The most interesting decay modes containing Higgs particles and other exotics are expected at rates of order 0.1% or less. At an average luminosity of several times 10^{30} cm^{-2} sec^{-1}, data could be recorded at rates of more than 10^5 events per month and searches for Higgs particles and deviations from the standard theory become feasible.

While the leptonic and most exotic processes are clearly marked by a few very high momentum leptons, the typical hadronic event consists of two or more jets--each containing roughly 10 charged light mesons and 10 photons--in a cone of less than 10° half-opening angle. Higher order processes, such as hard gluon emission and the production of heavy quarks, will result in wider jets, or more than two jets.

In the past, general-purpose solenoidal detectors have been the most favored--providing precise charged particle tracking for magnetic analysis, electromagnetic calorimetry for photon energy measurement and electron identification, and sometimes including hadron calorimetry and particle identification. A comprehensive detector that might be able to address all the physics questions at the SLC--including the unexpected--has been under study by various groups. In addition, a non-magnetic detector using calorimetry has been suggested. A compromise between the very large general purpose device and the pure calorimetric detector may also be of interest, especially considering reduced costs and the possibility of using existing devices.

In this first part of the calorimetry report we study various physics questions than can be addressed with the help of calorimetric measurements. We review specific exclusive states, inclusive spectra and the general characteristics of hadronic events and study how they influence the design of the detector, in particular the shower detectors. While specific designs incorporating various techniques of shower detection and readout will be presented in the later sections of the report, we shall assume for this introduction that the calorimeter will be external to a cylindrical tracking device of roughly 3-m diameter and at least 4-m length.

A. Z^0 Physics with Calorimeters

The following sections specify the physics topics of interest at Z^0 energies and emphasize the areas where calorimetry would be of prime use.

1. Hadron production at Z^0 energies

Hadronic final states are expected to comprise some 70% of the total Z^0 decay rate; a detailed study of these events should provide answers to basic questions on the nature of the weak coupling to quarks of different flavor. Furthermore, even though QCD is widely accepted as the correct theory of strong interactions, experimental tests at energies beyond PEP and PETRA will still be of interest at SLC and LEP. In searches for rare processes a detailed understanding of the dominant hadronic final states will be required.

a) Monte Carlo Simulation of Hadronic Events

Hadronic decays of the Z^0 have been simulated by an existing Monte

Carlo program[1] which was modified to take into account the relevant couplings of the Z^0 to quarks. The data are generated at a fixed center-of-mass energy of 88.6 GeV, thus neglecting the width of the Z^0 and any initial state radiation. Six flavors are produced and the mass of the t-quark is set to 19 GeV/c^2. The hadronization proceeds a la Feynman-Field, with a flat fragmentation function for b- and t-quarks. No baryons are produced. All unstable particles decay and interactions in the beam pipe and other material have been suppressed.

Charged particles are tracked in a solenoidal magnetic field of 5 kilogauss parallel to the beam. For a cylindrical drift chamber with 20 layers and a spatial resolution of 0.15 mm in the drift direction and 3 mm in the direction parallel to the beam, we can expect at best a momentum resolution of $dp_t/p_t=0.0025p_t$ (p_t in GeV). The corresponding angular resolution is 0.2 mrad in ϕ and 1.1 mrad in θ. The momentum error increases for tracks that are emitted at small angles to the beam and exit the chamber through the ends. A track is required to traverse at least a third of the radial length in the chamber to allow for track finding. Losses in precision and reconstruction efficiency due to neighboring tracks in the same cell or crossing are not taken into account. Here the tracking device is just used for comparison with a calorimetric measurement of hadronic energy. Multiple scattering effects are dependent on details of the set-up and have been ignored.

The calorimeter is assumed to cover the cylindrical surface of the tracking device as well as the endcaps down to distances of 0.2 m from the beam line. We have considered electromagnetic shower detectors with energy resolutions of $10\%/\sqrt{E}$ and $20\%/\sqrt{E}$ and angular resolutions between 5 mrad and 20 mrad. For a hadron calorimeter we have taken an optimistic guess of $35\%/\sqrt{E}$ and a more conventional estimate of $70\%/\sqrt{E}$, with the same angular resolution as the electromagnetic calorimeter.

Gaussian error functions have been imposed on the produced particle momenta and angles to simulate measurement errors. No attempt has been made to simulate pattern recognition and track reconstruction, since these problems depend on a specific layout which is not specified at this time. Consequently, the quoted resolutions are to be taken as a guideline and can be used only for relative comparisons. The actual measurements are expected to be degraded in comparison to measurements achieved for isolated particles.

b) General Characteristics of Hadronic Events

In Table Ia we present the particle multiplicities and momenta obtained as an average over all Monte Carlo simulated events. The predicted charged particle multiplicity is 21, the average number of photons per event is 22. Most photons are from π^0 decay. The electron data include Dalitz pairs, but not conversions in the beam pipe or any other material. If we assume a minimum of 2.5% of a radiation length, we expect on the average one additional electron per event. The muon rates include π and K decays, roughly 1 μ/event; 0.2 muons and 0.2 electrons per event are due to c-, b-, or t-decay. In Table Ib the same average quantities are presented for hadronic events with t-flavor only. We observe substantially higher multiplicities, and increased lepton momenta .

The momentum spectrum of all charged particles peaks around 500 MeV/c, half the pions have momenta below 1 GeV/c, half of the photon spectrum is below 0.3 GeV.

TABLE I

Average particle momenta and multiplicities for hadronic events
a) all hadronic events (udscbt quarks)

	⟨p⟩ (GeV/c)	P(median) (GeV/c)	⟨n⟩
photons	1.14	0.30	21.8
electrons	1.72	0.40	0.4
muons	0.90	0.35	1.2
pions (±)	2.45	1.03	16.4
kaons (±)	4.19	2.00	2.9

b) hadronic events from t-quarks only

	⟨p⟩ (GeV/c)	P(median) (GeV/c)	⟨n⟩
photons	0.68	0.32	32.6
electrons	2.30	0.95	1.0
muons	1.20	0.41	2.5
pions (±)	1.42	0.77	26.0
kaons (±)	2.20	1.36	4.2

c) Total energy measurement

A comparison of the electromagnetic and the hadronic energy component in the hadronic final states is given in Figure 1. On the average 29% of the total energy is carried by electrons and photons, while pions and kaons have 67%, and muons have 1.2%. Neutrinos carry less than 2% of the total energy. The integral over the total energy is presented in Figure 2a for detectors covering a limited range in polar angle, as compared to an ideal detector that has full coverage and allows only neutrinos to escape. Figure 2b illustrates the effect of limited detector resolution on the total energy measurement. The effect of the solid angle coverage is dominant, and the additional improvement obtained from hadron calorimetry is not very large--in particular considering the crude simulation of the detector errors in this analysis. However, a possible copious production of baryons with 50% neutrons, would improve this

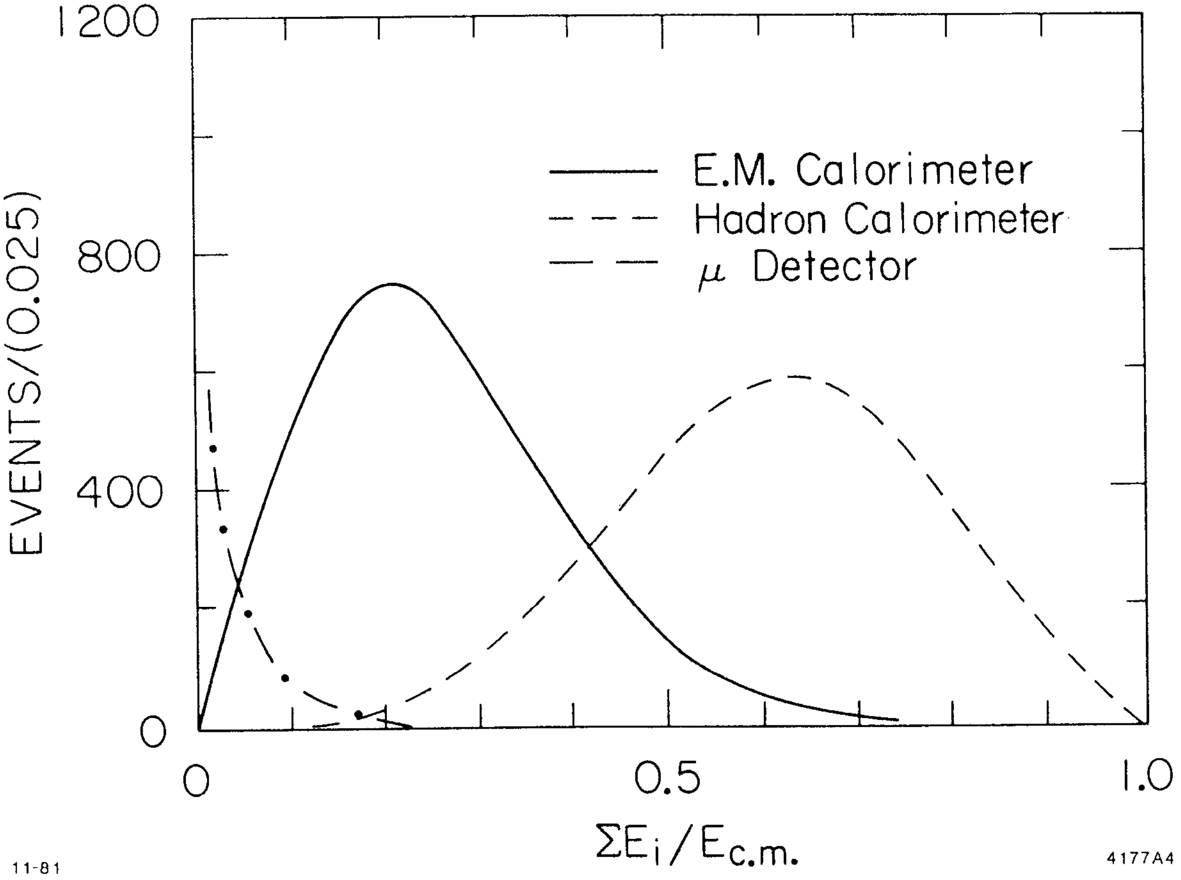

FIG. 1. Distribution of the energy deposited in various detector components. The curves are normalized to a total of 10,000 hadronic Z^0 decays.

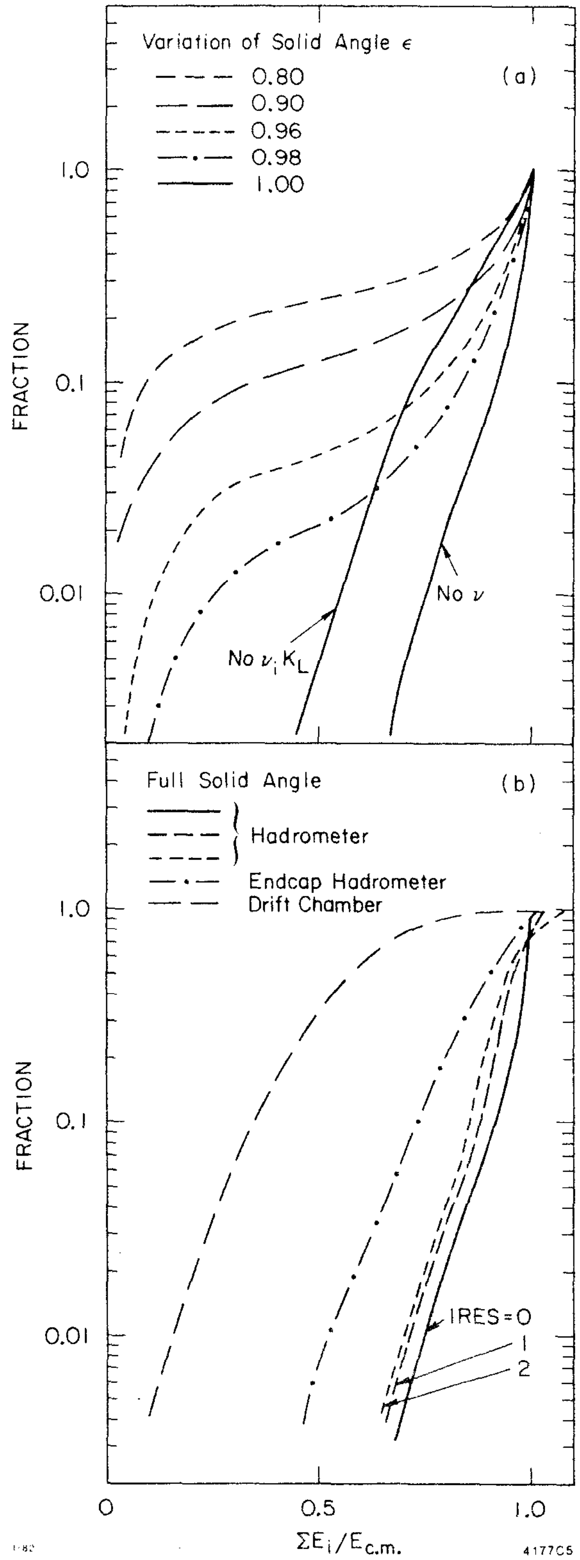

FIG. 2. Integral energy spectrum measured a) for detectors of different coverage in the polar angle but with perfect resolution, and b) for detectors of different resolution and various detector layouts. The three curves for a full-solid-angle hadrometer correspond to resolutions of 0.0, 0.1 and $0.2/\sqrt{E}$.

comparison in favor of hadron calorimetry.

d) Particle Density

A typical hadronic event consists of two or more jets, each containing an average of 10 charged particles and an equal number of photons in a cone of less than 10° half-opening angle. Higher order processes like hard gluon emission as well as the decay of heavy mesons will result in wider jets or more than two jets. In Figure 3 the charged particle density is presented as a function of the angle with respect to the jet axis, separately for events produced via the light quarks u,d,s,c and for the t-quark. The photon density distributions are very similar. While jets produced by light quarks contain half the multiplicity (4.5 charged particles per jet), in a cone of half-opening angle 23°, half the jet energy is contained in a cone of only 4°. For t-quark events with an average multiplicity of 17 charged particles per jet the corresponding angles are 39° for the multiplicity and 22° for the energy containment. In the center of the jet the particle density for light quark jets is four times larger than for t-quark. In the absence of a magnetic field a detector element of roughly 6 x 6 cm^2 placed on the jet axis at a distance of 1.5 m from the beam will be struck by two or more charged particle in 10% of all events. Roughly the same number of photons will hit the device. A magnetic field will reduce the density of the cluster on the outside of the tracking chamber; high momentum particles, however, will not be separated by very much.

e) Inclusive Lepton Distributions

Distributions for the normalized momentum, $x=2p/E_{cm}$, and for $p^2{}_t$ (the square of the momentum transverse to the direction of the fastest initial quark) are presented in Figure 4 for muons produced in events

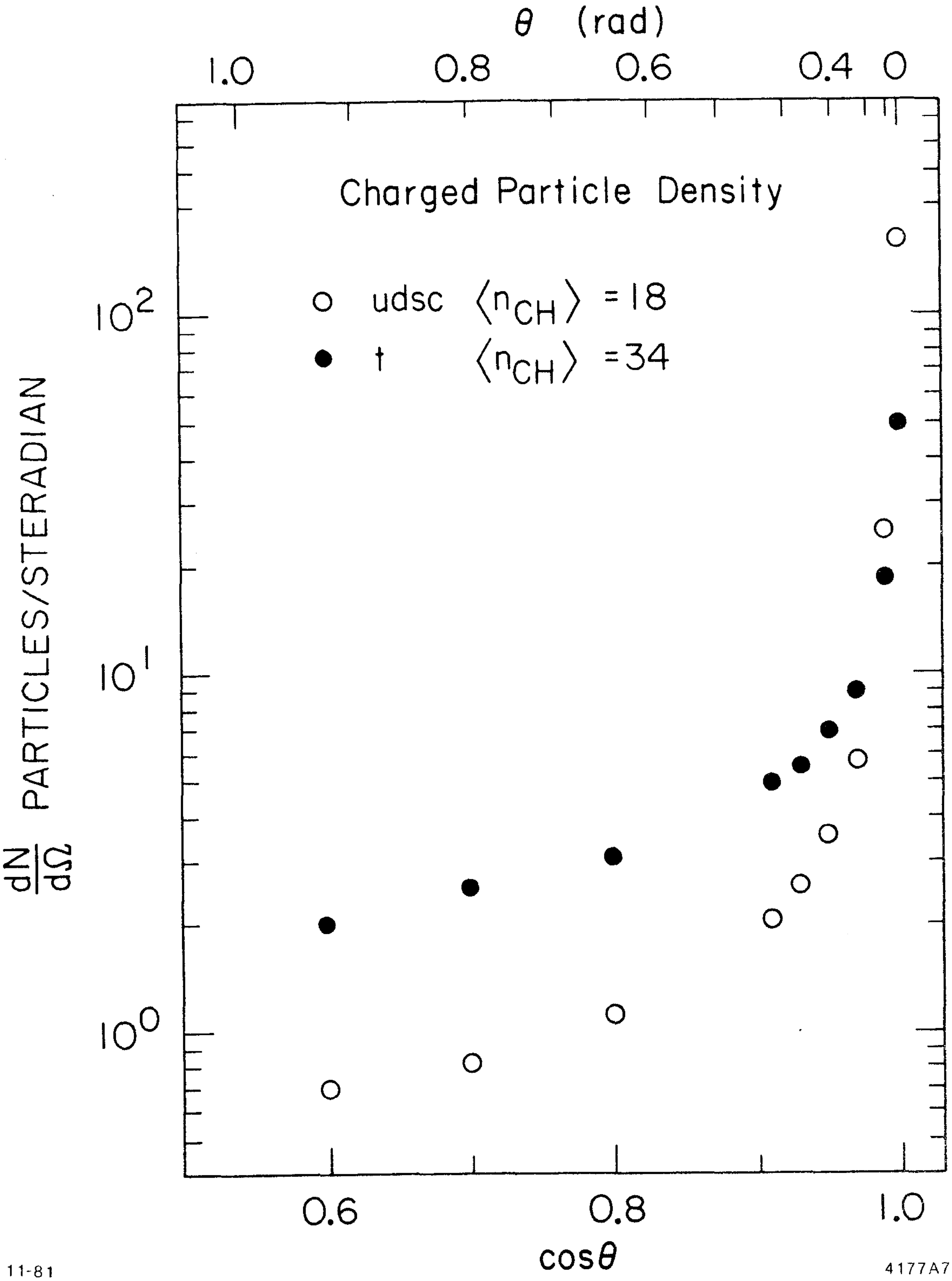

11-81

4177A7

FIG. 3. Charged particle density as a function of the angle relative to the direction of the primordial quark, separately for the light quarks and the t-quark.

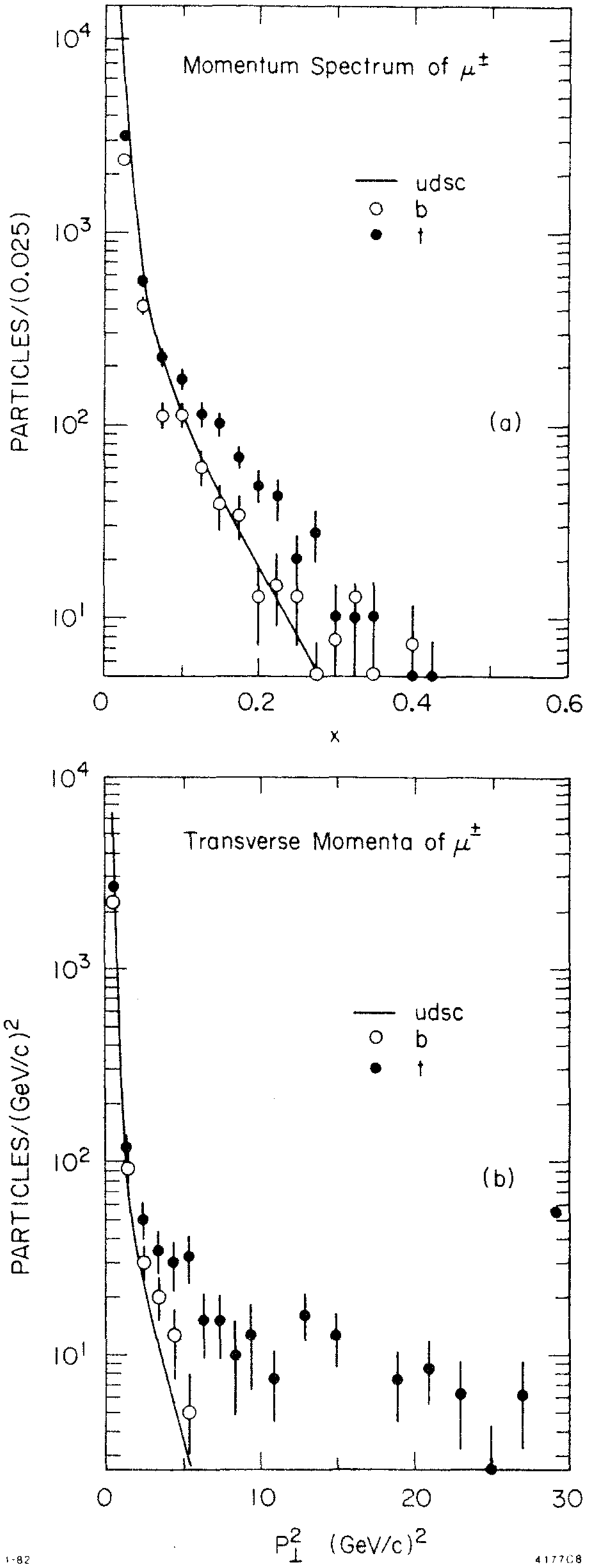

FIG. 4. Momentum distributions of muons for events of different quark flavor, a) total momentum normalized to the beam energy, and b) momentum transverse to the direction of the primordial quark direction. Muons from pion and kaon decay are included. The distributions are normalized to 10,000 hadronic events.

with primordial u,d,s,c,b and t-quark pairs. While the hadron and photon spectra show very little flavor dependence, prompt leptons from t-decay have substantially higher transverse momenta. Consequently, prompt leptons are not buried in the core of the jet under huge backgrounds from conversions and pion and kaon decay. Figure 5 underlines this fact by showing the ratio of muons to all charged particles as a function of the angle relative to the jet axis. While the ratio of leptons to hadrons is 0.08 and roughly independent of x and p_t, it decreases by an order of magnitude in the core of the jet. Given a charged particle density of less than 2 particles/steradian at angles larger than 20°, the problem of lepton identification becomes much less difficult. Inclusive leptons at high p_t may actually serve as a tag for a t-flavored jet, and detectors with lepton-hadron separation at the level of 1:100 should be adequate. Figure 6 gives the tagging efficiency and the expected signal to noise ratio for muons. Here muons from u,d,s,c, and b-jets are considered as background, while all muons from t-events are taken as signal. Background due to punch-through of hadrons is not taken into account, since it depends on the specific design of the detector. The Monte Carlo calculation assumes leptonic branching ratios of 10% for t, b, and c-quarks. Similar results hold for electrons, and thus t-quark-pair events can be tagged by charged leptons with p_t above 2 GeV with an an efficiency of about 50%.

f) Jet Measurements

In an attempt to understand the importance of various detector properties for the reconstruction of jets, we have studied the errors on the measured jet axis and jet energy for 2-jet events simulated by the Monte Carlo. In Figure 7 the measured jet axis as derived from the

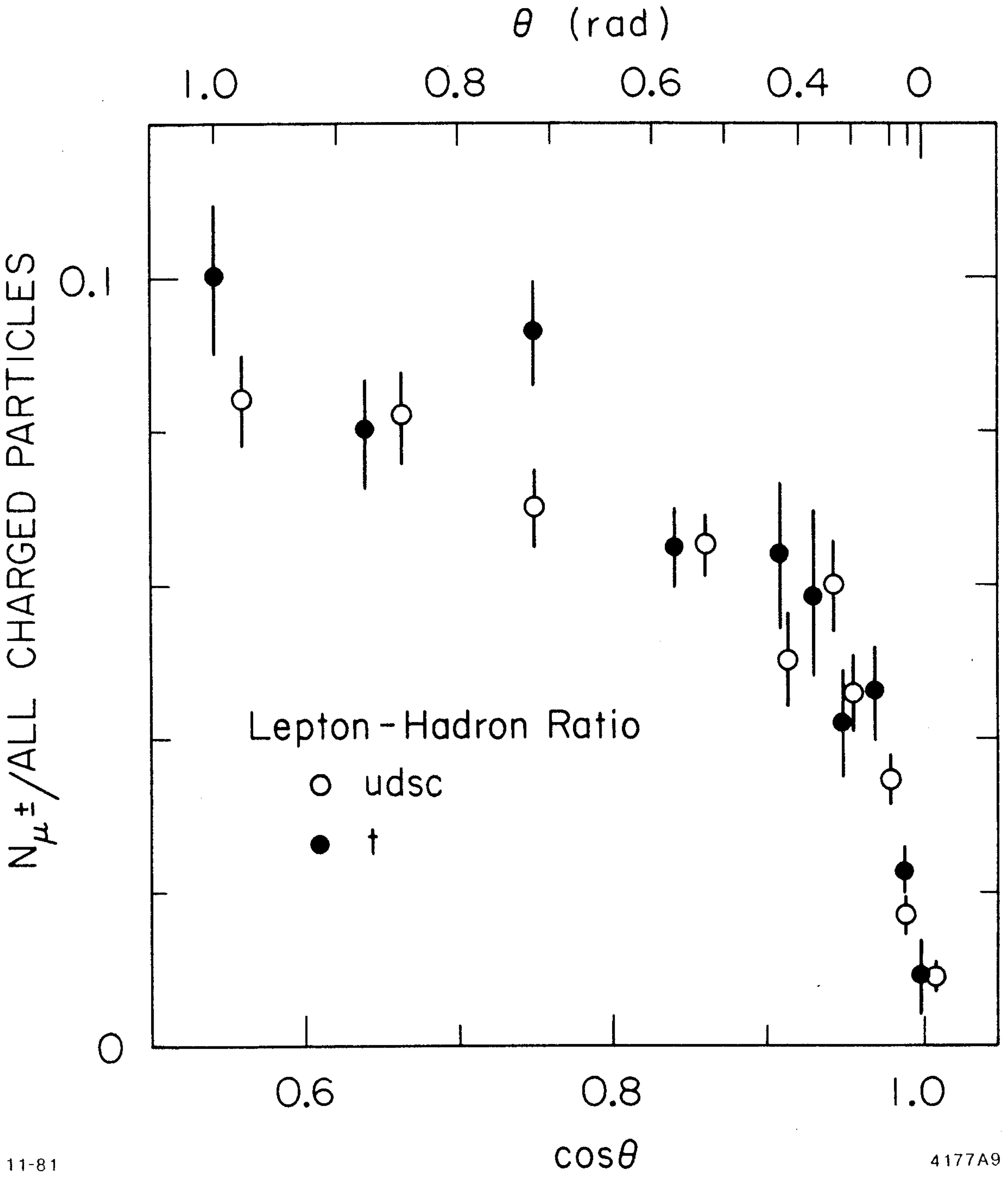

FIG. 5. Ratio of muons to all charged particles produced versus the angle relative to the primordial quark direction.

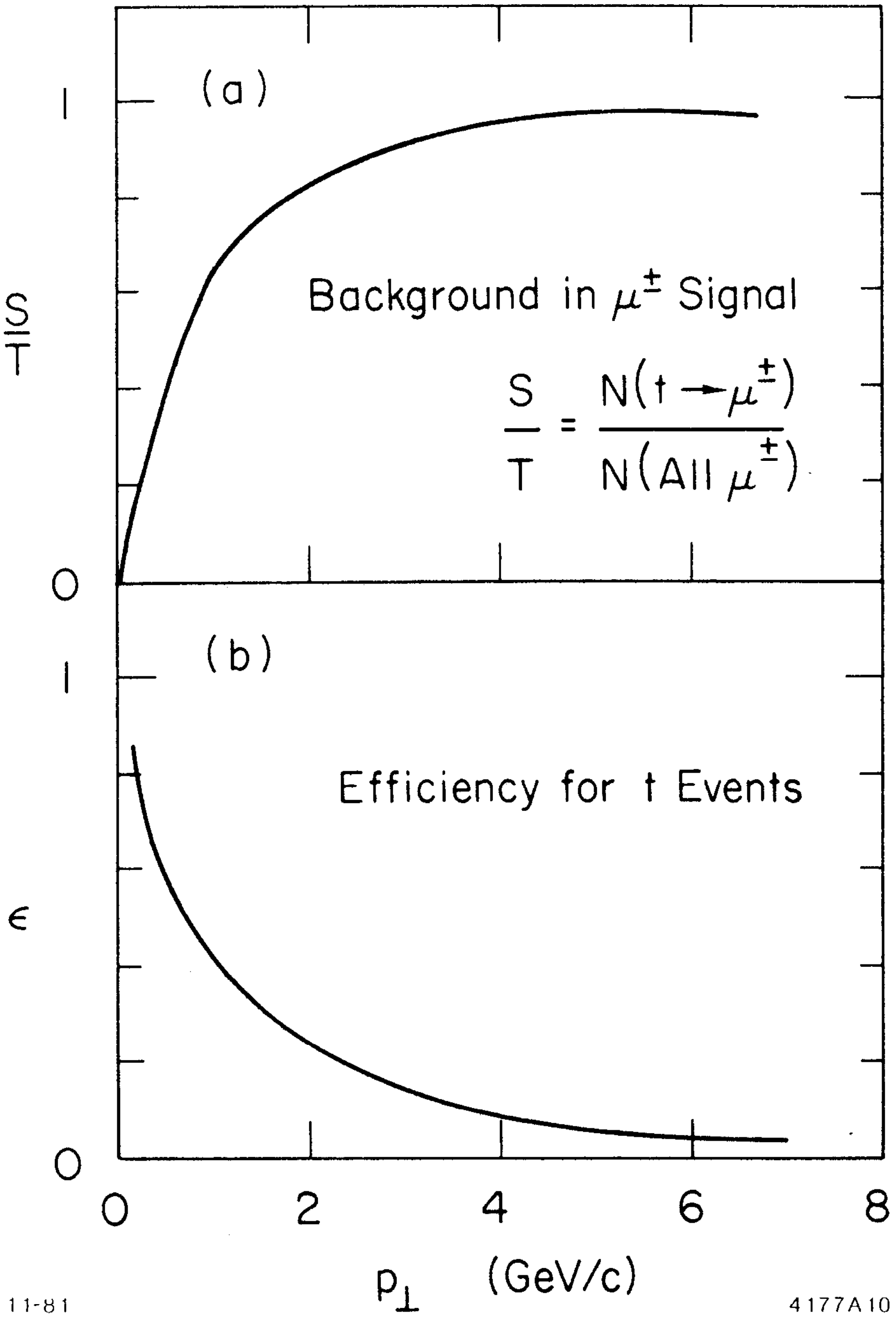

FIG. 6. Detection of t-flavored events via high $p_\perp$ muons.

a) Signal to noise ratio versus the transverse momentum of the muon. As signal we count all muons from t-events, including those from pion and kaon decay.

b) Fraction for t-events with a muon above the transverse momentum p_t. This curve rises to 2.5 for $p_t = 0$.

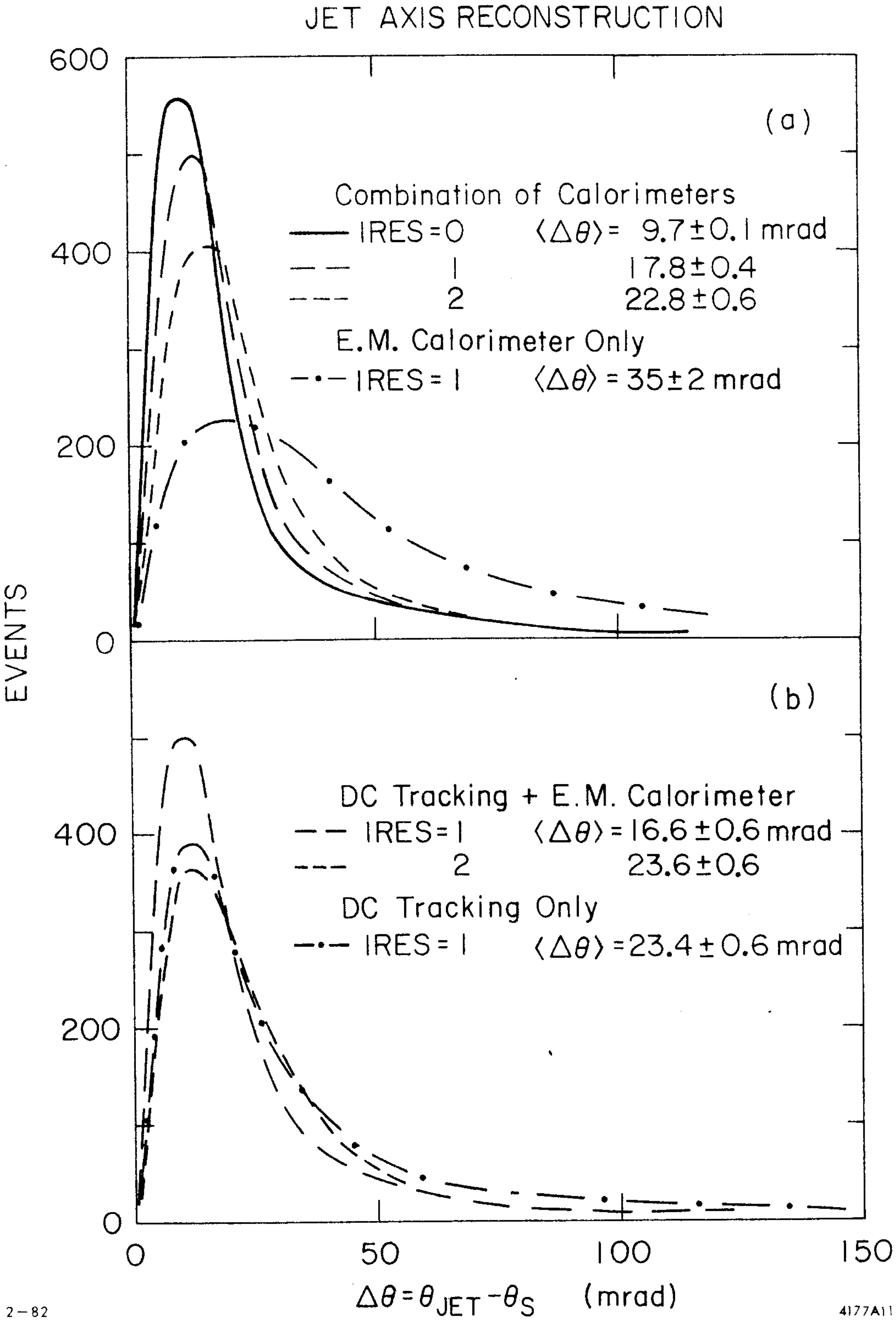

FIG. 7. Reconstruction of the jet axis using the simple sphericity method, for various detectors of different layout and resolution. The angle plotted is the difference between the axis given by the direction of the primordial quark pair and the axis reconstructed from the measured particles.

sphericity tensor of the detected particles is compared to the direction of the primordial quark pair. The measurement has an intrinsic error of 10 mrad caused by the production of neutrinos and details in the hadronization process. A measurement based on an electromagnetic calorimeter, without a tracking chamber inside, gives a rather poor jet axis reconstruction (±35 mrad) due to large event-by-event fluctuations in the neutral to charged energy distribution. A calorimeter for electromagnetic and hadronic showers is roughly equivalent to a drift chamber and electromagnetic shower detector combination. In general, good solid angle coverage and good angular resolution are most crucial to the jet reconstruction.

The jet axis reconstruction combined with a measurement of the total missing momentum can be used as a tag for leptonic decays of heavy particles. Figures 8 and 9 show the square of the missing momentum transverse to the reconstructed sphericity axis, for a variety of detector options. The t-events exhibit a rather flat distribution compared to the lighter quarks, including the b-quark. Even for rather poor calorimetric resolution, a separation of t-jets seems feasible with excellent signal to noise ratio and good efficiency. Hadron detection by drift chamber tracking alone gives somewhat poorer results, but combined with an electromagnetic shower counter of good resolution ($10\%/\sqrt{E}$ and 10 mrad) could be adequate for this kind of flavor tagging. Figure 10 gives the efficiency and the signal/total ratio for t-jets selected by a cut on the missing transverse momentum. In practice, the energy deposition of hadronic particles in the electromagnetic calorimeter constitutes a subtle problem for the experimenter.

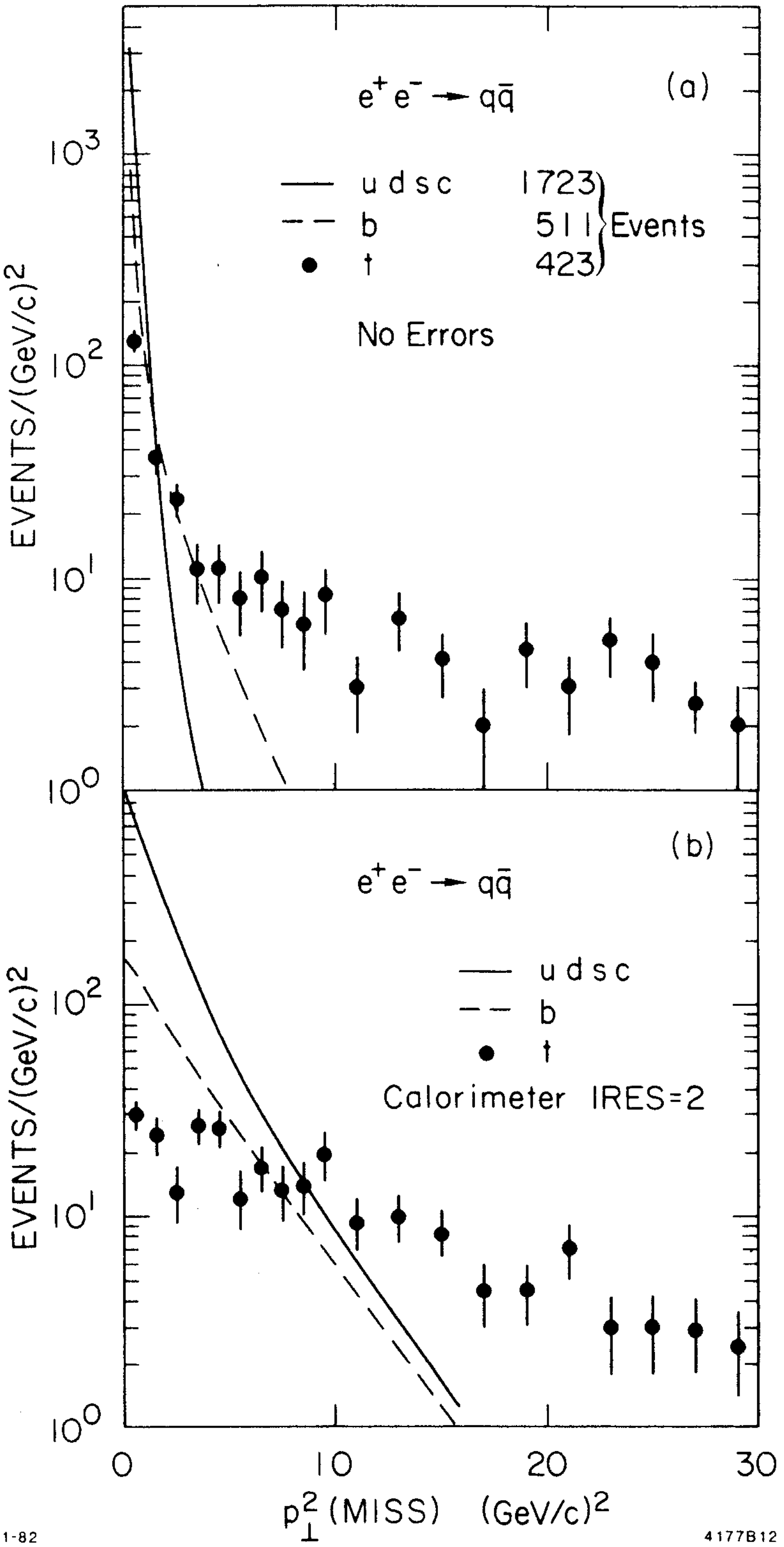

FIG. 8. The square of the component of the missing momentum transverse to the jet axis as measured by the sphericity axis for events of different flavor, a) in a perfect detector with no errors or inefficiencies, b) in a calorimetric detector of 96% solid angle, 20 mrad angular and 20%/$\sqrt{E}$ energy resolution for photons, and 70%/$\sqrt{E}$ for hadrons.

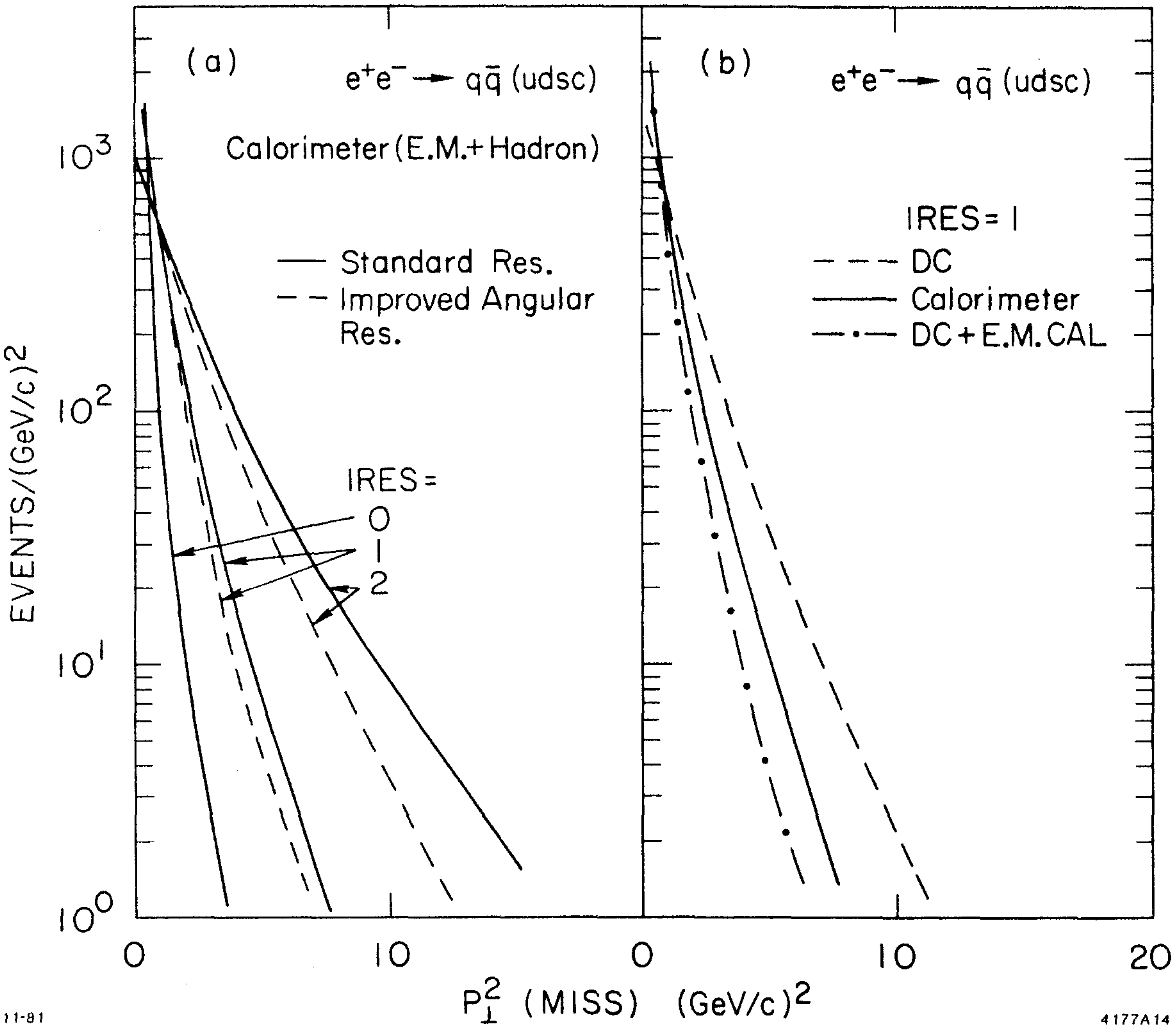

FIG. 9. The square of the missing momentum transverse to the jet axis for various detector choices. The different resolutions are specified by the parameter IRES.

IRES=0	Perfect detector		
IRES=1	Solid angle 96%		
	Drift chamber	$dp/p=0.0025p$	
	E.M. Calorimeter	$dE/E=0.10/\sqrt{E}$	$d\theta=10$ mrad
	Hadrometer	$dE/E=0.35/\sqrt{E}$	$d\theta=10$ mrad
IRES=2	Solid angle 96%		
	Drift chamber	$dp/p=0.005\ p$	
	E.M. Calorimeter	$dE/E=0.20/\sqrt{E}$	$d\theta=20$ mrad
	Hadrometer	$dE/E=0.70/\sqrt{E}$	$d\theta=20$ mrad

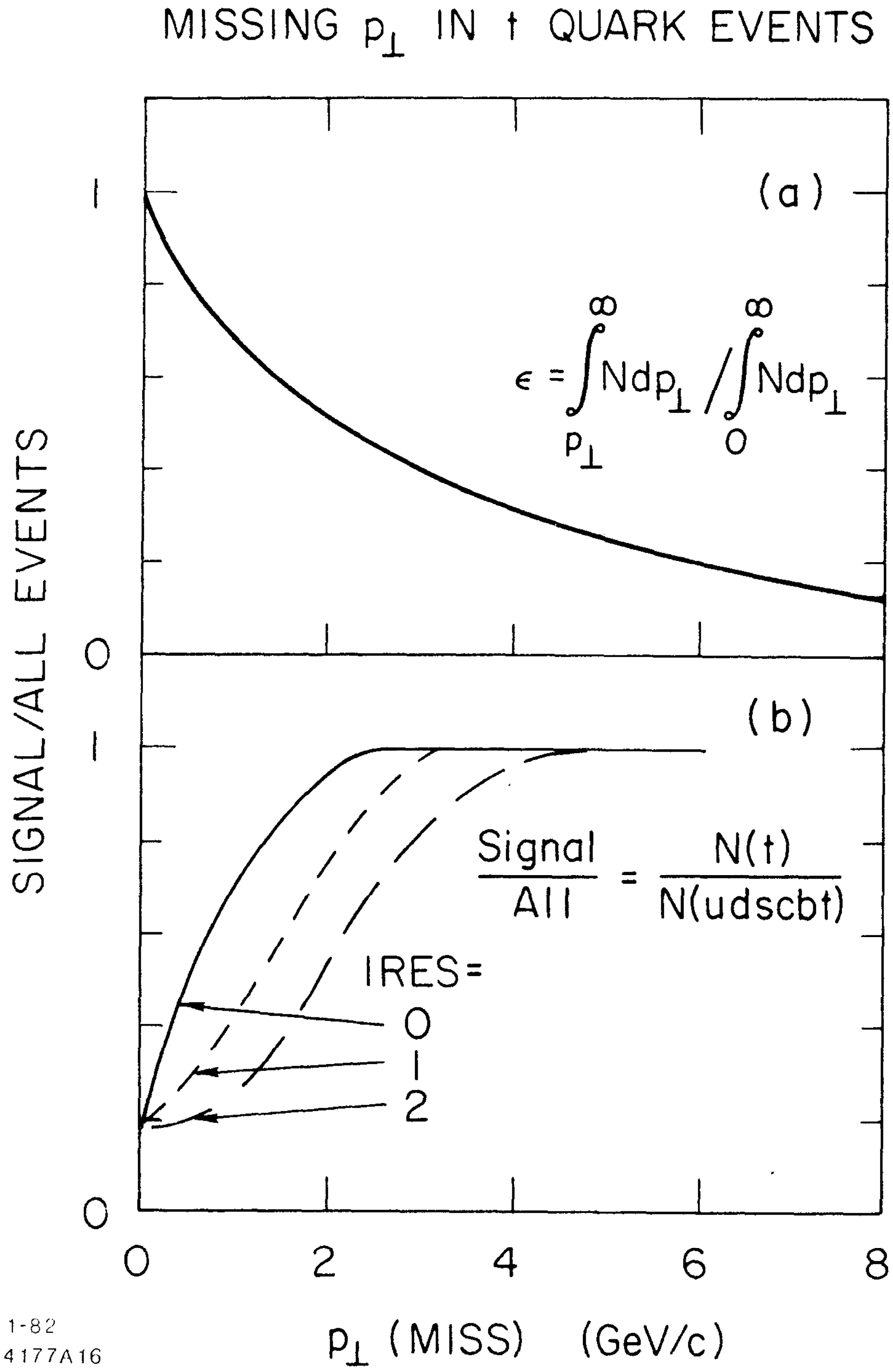

FIG. 10. Detection of t-events by missing momentum transverse to the jet axis.
a) Fraction of all t-events selected by a cut on missing p_t
b) Ratio of t-events to all events with a missing transverse momentum p_t.

2. Lepton Production

a) Lepton pair production

Measurements of lepton pair production and searches for new heavy leptons, charged or neutral, deal with final states of very low multiplicity compared to hadronic production. Good momentum resolution and good lepton-hadron separation at high momenta are required. While this in general is not a severe requirement, the separation of the decay $\tau^+ \to \pi^+ \nu$ from other decays like $\tau^+ \to \rho^+ \nu$ and $\tau^+ \to \mu^+ \nu \bar{\nu}$ is of particular interest because of the analysing power of the two-body decay for the spin orientation of the tau. A Monte Carlo study of these decay modes indicates that a fine grain calorimeter with a segmentation of 7.5 mrad could result in a contamination of less than 10%.

For the measurement of the muon charge asymmetry, good solid angle coverage and uniformity of the absorber will reduce the systematic errors. Contamination from the decay of tau and possibly other leptons needs to be studied.

b) Partial width $Z^0 \to$ neutrinos

Radiative Z^0 production has been suggested[2] as a way of counting the number of neutrinos. The total width of the Z^0 depends roughly linearly on the number of fermions of mass less than $M(Z^0)/2$. The best way to measure the radiative photon from $e^+e^- \to Z^0 + \gamma$ and avoid background from $e^+e^-\gamma$ and $3\text{-}\gamma$ states is to operate the machine well above the Z^0 mass and look for a single hard photon at relatively small angles to the beam. The authors[2] suggest operating 15 GeV above the Z^0 with photon detection down to 6° from the beam axis. If one required that the photon energy resolution be comparable to the expected Z^0 half-width, then the demands on the resolution of the calorimeter would be not too stringent, namely

$$\Gamma /E = 2.6 \times 0.5 /15 = 8.5\% \quad \text{or} \quad \sigma \simeq 15\%/\sqrt{E}.$$

Attention must be paid to solid angle coverage, to small angles, and to a highly efficient veto for photons and electrons from background processes.

In a 30-day run at a luminosity of 5×10^{30} cm^{-2} sec^{-1}, one can expect at best an effect of 5 standard deviations if there were one 'extra' neutrino beyond the present three. This assumes negligible backgrounds and perfect machine performance. It may therefore be necessary to increase the rate by operating closer to the Z^0 mass and by accepting photons at smaller angles, but this is at the expense of more background. The most severe background is expected to be beam-beam bremsstrahlung (10%), followed by 3-photon final states, beam-gas bremsstrahlung, and two-photon interactions.

Figure 11 shows the photon energy distribution for various energies just above the Z^0 mass peak. The detector acceptance is assumed to be limited in polar angle, $20° < \theta < 160°$, though the total veto acceptance is larger. A smaller angular acceptance like $60° < \theta < 120°$ (a loss in solid angle of 50%) causes a rate reduction by a factor of 3, but reduces the background substantially.

Furthermore, it should be pointed out that a measurement of the total width of the Z^0 by this method does not uniquely determine the number of neutrino decay channels. Partial width contributions from additional charged leptons and quark doublets depend on their mass relative to the mass of the Z^0. For instance, an increase of the t-quark mass by 10 GeV/c^2 lowers the widths of the Z^0 by 100 MeV/c^2, i.e. roughly 3%. To obtain the partial width into neutrinos, the decay width into charged

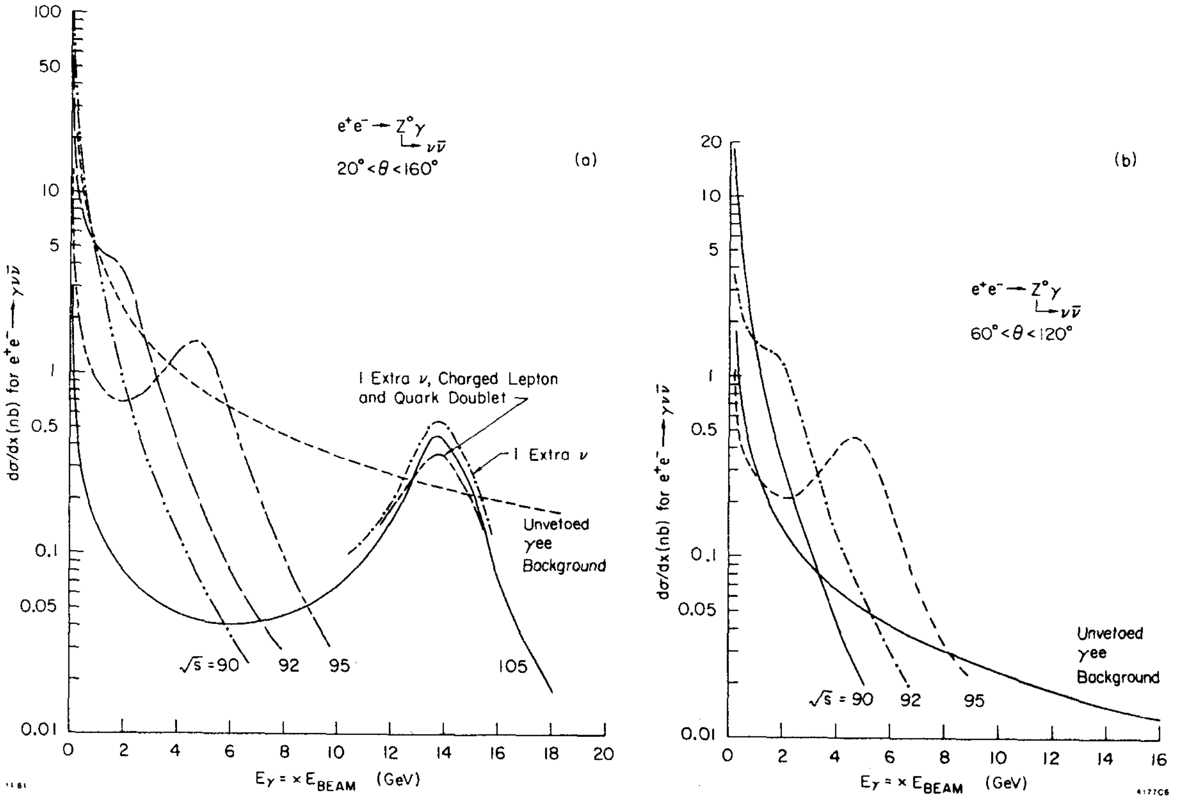

FIG. 11. Differential cross section $d\sigma/dx$ for radiative photons detected at various center-of-mass energies above the mass of the Z^0 (assumed as 90 GeV) for a) $20<\theta<160$ and for b) $60<\theta<120$.

The curves are evaluated for 3 quark flavors, 3 charged leptons and 3 neutrinos. The broken line for the 105 GeV curve indicates the change in the width of the Z^0 if the number of fermion families were 4 instead of 3. Also indicated is the unvetoed background from γe^+e^-.

particles has to be measured and then subtracted from the total width.

3. Rare Processes

Many of the more exotic, non-standard decays are perhaps non-existent or not observable, but some of them are of prime importance. In many of these processes very good energy resolution would enhance the signal-to-noise ratio; good acceptance would enhance the observed rates.

a) Higgs production

In the minimal Weinberg Salam model, there is a single neutral Higgs scalar with known couplings but of unknown mass. The observation of this or any other Higgs boson is probably the most exciting prospect for a machine like the SLC. There are three simple mechanisms for the production of the neutral Higgs

i) $Z^0 \rightarrow H^0 \ \ell^+ \ell^- \quad \ell = e, \mu, \tau$

ii) $Z^0 \rightarrow H^0 \ \gamma$

iii) $Z^0 \rightarrow H^0 \ \nu \bar{\nu}$

The rates for these decays relative to the dimuon rate are presented in Figure 12. The decay rate to Higgs plus neutrinos is a factor two larger for each generation of neutrino. Given an average luminosity of 10^{30} cm^{-2} sec^{-1} and 10^5 Z^0 decays per month, we expect per month 4 events for each mode i), 24 events for the total decay rate iii), and only 0.4 events for mode ii) --assuming a Higgs mass of 20 GeV/c^2. If we double the mass, the leptonic rates i) and iii) go down by a factor 10, and become too small for a meaningful experiment.

Since the Higgs coupling to fermions is proportional to their mass, it would decay dominantly into two jets, either b- or t-quark, depending on its mass. A typical decay of the Z^0 to Higgs would therefore have two hadronic jets, and a pair of leptons or a high energy photon.

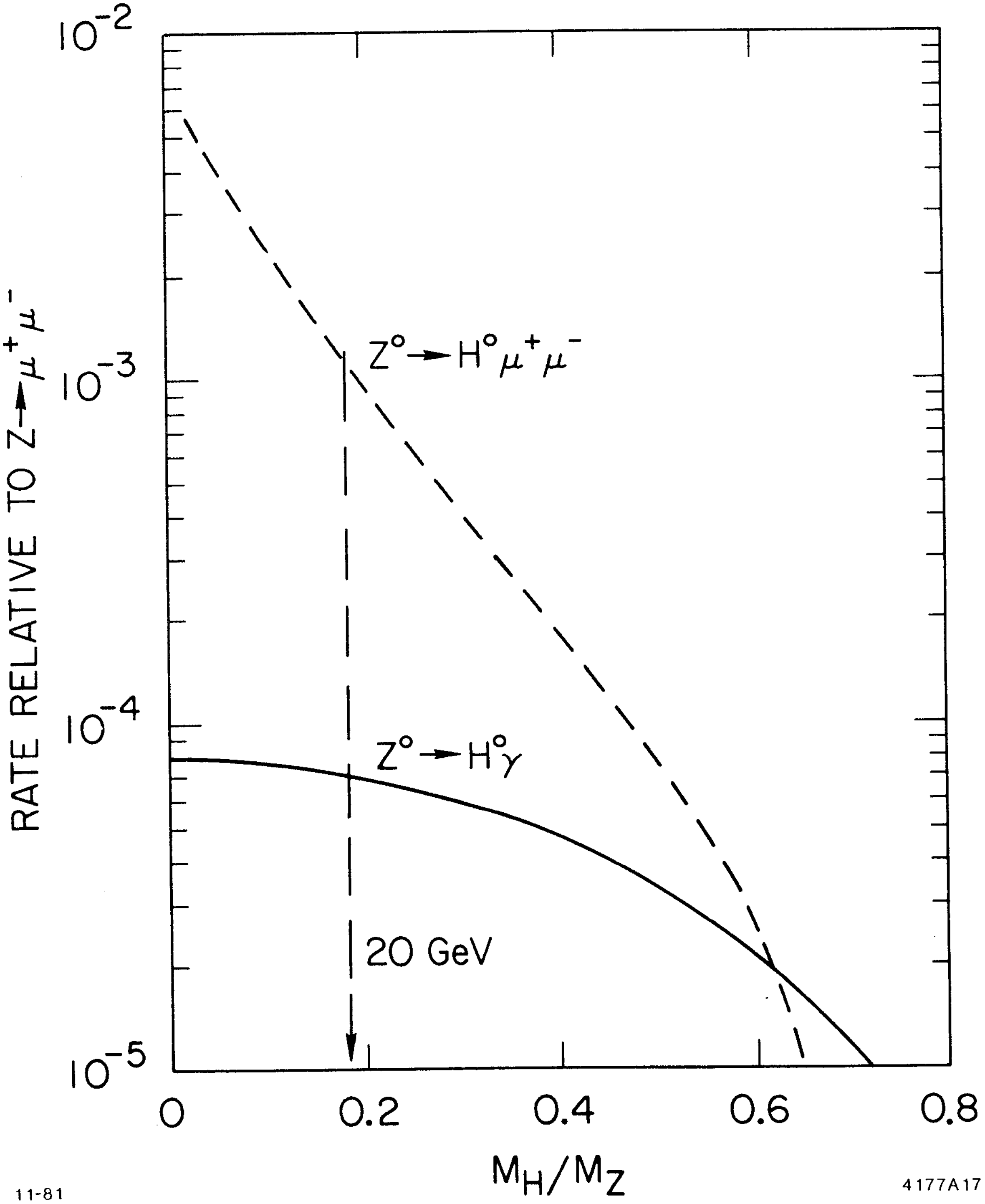

FIG. 12. The relative rates for the production of the neutral Higgs particle in various simple decay modes of the Z^0 as a function of the Higgs mass.

The detection of the three decay modes listed above places somewhat different requirements on the detector and the analysis:

i) $Z^0 \rightarrow H^0 \quad \ell^+ \ell^- \quad \ell = e, \mu, \tau$

The heavy Higgs tends to be at rest in the center-of-mass system so that the invariant mass spectrum of the lepton pair peaks towards the largest mass kinematically possible. The mass of the Higgs is measured as the recoil mass against the lepton pair and the error is dominated by the error on the lepton energy. Consequently, the precision on the electron decay is far superior to the muon or tau decay. We expect that an electromagnetic calorimeter with a resolution of $15\%/\sqrt{E}$ would give a mass resolution between 3% and 10% for masses between 50 and 20 GeV/c^2. This accuracy could be improved over the entire mass range to 1-2% by a special high-precision electromagnetic calorimeter. A 5% result could also be obtained from a measurement of the energies of all particles in jets from Higgs decay, provided not too much energy escaped in the form of neutrinos.

Since the high momentum charged leptons are well separated from the decay products of the Higgs, backgrounds should be low and efficiencies could be as high as 80%. Background in the sample of high energy electrons could come from decays of heavy quarks, two-photon processes and leptonic decays like $Z^0 \rightarrow e^+e^-$ or $\tau^+\tau^-$. The only problematic source of electrons with momenta above 10 GeV/c are decays of t-quarks. Given a production rate of 14% for the process $Z^0 \rightarrow$ t-pairs and a semileptonic branching ratio of 10%, one expects e^+e^- pairs at a rate of $1.4 \; 10^{-3}$ per Z^0 decay. This is about 30 times the expected rate for $Z^0 \rightarrow He^+e^-$, for a Higgs mass of 20 GeV/c^2. A momentum cut of 10 GeV/c on the electrons will only remove 15% of the signal, but reduce the hadronic background by a factor of 20 for a T-meson mass of 19 GeV/c^2 (40 GeV/c^2).[4] In Figure 13 the effective mass of the e^+e^- pair from Higgs production is compared to background from hadronic events. An additional cut on the angle between each lepton and the jet axis of the hadronic particles can reduce the background from t-quark decay by another order of magnitude, provided the T-meson mass does not become too large. This additional cut is particularly effective in reducing background from high momentum hadrons that interact in the shower counter. In summary, Higgs production can give a relatively clean signal, for masses of less than 30 GeV/c^2.

ii) $Z^0 \rightarrow H^0 \gamma$

This mode relies on the detection of a single high energy photon opposite two hadronic jets. The energy of the recoil photon is

$$k = [M_z^2 - M_h^2]/2M_z^2.$$

The uncertainty in E_{cm} of 300-400 MeV is much smaller than the expected half-width of the Z^0 of 1300 MeV. For a narrow Higgs this beam spread introduces an effective uncertainty in the Z^0 mass leading to

$$\sigma_k/k = [\sigma_m(M_z^2 + M_h^2)]/[M_z(m_z^2 - M_h^2)].$$

Figure 14 shows the recoil photon energy and the absolute uncertainty introduced by the beam spread (error bars) as a function of the Higgs mass. The solid line gives the resolution in percent (full width) required of a detector that is well-matched to the spread in beam energy. Except for Higgs masses above 80 GeV, a precision photon detector can help to reduce background for this small signal. The desired resolution of $5\%/\sqrt{E}$ or better would be hard to obtain in a conventional shower chamber, but a NaI or BGO device (see VI E) would be well matched to this.

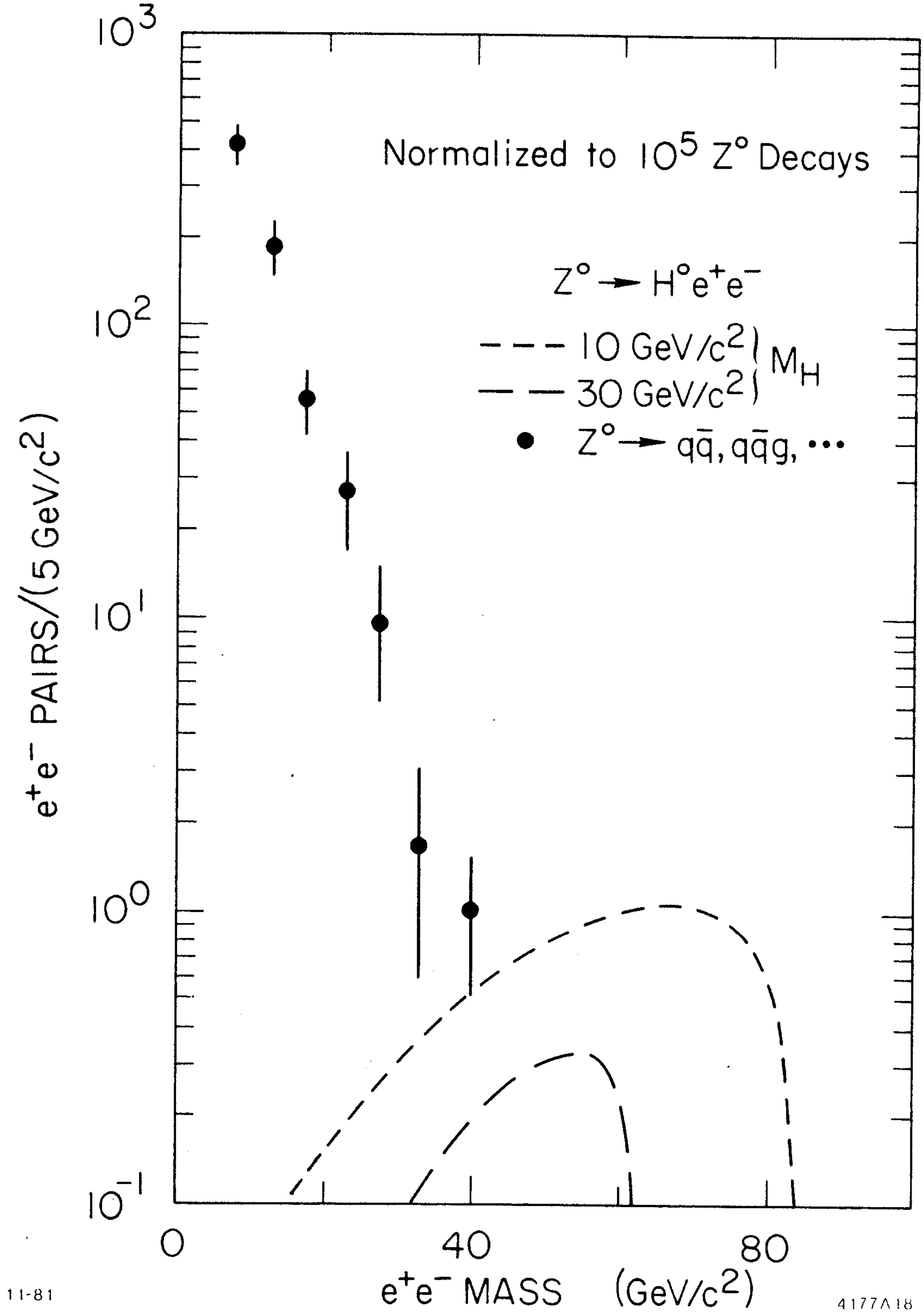

FIG. 13. Signal for Higgs production in the decay $Z^0 \rightarrow H\, e^+e^-$. The effective mass of e^+e^- pairs for various values of the Higgs mass is compared to background expected from hadronic events, mainly t-events. Background from misidentification of hadrons is not taken into account.

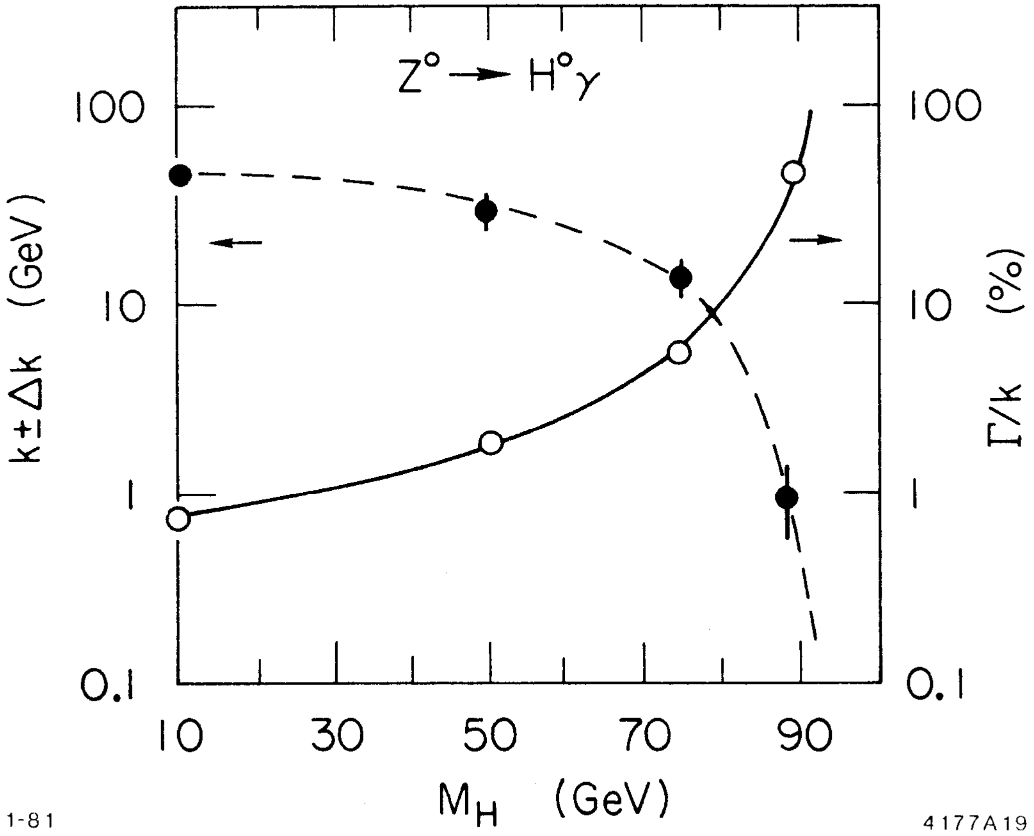

FIG. 14. The detection of the process $Z^0 \rightarrow H\gamma$.
The recoil photon energy k and its absolute uncertainty dk (error bars) caused by the beam energy spread, as a function of the Higgs particle mass. The solid curve indicates the relative resolution in percent (full width) required of a detector to be well-matched to the uncertainty in the beam energy.

In practice the effective beam-broadening is larger than stated above, because the beam width is embedded within the width of the Z^0. This means that instead of a radiative tail, the entire beam envelope is distorted and broadened by initial photon radiation of up to 2 GeV. A precise calculation of this effect is sure to soften the requirements on the detector as outlined above.

Such a very large photon energy requires an extremely large dynamic range for the detector and the electronics.

iii) $Z^0 \rightarrow H^0 \nu \bar{\nu}$

The signal for this decay mode as determined by a full calorimeter would be a large amount of missing energy, not directed parallel to the beam pipe. The mass of the Higgs would be obtained by a measurement of the total energy without pattern recognition. If the Higgs decayed predominantly though t-quarks, then the containment of neutral hadrons becomes important. The mass resolution for a hadron calorimeter of $0.35/\sqrt{E}$ could be better than 10%.

b) Monochromatic photons

Even though these processes may take place at extremely low rates, they may constitute a case for a very high resolution electromagnetic calorimeter.

i) $e^+e^- \rightarrow$ Toponium

If the mass of toponium were only a few GeV below the Z^0 the weak-electromagnetic interference would enhance toponium production and could provide a chance for T spectroscopy.

ii) $e^+e^- \rightarrow \chi_t + \gamma$

This reaction would be allowed by rearrangement of the quarks to form a p-state by emitting a hard monochromatic photon, and would then give rise to toponium ground state via the emission of a soft photon.

B. Hadron Calorimeters

1. Physics Goals

The principle reasons for the use of a hadron calorimeter on the outside of a cylindrical tracking device and a shower counter are the following:

a) Total energy measurement

Given a hadron calorimeter with 4π coverage, a measurement of the total deposited energy, both in magnitude and direction, can serve to:

- reject two-photon background,
- detect neutrinos from leptonic decay of heavy flavors,
- detect neutrinos in heavy leptons, and
- detect $Z^0 \rightarrow$ Higgs + neutrinos.

Measurements at PETRA indicate that the fraction of the total energy carried by neutral hadrons is increasing with energy, and may amount to as much as 20% at SLC energies.

b) Improved momentum measurement

For a detector with a tracking chamber resolution of 0.005p (0.0025p) and a hadron calorimeter with a resolutions of $0.35/\sqrt{E}$, the calorimetric measurement is superior to the tracking measurement above 17 GeV/c (27GeV/c). According to the Monte Carlo prediction, 2% (0.5%) of all charged tracks carry 20% (8%) of the total energy. Thus, a calorimeter would not provide a large improvement, but may still be of interest because the more energetic particles supposedly carry more information. Furthermore, the error on charged particle momenta measured in a solenoidal detector degrades rapidly for smaller angles to the beam axis, and therefore the most significant improvement can be expected for an endcap calorimeter.

c) Jet energy spread

Charged-particle tracking may be rather difficult because of the tight collimation of particles in hadronic events, and consequently a calorimeter may produce a more reliable measurement. This is certainly true for jets produced at small angles to the beam, where the resolution of the drift chamber tracking degrades severely. Since the hadronic shower in the calorimeter is small compared to the size of a jet (typically 100-200 mrad for 50% energy containment), the energy and momentum of the jet can be determined in a calorimeter without resorting to pattern recognition. The mass is obtained by the relation

$$M^2 = E^2(s_x{}^2 + s_y{}^2)/R^2$$

where E is the total energy, s_x and s_y are the second moments of the energy distribution and R is the distance from the beam[3]. Particle ambiguities lead to corrections on the order of 1%.

Energy flow measurements in multi-jet events are limited by the transverse spread of the jets themselves, and therefore the segmentation should be chosen to be substantially smaller than the core of the jet. The study of the energy flow within the jet is limited by the transverse spread of the hadronic shower in the calorimeter and its distance from the IR. The finest observable structure inside a jet would be 40-80 mrad. On the other hand, non-perturbative effects in the hadronization plus the decay of heavier unstable mesons into lighter fragments will presumably make it very difficult to interpret a measurement of such detail. Furthermore, the presence of a magnetic field will spread out the charged particles and may require special techniques to determine the energy spread of the particles in the jet.

d) Muon identification

A calorimeter with five absorption lengths of material would absorb more than 99% of all incident hadrons and therefore serve as an excellent muon identifier. Below 1.5 GeV/c a range measurement might be used to reject hadrons.

e) Electron-hadron separation

In events where a photon of the proper energy converts near a charged hadron, the hadron calorimeter can identify the track correctly as a hadron and not an electron.

f) Hadron energy loss in electromagnetic calorimeters

Hadron calorimetry could play an important role in the understanding of the energy deposition in the electromagnetic calorimeter. A typical shower counter is 15 radiation lengths thick, corresponding to about 1 absorption length. Since 50% of all hadrons produced have momenta below 1 GeV, a considerable fraction of the total hadronic energy will be deposited in the electromagnetic calorimeter (see, for example, the discussion in IV for MAC). An experiment equipped with a hadron calorimeter can measure this effect and be less dependent on Monte Carlo calculations.

2. Options for layout and design

Given the physics goals listed above, there remain several options for the layout of a hadron calorimeter surrounding a cylindrical tracking chamber and an electromagnetic shower counter:

a) The 'full-blown' hadron calorimeter

This design would be expected to meet all the physics goals outlined above, and possibly more. It would aim at the best energy resolution obtainable ($40\%/\sqrt{E}$ or better), and hence require very fine granularity, 2- to 3-mm-thick radiators, good uniformity, nearly equal response to electrons and pions, full solid angle coverage, and an angular resolution better than 15 mrad. The obvious shortcoming of such a detector would be its cost, volume, and weight. Several attempts to overcome these disadvantages will be discussed in the later sections of this report.

b) A 'skimpy' hadrometer

This design focuses on muon detection as the primary task. It suggests three steel slabs, 1.5 absorption lengths thick, interspaced with a planar tracking chamber of good spatial resolution and equipped with analog readout. Combined with an electromagnetic shower detector of excellent spatial resolution and differential and transverse shower detection in 20 radiation lengths, such a device is expected to perform the most important tasks of a hadrometer:

* Muon-hadron separation

Given a total thickness of 5.5 absorption lengths and good spatial resolution to detect hadron scattering, a hadron rejection of better than 100:1 should be obtainable.

* Neutral hadron detection

Monte Carlo simulations indicate that efficiencies for K^0 or neutron detection of 70-80% may be achievable. The energy resolution is estimated to be $150\text{-}200\%/\sqrt{E}$.

* Missing energy measurement

Measurements of the missing energy have been compared to the produced neutrino energy for various detector scenarios. The results, presented in Figure 15 and Table II, show a clear difference in resolution between the 'full-blown' calorimeter

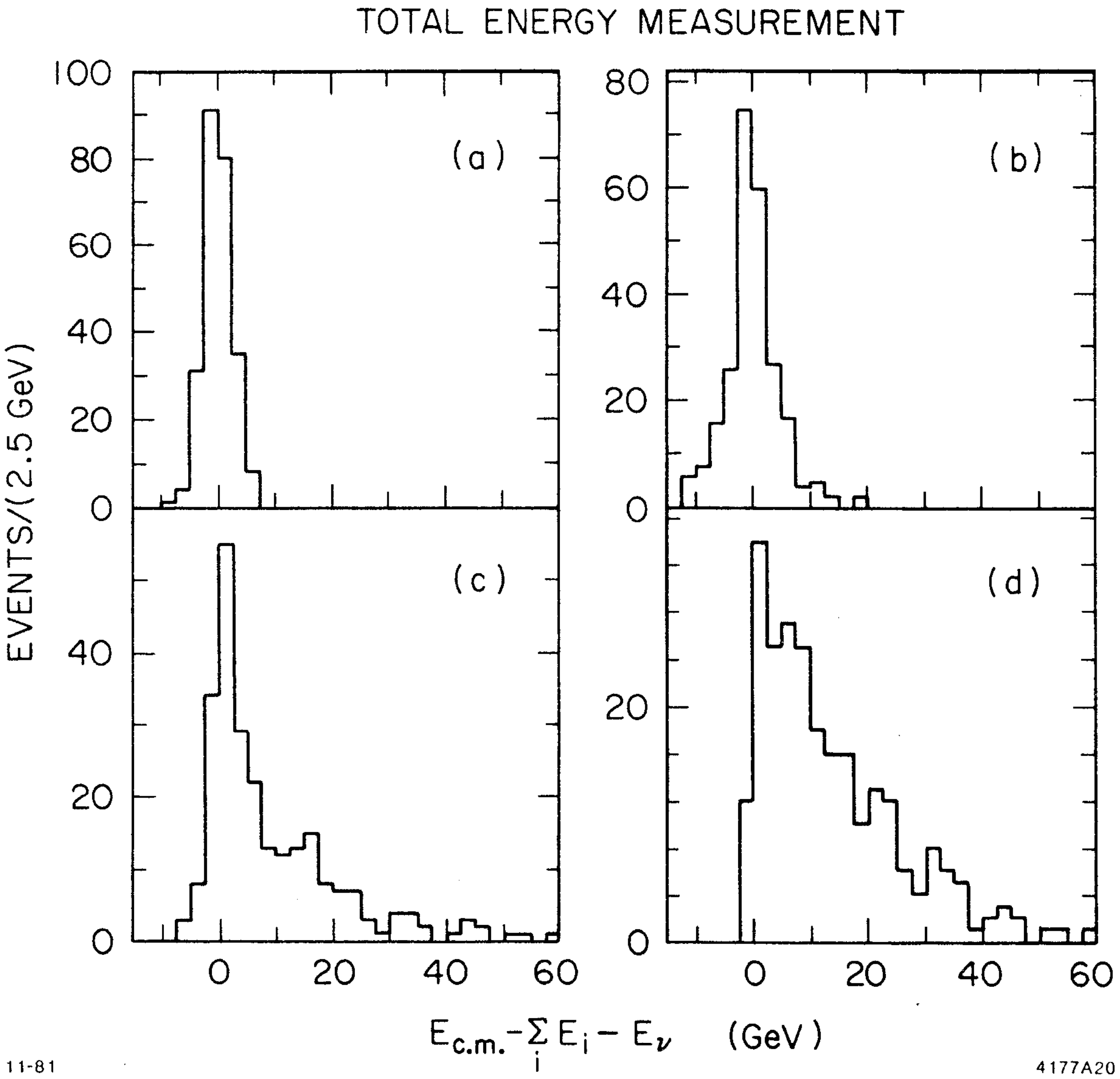

FIG. 15. Measurement of the missing energy for different options for a hadron calorimeter,

a) the complete solid angle coverage with $dE/E=0.70/\sqrt{E}$,

b) the "skimpy" barrel calorimeter with $dE/E=1.80/\sqrt{E}$ and an endcap hadrometer with $dE/E=0.70/\sqrt{E}$,

c) a layout with endcap calorimetry only, $dE/E=0.70/\sqrt{E}$,

d) no hadron calorimeter at all.

and the 'skimpy' one. But this difference is small compared to the very non-Gaussian results obtained for a setup with no hadrometer, or just endcap coverage.

TABLE II

Measurement of the neutrino energy for various calorimeter layouts. The second column is the average difference between the actual energy lost to neutrinos and the energy loss as given by the detector; for a perfect detector this difference would be zero. The third column gives the width of this distribution and indicates the fluctuation in this value. The third column gives the value of difference which includes 99% of all events, and is a measure of the non-Gaussian nature of the distribution.

Choice of Calorimeter	Average (GeV)	Width (GeV)	99% Containment (GeV)
Full	0.1	2.5	7
Skimpy	0.4	4.0	16
Endcap only	6.4	7.8	55
None	12.8	10.9	60

c) Endcap calorimetry only

The idea of placing a hadron calorimeter only at the ends of the cylindrical tracking device is based on the fact that charged particle tracking in this region is very limited and does not allow for a full solid angle coverage (max. 95%). This arrangement does not aim at fulfilling all the physics goals that have been spelled out for a hadron calorimeter; it will not provide muon identification, for example. It may, however, be considered as an addition to the 'skimpy' hadrometer.

d) No hadron calorimetry

This suggestion, like c), does not detect muons or neutral hadrons and does not help to measure the deposition of hadronic energy in the electromagnetic shower counter. In terms of the total energy measurement very good performance of the tracking chamber and the shower detector could result in errors comparable to a calorimeter with a more conventional resolution like 70%/$\sqrt{E}$.

A problem common to any of these schemes is the energy deposition of hadronic particles in the electromagnetic calorimeter, as mentioned earlier.

C. Electromagnetic Calorimeters

1. Physics Goals

The principal reasons for the use of an electromagnetic calorimeter are rather obvious:

a) Measurement of the total electromagnetic energy

In hadronic events photons from π^0- and η-decay carry roughly 28% of the total energy, while electrons carry only 1%. A total energy measurement based on the shower counter and the tracking device will be affected by undetected neutral hadrons (11%) and neutrinos (2%). This introduces larger non-Gaussian errors but does not exclude the use of this measurement for particle searches.

b) Photon detection

The detection of single photons could be important for many interesting questions, in particular the search for rare processes like:

* QCD tests for the radiative emission of hard photons from quarks of different flavor,
* photons from initial-state radiation to tag the process $e^+e^- \rightarrow Z^0 + \gamma$, for a measurement of the total width of the Z^0,
* prompt photons associated with Higgs production,i.e. $Z^0 \rightarrow \text{Higgs} + \gamma$,
* possible monochromatic photons from toponium transitions,
* heavy leptons searches, $E^* \rightarrow e + \gamma$, and

- techni-pions and exotics.

c) Electron detection

A clean separation of electrons from hadrons is an important requirement at Z^0 energies, mainly because the presence of a single electron signals a weak-decay process:

- semileptonic decays of hadrons of different flavor could provide information of the weak couplings of quarks, as they can serve as a tag for t-quark events,
- lepton pair production provides a very handy tool for the basic tests of Weinberg-Salam theory, in particular in the presence of beam polarization,
- searches for heavy leptons remain pivotal to the understanding of lepton spectroscopy,
- Higgs particles production in association with a pair of charged leptons is a very clean signal, and
- many exotic particles that decay weakly will produce electrons.

2. Design considerations

a) Solid angle coverage and location

Since many processes involving single electrons or photons have small cross sections, full solid angle coverage and good uniformity are very desirable. These features are important, particularly for events with missing energy in form of neutrinos. Likewise, any multi-jet analysis will suffer substantially from incomplete solid angle.

Full photon detection efficiencies and good resolution for energies below 400 MeV as well as e/π separation to better than 10^{-2} can only be obtained with rather fine sampling at the front end of the electromagnetic calorimeter. This would mean that at least a fraction of the shower detector be placed inside the solenoidal coil of the magnet, while the hadron calorimeter would go to the outside, i.e. with an inner radius of at least 2 m.

b) Inclusive Photons

Measurements of inclusive photon production will be as difficult at the SLC as at any other machine. The main problem is due to backgrounds from the decay of π^0 and other neutral mesons, interactions of neutral hadrons in the shower detector, and initial state radiation. The identification of single photons, at energies above a few GeV, depends primarily on the ability to resolve photons from π^0 decay, i.e. on the ability to determine whether there are two showers or one. The opening angle of two photons is approximately $\theta=2M/P$ where M is the mass, P the momentum of the decaying meson. The separation at a distance L will be

$$d = L\cdot\theta = 2ML/P.$$

Let d_{min} be the minimum separation at which the shower of two photons can be differentiated from a single photon. For L=1.5 m, we obtain a maximum momentum for a π^0 to be detected.

d_{min} (cm)	Pmax (GeV/c)
1	42
2	21
5	8.4

Typical fine-grained detectors, such as liquid argon[4] or lead-scintillator with strips of 2 cm width can obtain spatial resolutions of 1.5 - 2.0 cm. Lead and proportional tube calorimeters with 1- to 2-cm-wide tubes should yield similar values for d_{min}, but generally suffer from lower average density than liquid argon calorimeters. Separation of π^0's from photons above 20 GeV will probably require a converter in the tracking volume--a drift-calorimeter[5] which measures the photon position in the first few radiation lengths after conversion.

The detection of π^0's at energies below several GeV suffers from large combinatorial background. Figure 16 shows an effective mass plot for calorimeters of different resolution. In the optimistic case with resolutions of 5 mrad and $10\%/\sqrt{E}$, the signal-to-noise ratio is roughly one.

c) Electron-pion separation

Electrons differ from pions not only by the amount of energy deposited, but also in their transverse and longitudinal shower development. Abshire et al.[6] have demonstrated that a very fine sampling Pb-scintillator-sandwich counter with three longitudinal readout sections can give pion rejection of greater than 1000:1, while maintaining an electron detection efficiency as high as 80% for energies from 2 to 6 GeV. The Mark II liquid argon system has obtained rejection rates of 100:1.[4] Better separation can only be obtained with rather fine sampling at the front end of the calorimeter. This would mean that at least a fraction of the shower detector be placed inside the coil of the magnet.

The primary requirements that e/π separation places on spatial segmentation are that there be

- at least 2, and preferably 3, longitudinal readout sections, and
- a transverse segmentation not necessarily small enough to observe the actual shower size, but small enough to prevent frequent overlap between photons and charged tracks, which could fake electron signals.

The determination of the actual spatial resolution requires a

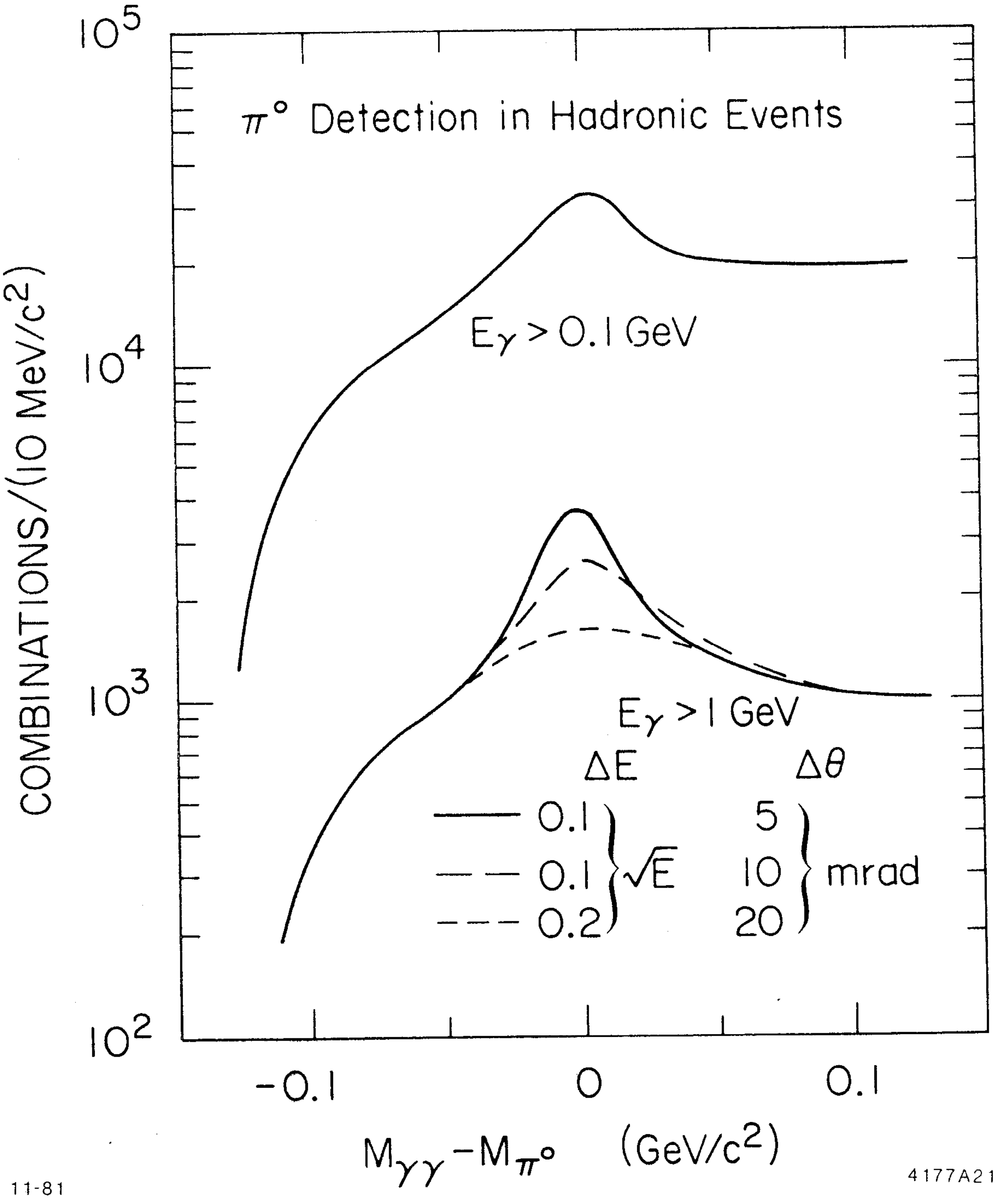

FIG. 16. Detection of π^0 in hadronic decay of the Z^0. The effective mass of any pair of photons is plotted for two different cuts on the photon energy, and different resolutions of the shower detector.

detailed Monte Carlo study with realistic algorithms for electron identification and hadron interactions in the shower set-up.

d) Shower overlap

Particle identification and energy measurements in a calorimeter can be seriously affected if several particles hit the same detector segment. Using the hadron Monte Carlo one can estimate the average number of extra particles hitting a solid angle element centered on an incident photon or electron. The results are given in Table III for a cone of half-opening angle 25 mrad. These numbers are averages and do not take into account the rapid change in particle density near the center of a jet. From the numbers given in the table we conclude that detector elements corresponding to cones of half-angle 10 mrad are needed for photon detection above 1 GeV with less than 10% overlap by other particles.

A more detailed calculation including energy deposition by interacting hadrons is needed to obtain more reliable estimates.

TABLE III

Multiple hit problem for calorimeters: The average number of background particles within a cone of half-opening angle of 25 mrad with respect to the incident electron or photon.

	Incident Particle			
	Electron		Photon	
Background particle	All	E>1GeV	All	E>1GeV
All Particles	0.17	0.25	0.21	0.59
Electron or Photon	0.08	0.13	0.13	0.39
Electron or Photon $E > 0.1 \cdot E_{inc}$	0.08	0.13	0.13	0.37
Hadrons	0.073	0.11	0.08	0.20

References

1. A. Ali, E. Pietarinen, J. Willrodt, DESY Internal Report T-80-01.

2. G. Barbiellini et al. SLAC-PUB 2744 (1981)
   E. Ma and J. Okeda, Phys. Rev. Lett. 41, 289 (1978)
   K. J. F. Gaemers, R. Gastman, R. M. Renard,
   Phys. Rev. D19, 1605 (1979).

3. V. Cook et al., Nucl. Phys. B186, 212 (1981).

4. D. Hitlin et al. Nucl. Instr. and Methods, 137, 225 (1976).

5. L.E. Price and I. Ambats, IEEE Transactions of Nucl. Science
   Vol. NS-28, 506 (1981).

6. G. Abshire et al., Nucl. Instr. and Methods, 164, 67 (1979).

This section is, in parts, a summary of the following
SLC Workshop notes:

#24 Do we need a hadron calorimeter?,
R. Hollebeek, J. R. Johnson, P. M. Mockett.

#29 Calorimeter resolutions,
D. Coyne, V. Luth, L. Price, H. Williams.

#19 Measurement of jet properties at SLC energies,
V. Luth.

#37 Can the decay $\tau \to \rho\nu$ be measured directly?,
J. Hauptman.

III. CALORIMETER READOUT GEOMETRIES

Any consideration of the geometrical volumes into which a calorimeter is to be subdivided depends critically upon the available technologies, costs and physics objectives. We shall emphasize the last, and consider two topics: average jet parameters and reconstruction of individual particles within jets.

For $Z^0 \rightarrow$ quark-pair decays generated by the TUBES[1] Monte Carlo, the higher energy particles in the jets tend to be collimated into a few tens of milliradians. The average angle, α, subtended by projective strips or square towers in a 4π solid angle calorimeter with N channels is given by

$\alpha^2{}_t = 4\pi/N$ (for towers)

$\alpha^2{}_s\ (\ell/3s) = 4\pi/N$ (3 views of projective strips)

where ℓ = strip length, s = strip width.

For a fixed number of channels,

$\alpha_s \simeq = \sqrt{(3s/\ell)}\ \ \alpha_t$.

For a typical specific geometry, $\sqrt{(\ell/3s)} \simeq 10$, $\alpha_s \simeq 5$ mrad, $\alpha_t \simeq 50$ mrad, yielding 5000 channels in the front section (or 10,000 channels if two more sections in depth are added), each with twice the cell size of the front section.

For the first topic of studying only the gross features of jets and their production, projective towers of modest dimensions (10 X 10 cm^2) placed at a radius of 2.0 meters ($\alpha \simeq 50$ mrad) would suffice to measure the jet axis and the lower moments of the jet energy pattern. Isolated and high transverse momentum particles would be measured directly and without ambiguity.

For the reconstruction of individual particles within jets, towers are inadequate even for a large (10^4 channels) system. Narrow projective strips in three or more stereo views offer the possibility of untangling individual photon showers in high density environments. A system with strip widths of 1.0 cm at 2 meters ($\alpha \simeq 5$ mrad) is capable of identifying and reconstructing with some confidence even a 15 GeV neutral pion. Therefore, the identification of simple final states such as τ decay to ρ is possible.

For hadronic events at the Z^0, we have compared the frequencies with which individual channels are struck, the relative abilities of each system to measure average jet parameters, and the capability for individual photon reconstruction. Parts of this study were carried out analytically, while others resorted to a full EGS electromagnetic shower program plus a hadronic Monte Carlo simulation of complete $Z^0 \rightarrow$ quark-pair events.

Projective geometries are optimal for shower reconstruction, since the shower develops along the axes of the geometric channels. Hence fluctuations in depth development do not affect the apparent centroid of the shower; in non-projective geometries, these fluctuations introduce correlations with the reconstructed shower position.

Based on the present study we believe that a hybrid system of projective strips and towers offers the best opportunity for detailed analysis of the relatively small Z^0 sample produced by the SLC. The weaknesses of each of the two geometries are compensated by the strengths of the other. Thus, the geometrical ambiguities of the stereo strip system are largely removed by the tower structure, and the spatial crudeness of the towers is overcome by the precision of the strips.

A. Measurement of Average Jet Properties

In an n-view strip system the projected spatial distribution of energy deposited in a cluster can, to a large extent, be determined separately for each view without matching views and resolving ambiguities to localize particle hits. In a multi-jet environment, this requires that:

1) A means exists to identify which strip signals to include in a particular cluster. This implies that in at least two views the higher-energy particles in two distinct clusters not share the same strips.

2) Hadrons, electrons and photons be counted with correct energy response of the calorimeter. This requires either a uniform medium deep enough to contain the hadronic showers, or a means (using longitudinal segmentation or knowledge of the tracks) to distinguish photons and electrons from hadrons. This need not be done with 100% efficiency.

The simplest case to discuss is n=2: a projective system of longitudinal wires (ϕ-view) and azimuthal (θ-view) strips in the same gaps for a gas detector. For equal-width strips in the two views, and $L \simeq 2R$, an arrangement with three 120° azimuthal sectors, as shown in Figure 1, not only yields roughly equal strip areas for the two views, but also provides a natural way to meet the first requirement listed above, at least for two-jet events. Momentum flow disributions and projected moments in ϕ and θ are readily determined. While one cannot take the next step--to $p_\perp$ distributions--in the presense of ambiguities with n=2, jet models can still be confronted with the projected information. (The projections can be used to compute approximately the

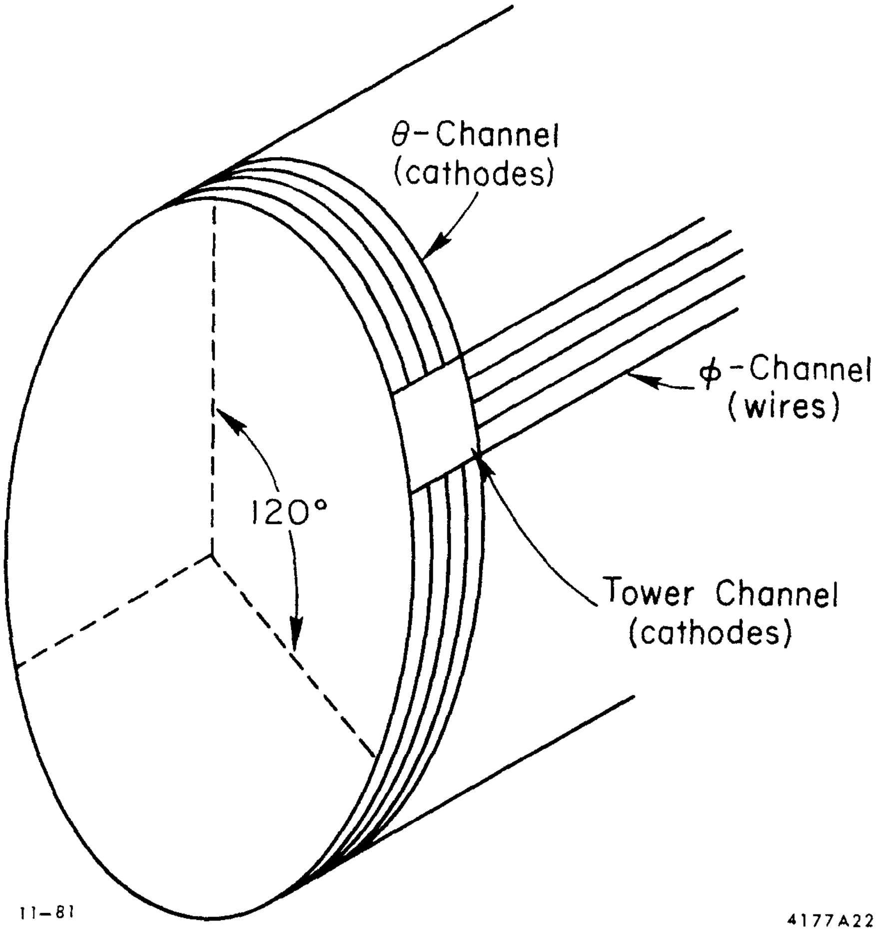

FIG. 1. A two-view plus tower system; the polar view (θ) is segmented each 120 °, the azimuthal view (φ) is axial and defined by the anode wires, and the towers cover an integral number of strip channels.

jet axis and the rms $p_\perp$ of the jet but not the higher moments of the distribution. The jet axis in one coordinate should be quite accurate, subject to the inclusion of the right strips in the cluster.) The rms width is subject to fractional errors of the order of an appropriately weighted mean-square jet angle; a Monte Carlo simulation can be used not only to estimate this better, but also to correct for it. We emphasize that only projected information in one coordinate may confront a model, since ambiguities will not allow a measurement of, say, $d^2N/d\cos\theta\, d\phi$, but only $dN/d\theta$ and $dN/d\phi$.

We do not advocate a 2-view system, but have tried to show that this sort of physics is less demanding than is full jet reconstruction, which obviously requires a third view. Perhaps the most attractive way to add a view is with a strip-tower hybrid arrangement, in which the two orthogonal strip views (θ and ϕ) are maintained and projective rectangular towers are added. Tower boundaries would coincide with an integral number of strip boundaries. The entire system is easy to visualize and simpler to analyze than a system of three non-orthogonal views of strips, since the pair of strip views and the tower view separately provide a good deal of information (see Figure 1). Similar considerations apply to endcap calorimeters. For jets overlapping the barrel and endcap regions, the use of ϕ and θ strips in the endcaps would provide a natural geometrical match.

Another method of implementing a strip and tower hybrid scheme may involve relatively large towers (25 by 25 cm^2) that are subdivided by a grid of x and y strips. The strips serve to give the projected energy patterns from which the four vector energy-momentum sum of all the particles striking the tower can be determined. As long as the size of

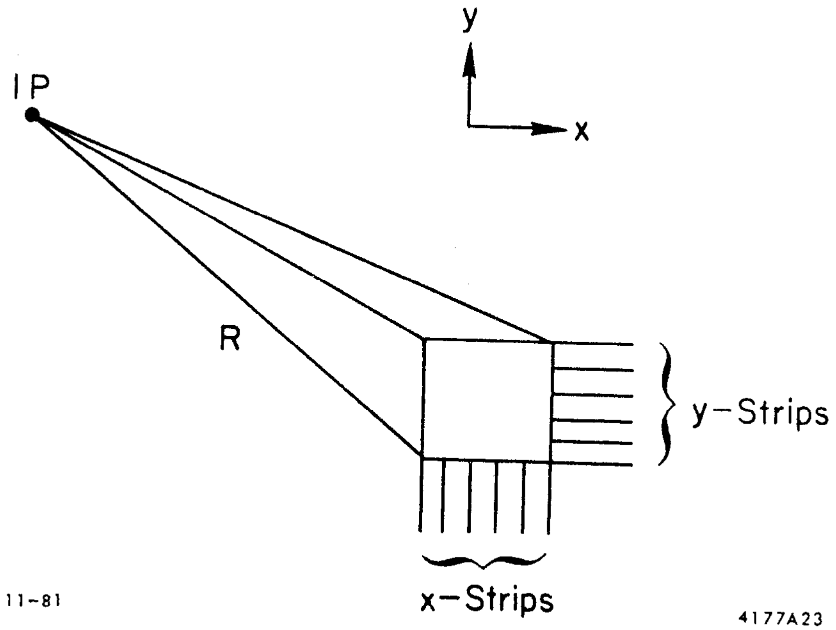

FIG. 2. Two-strip plus tower hybrid with generalized x,y coordinates for computing the jet mass and average p_x and p_y.

the tower is small compared to the distance of the tower from the interaction region, then all that is required to reconstruct the energy-momentum four-vector accurately are the projected first and second moments of the energy distribution and the total energy. If we denote the total energy as E and the first and second moments of the projected energy distribution as $\langle x\rangle$, σ_x, $\langle y\rangle$, and σ_y, then for a tower a distance R from the interaction point the four-vector is obtained from the following relations:

$$p_x = E\ \langle x\rangle/R$$

$$p_y = E\ \langle y\rangle/R$$

$$m = E\sqrt{(\sigma_x^2 + \sigma_y^2)}/R.$$

Correlations between x and y enter as a correction which goes as $1 + \sigma_{xy}/R^2$ and are of order one percent. Hence, in this scheme an excellent measurement of the jet parameters can be obtained. Since no pattern recognition is required the analysis is straightforward. However, it is tacitly assumed that the electromagnetic calorimetry is accompanied by hadronic calorimetry and that the response to hadrons and photons and electrons in the calorimeters is similar.

B. Individual Photon Reconstruction

The following analysis assumes a sampling calorimeter using lead as the converting medium. We have simulated both the electromagnetic and hadronic interactions in the electromagnetic calorimeter. The coordinates of all charged particles which cross the sensitive gaps are saved. The simulation was done with vacuum gaps; for liquid argon, scintillator or other sensitive media, the nuclear absorption length is underestimated. A signal is assigned to each track with a fluctuation appropriate to the collection mechanism and energy deposition. These tracks may readily be summed into channels of any geometry. Such detail allows more precise study of efficiency and shower overlap losses.

Definition of Geometries

We make several restrictive, but reasonable, assumptions.

For both tower and strip systems:

(1) 4π solid angle is covered by a cylinder plus two end caps; the front face of the module is a distance 1.5 meter from the interaction point (Figure 3a).

(2) all sampling elements are "projective", i.e. all strips and towers are aligned with the luminous region (Figure 3b);

(3) there are $\lesssim 10^4$ channels in the whole system; and

(4) there are three electronic sections in depth, each having about 6 X_0 of lead, sampled evey 0.3 X_0 in a 5 mm gap.

For the strip system:

(5) there are three stereo views at 0° and ±60°;

(6) the strip width is s cm in the front section, and 2s cm in the back two sections; and

(7) the strip channels are electrically separated at the center of the cylinder.

For the tower system:

(8) the tower dimension is t cm in the front section and 2t cm in the back two sections.

The number N of electronic channels (or separate sampling volumes) as a function of the strip width s, tower dimension t, cylinder length L, and radius R is given by[2]

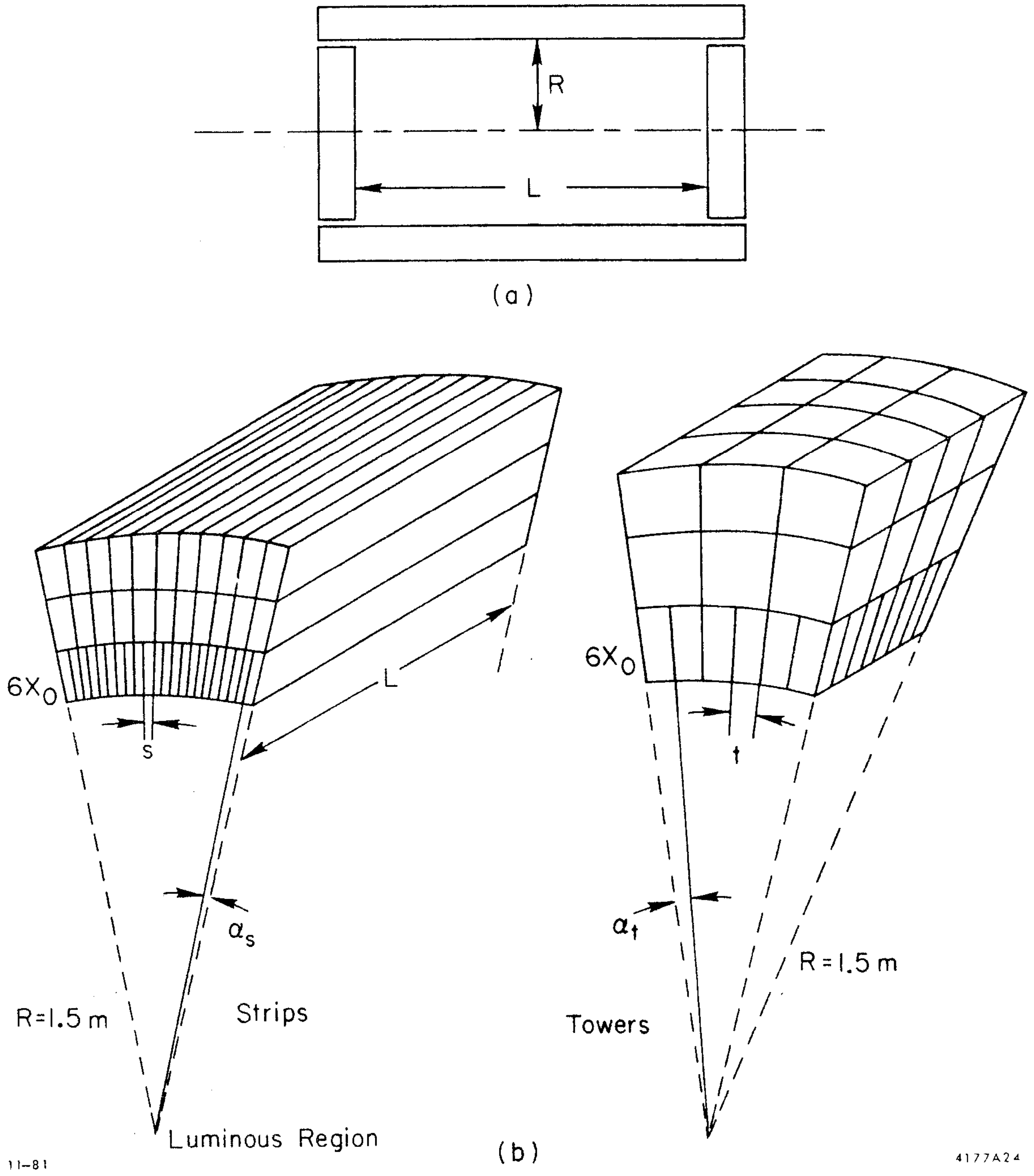

FIG. 3. The overall calorimeter geometry, and the projective calorimeter geometries for strips and towers. The other stereo views of the strip system are not shown.

$$N_{strips} = ([2\pi R/s + 2\cdot 2\pi R/2s] + 3\cdot 2R/s)(1 + \tfrac{1}{2} + \tfrac{1}{2})\cdot 2$$

$$= (8R/s)\cdot(2\pi + 3)$$

$$N_{towers} = (2\pi RL/t^2 + 2\pi R^2/t^2)(1 + 1/4 + 1/4)$$

$$= (3\pi R/t^2)(L + R)$$

$$= (9\pi R^2)/t^2 \qquad \text{for } L = 2R$$

then for N channels,

$$s = (8R/N)(2\pi + 3)$$

$$t = 3R\sqrt{(\pi/N)}$$

These channel sizes are plotted against N in Figure 4.

Full reconstruction of Z^0 jets will be an effort of limited success. Nevertheless, pursuit of such a difficult objective will make more obvious the strengths and weaknesses of different calorimeter geometries.

a. Analysis of strip system. For any point in two-dimensional (e.g. θ,ϕ) space, a function is defined to be the product of the three stereo view amplitudes observed at that point. For points within a shower all three stereo views have significant signals, and this triple product is relatively large. On the other hand, this product is zero if any one of the stereo amplitudes is zero. The surface representing this function closely resembles a histogram of signals from high resolution towers. In practice, this amplitude function is discretely and approximately sampled in each stereo view by the strip channels; these signals are used directly in the triple

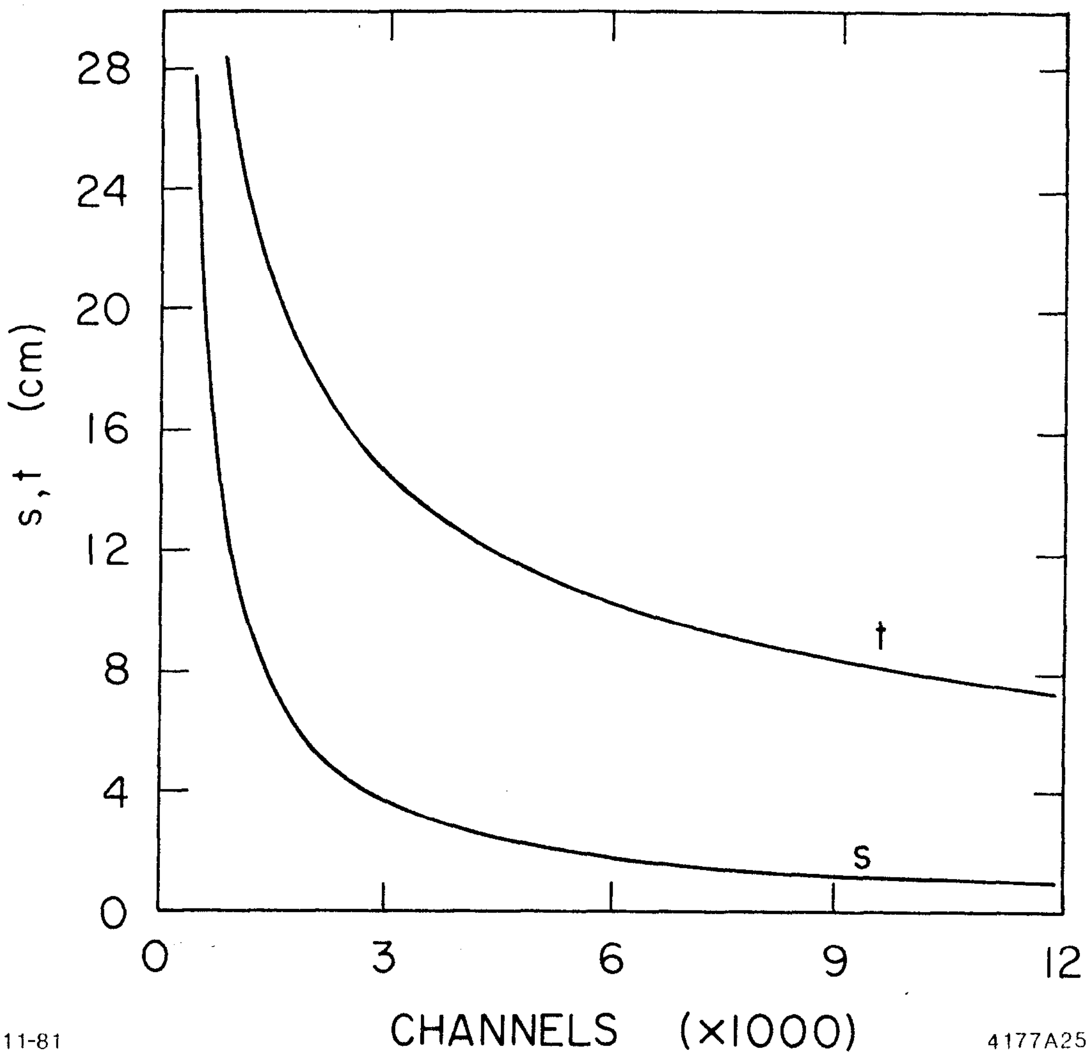

FIG. 4. Strip (s) and tower (t) sizes as a function of total number of channels for the typical geometry.

product since the channels widths are comparable to or smaller than shower widths in the calorimeter. The cube root of the product is then plotted.

b. Analysis of the tower system. Tower signals are displayed directly as a histogram in two dimensional space.

c. Analysis of the strip-tower hybrid. As in the strip system, a product of three stereo views is calculated. The tower signal which spatially overlaps the stereo intersection point multiplies this product, yielding a "quadruple product". The fourth root is taken to help the display.

A picture of a typical Z^0 event in the calorimeter is shown in Figure 5. For this event the triple product surface for a strip system, the signals for a tower system, and the quadruple product for a hybrid system are shown in Figures 6, 7, and 8, respectively. For each system the total number of channels was the same.

The triple product is displayed as a "surface" plot in Figure 6(a) and as a contour plot in Figure 6(b). The particle impact positions on the face of the calorimeter are shown in Figure 6(c) on the same scale used for 6(b). An overlay of 6(c) onto 6(b) reveals distinct local maxima at all impact locations, but also several "ghost" maxima generated by stereo ambiguities.

In Figure 7(a-c) we show the same plots for the tower system. Isolated showers are unambiguous, but it is impossible to distinguish the two, and sometimes three, particles which populate the same tower.

In Figures 8(a-c) we show the quadruple product of a strip-hybrid system. An overlay of Figure 8(c) onto 8(b) reveals that all hits have local maxima. Those ambiguities which remain within each tower are

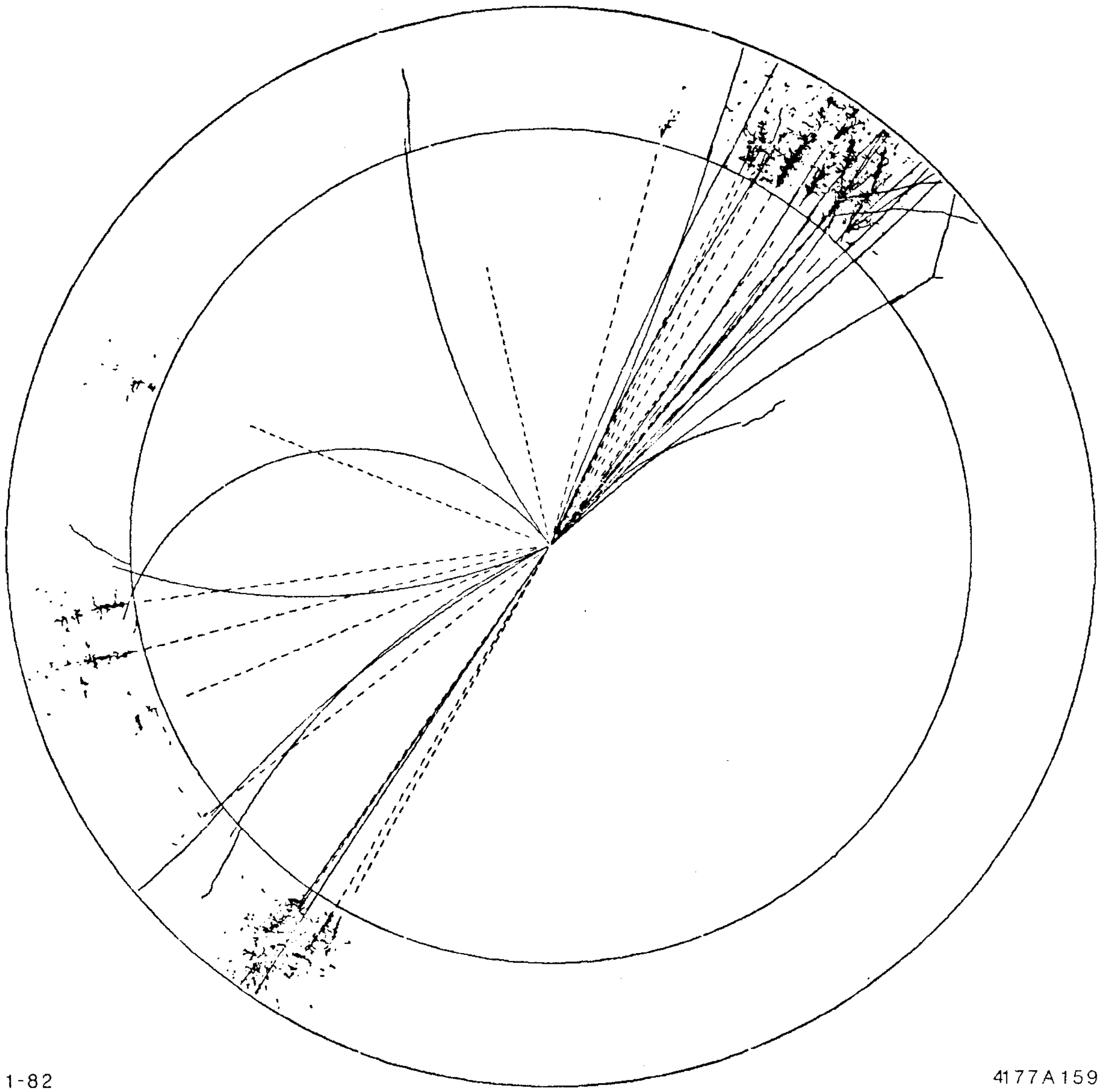

FIG. 5a. A typical Z^0 event in an electromagnetic calorimeter. The short dashes are photons, the solid lines are charged hadrons, and the long dashes are neutral hadrons.

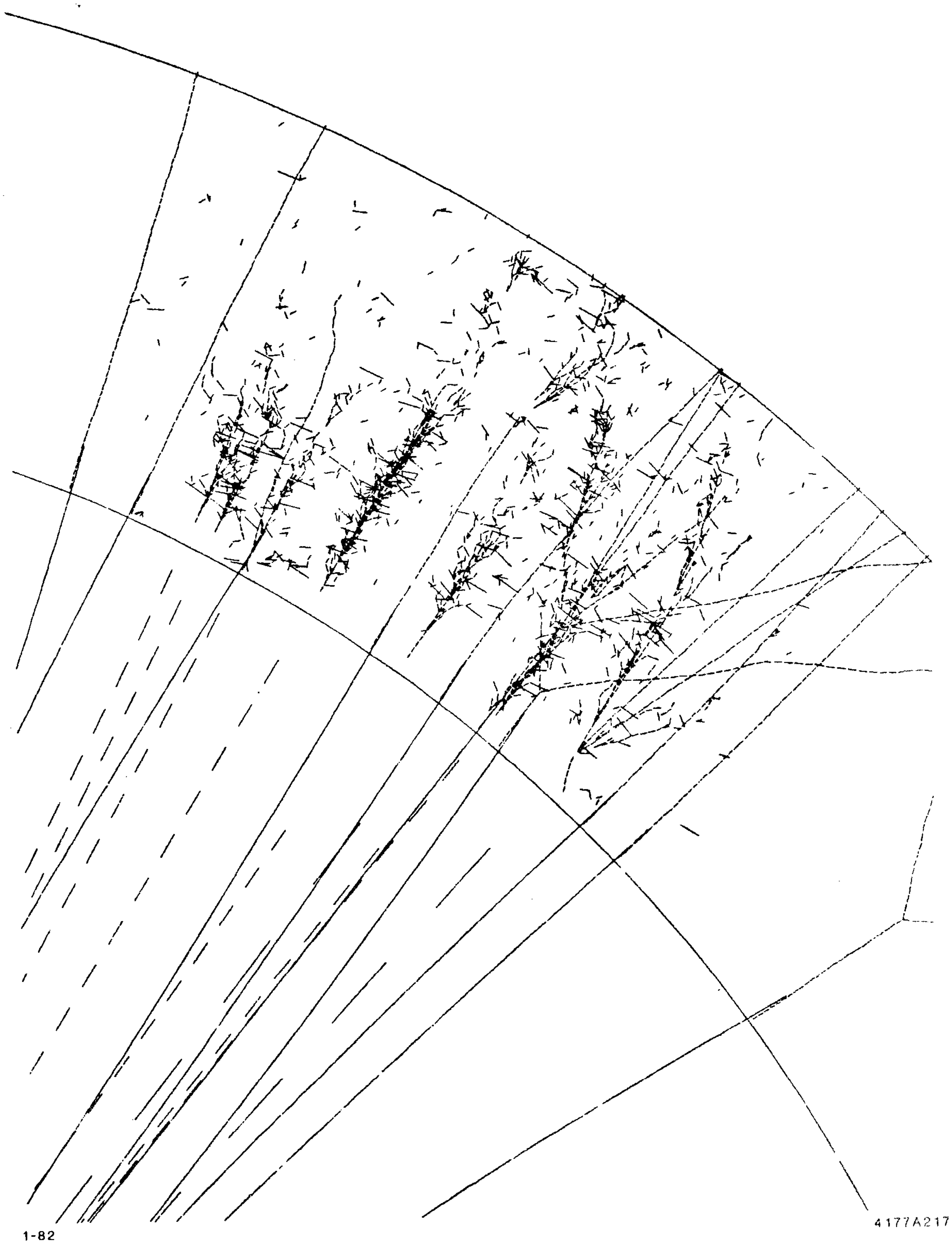

FIG. 5b. An enlargement of part of the event of Fig. 5a.

relatively easy to resolve by allocating the expected signals of the highest energy shower in each view first, and then continuing on with the next lower energy photon. Once the channel signals in any one view are attributed to a shower, the ambiguity is removed. (Note that in Figures 6 and 8 the plot axes labelled p,q are in fact oriented at 60° with respect to each other; the third stereo axis crosses this plot diagonally. In Figure 7, the two tower coordinates u,v are perpendicular to each other, and are plotted as such.)

Although an analysis has not been made for the 2-view strip-tower hybrid system for average jet parameters, we expect that it will perform about as well as this 3-view strip-tower hybrid system.

A study of a few of these pictures leads us to conclude that as far as individual photon reconstruction is concerned, a strip system is superior to a tower system and a hybrid system combining both is clearly superior to either strips or towers alone. This is not surprising since a hybrid system contains more information. The ambiguity problem with stereo strips is largely solved by using the towers as a pattern recognition "enable" in order to define which strip intersections are to be taken seriously. Conversely, the tower signals can be used alone for direct energy flow analyses or together with the strips in searches for energetic single photons from, for example, Higgs decays.

C. Enhanced Photon Position Measurements

Since pattern recognition will be an important consideration in the investigation of exclusive final states, the electromagnetic calorimeter should be supplemented with a front end which can detect the conversion of individual photons.

A measurement of the precise photon position will contribute in five

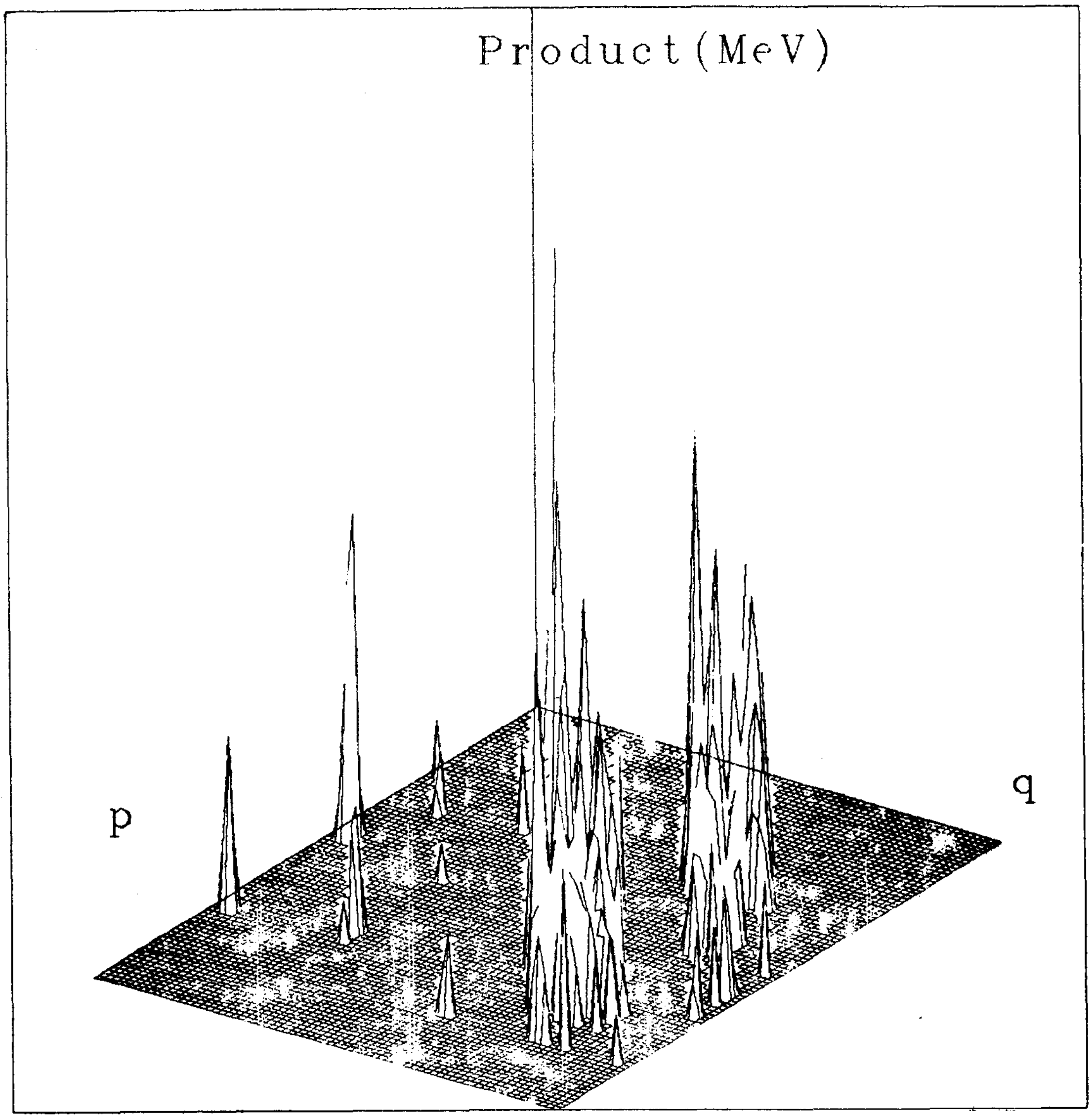

FIG. 6a. This surface plot of the triple product of strip signals is produced by analyzing the response to the event of Fig. 5.

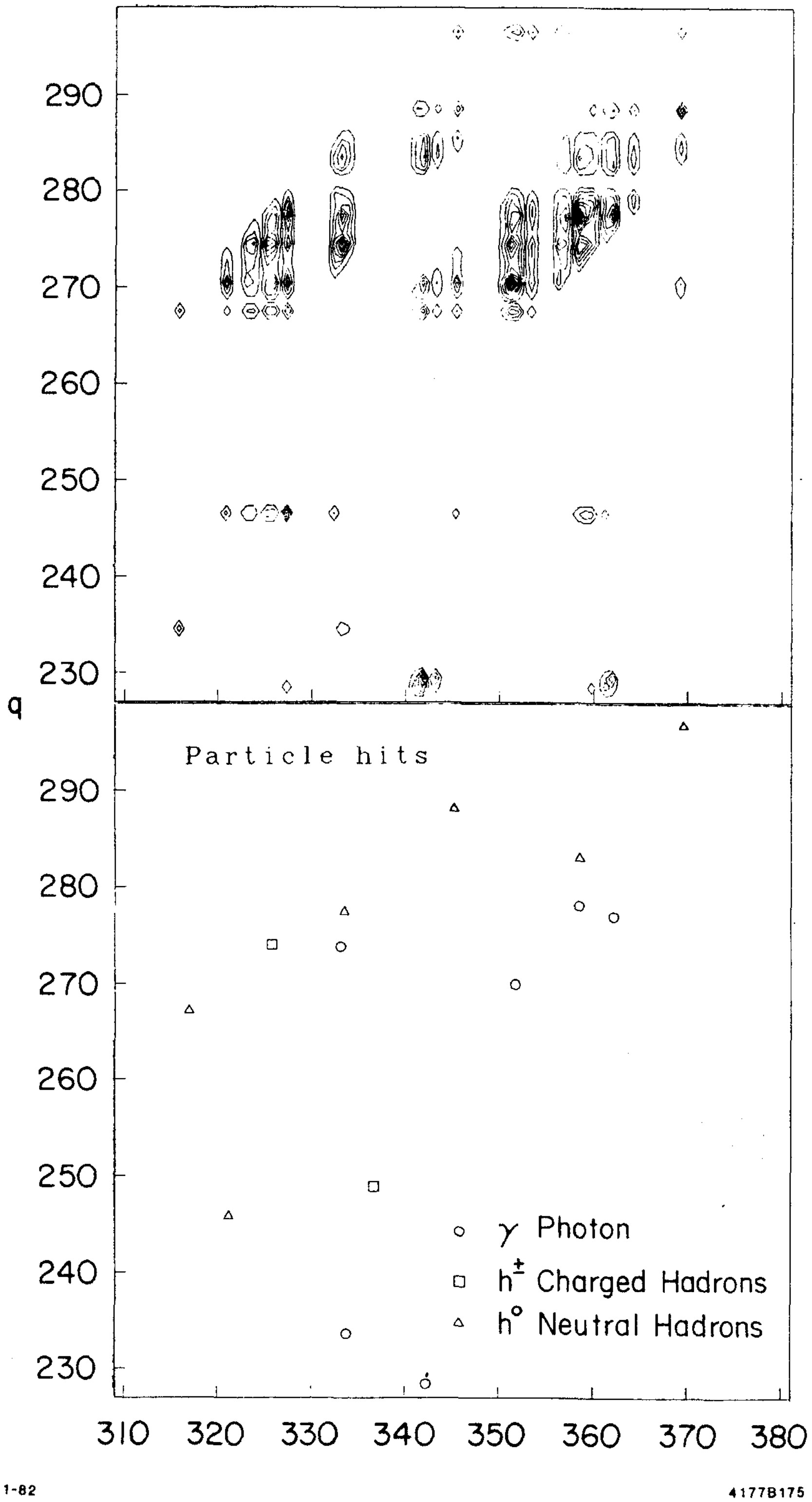

FIG. 6b,c. The contour plot (a) and impact position (b) for a strip system and the event of figure 5.

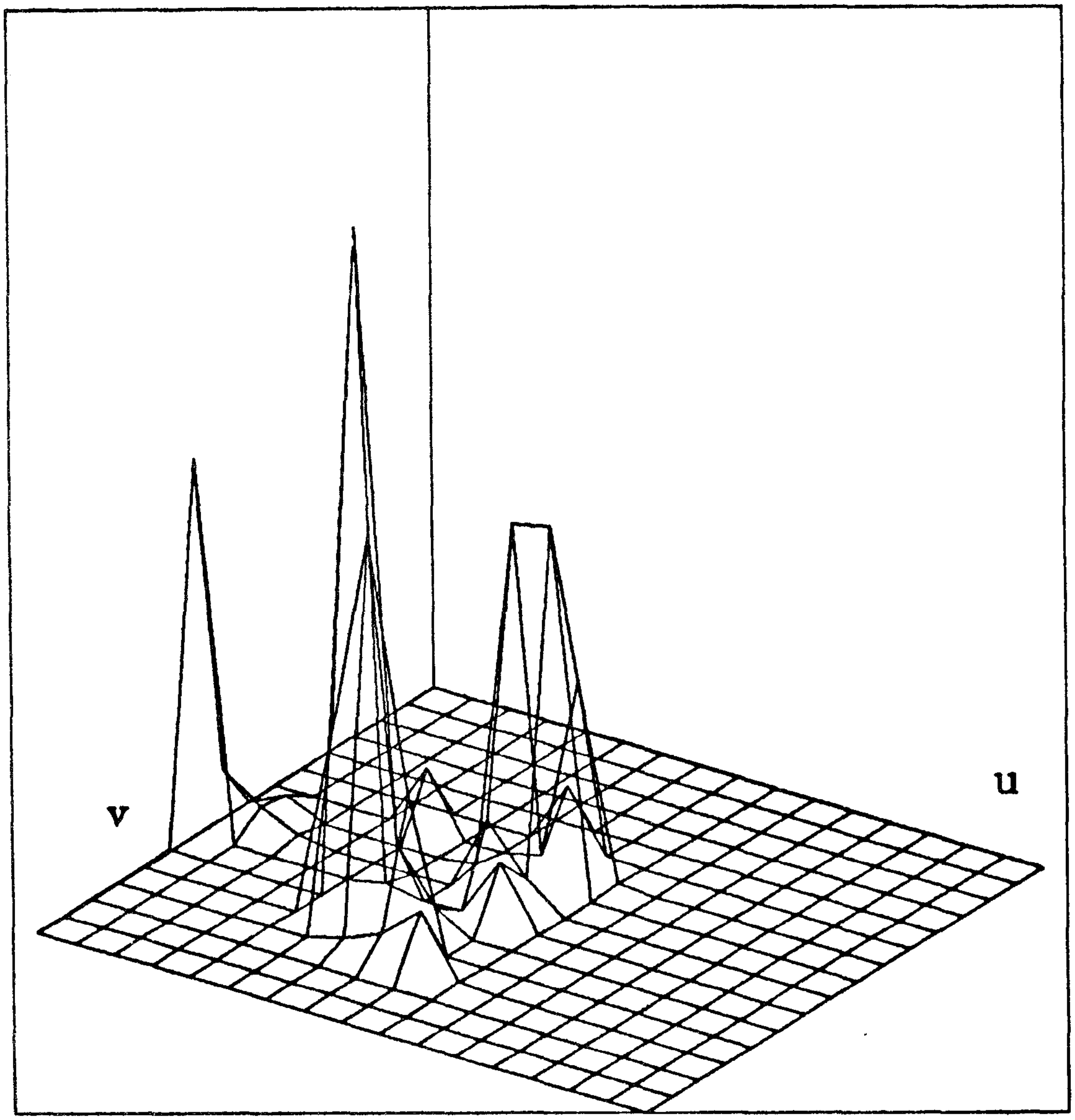

1-82

4177A173

FIG. 7a. A surface plot of tower signals for the tower geometry and the standard event.

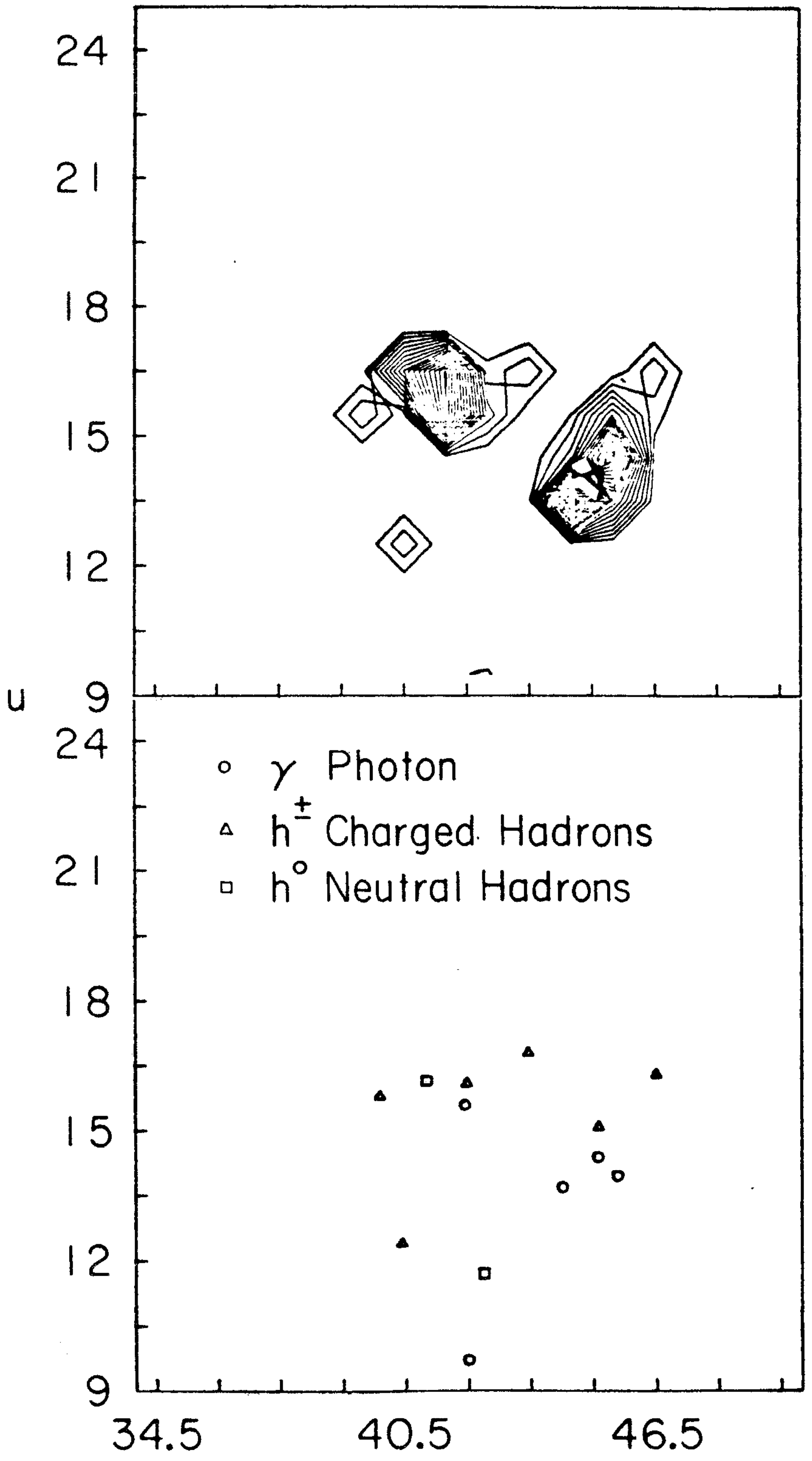

1-82 4177A176

FIG. 7b,c. The contour plot (a) and impact position for the tower geometry.

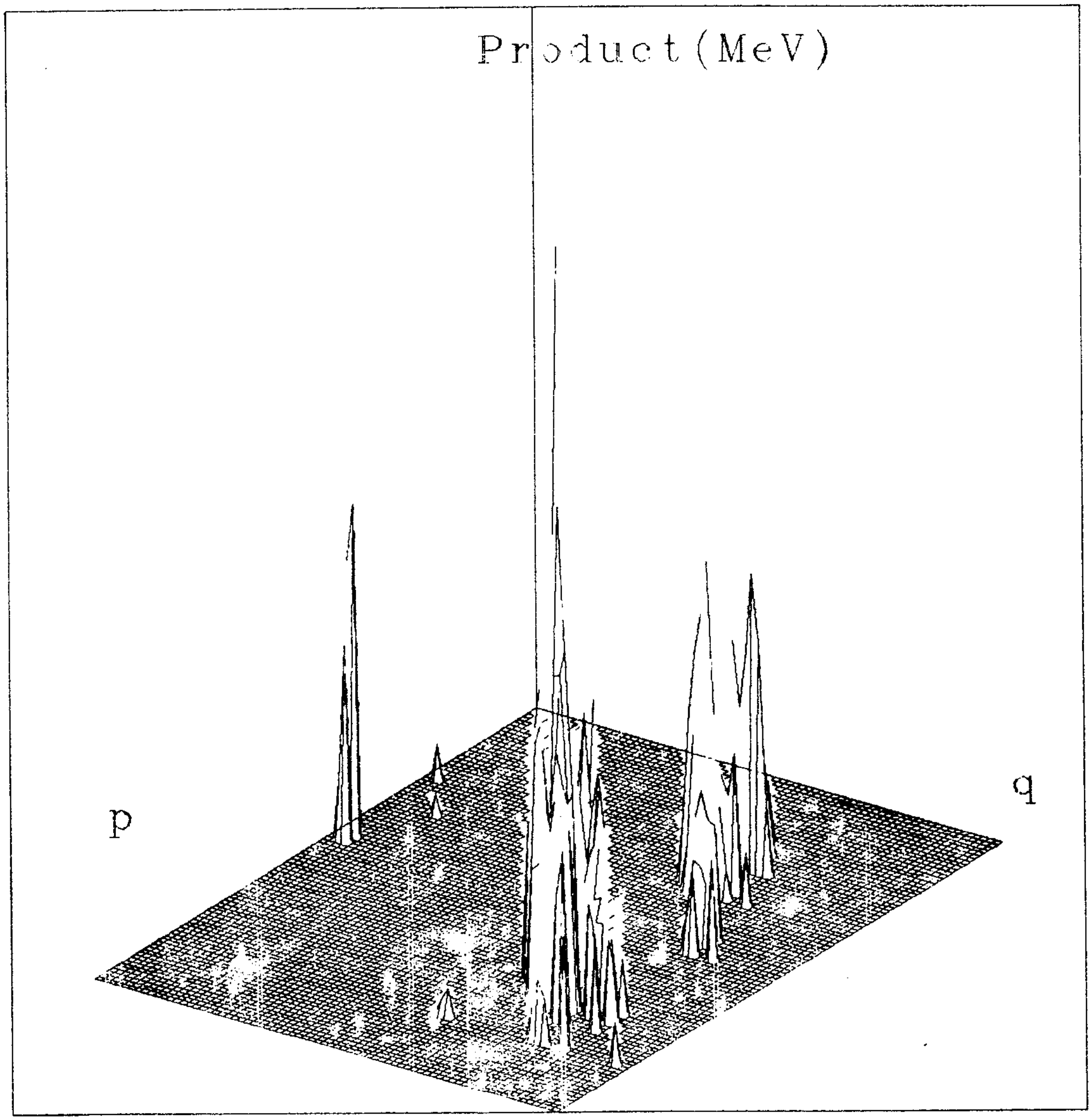

1-82 4177A174

FIG. 8a. A surface plot of the quadruple product for a hybrid strip and tower system with the standard event.

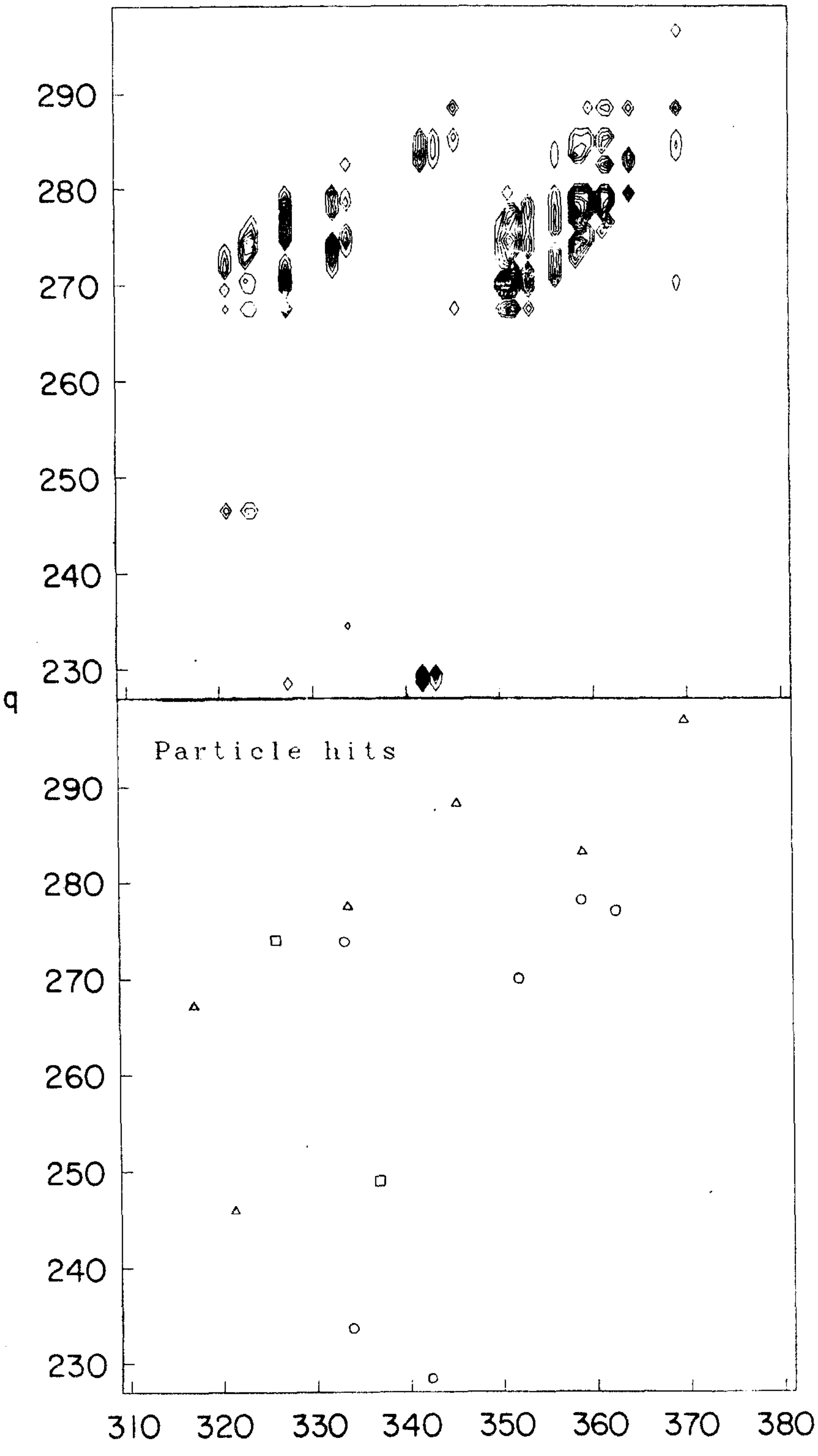

FIG. 8b,c. The contour plot (a) and impact position for the hybrid system of strips and towers and the event of Fig. 5.

important ways to the shower measurement:

(1) For less than total absorption in the shower chambers, the conversion point in depth will be measured and the energy fluctuations induced by conversion point fluctuations reduced;

(2) The transverse location of the conversion point provides an excellent means of determining how the energy is shared among the strips;

(3) Pion-electron separation is enhanced by a) distinguishing between a pion and a nearby photon and electron, and b) by noting the details of the shower build-up in the first few radiation lengths beyond the conversion. The precise criteria for an electron can be determined according to the physics needs of efficiency and background rejection.

(4) An excellent measurement of the photon-photon mass can be obtained without measuring separately the energies of the individual photons, but only their sum. The natural line width is independent of the total energy, and is shown in Figure 9. This would be especially useful for high energy π^0's where the granularity of the shower detector might make it difficult in many cases to separate the photon energies.

(5) Improved low energy photon efficiency will be possible with this front end.

A selection of photon showers, showing each individual charged particle gap crossing, is included as figure 10 to see how this front end might determine the conversion point.

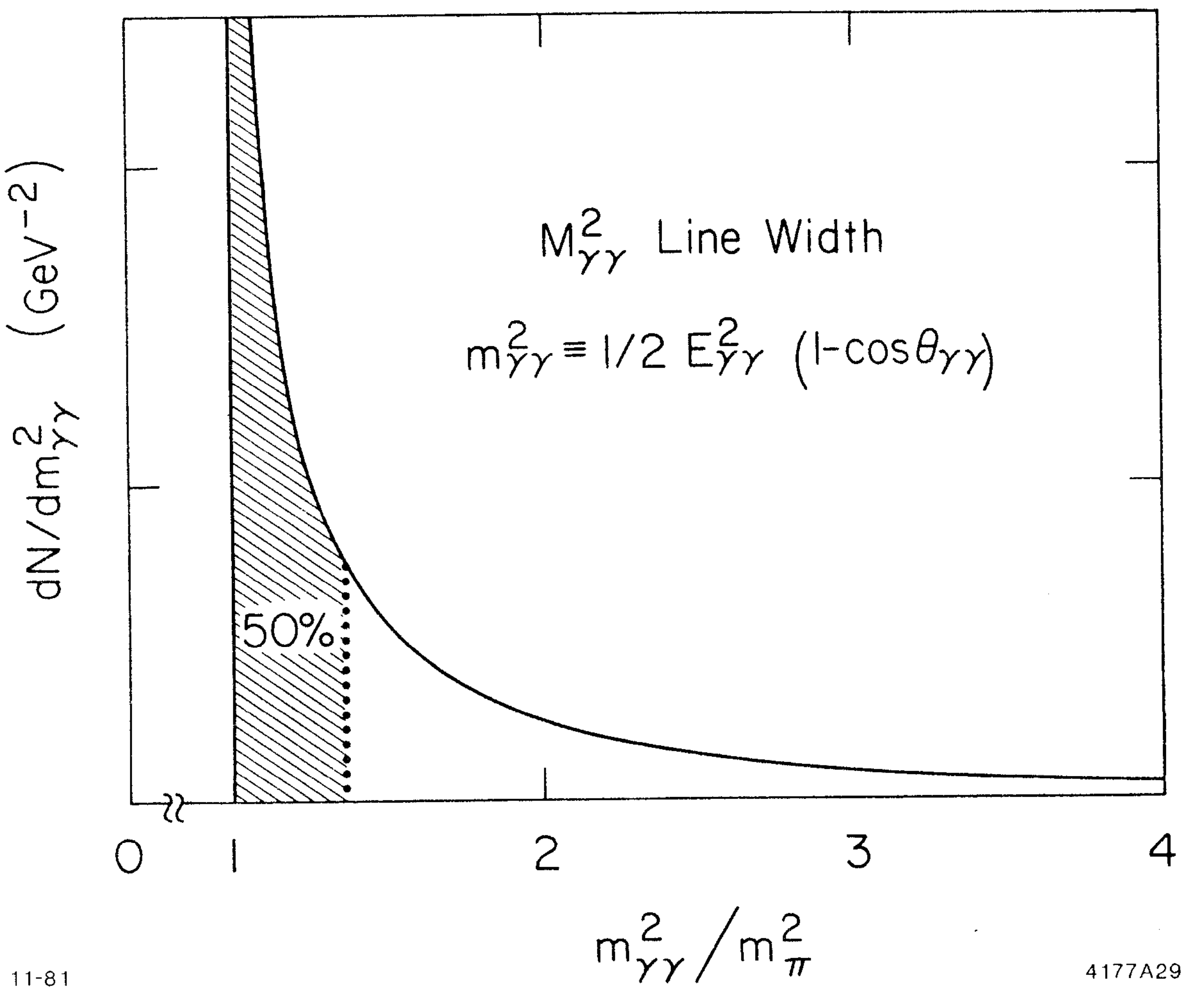

FIG. 9. The photon-photon mass spectrum obtained by using only the total energy of both photons.

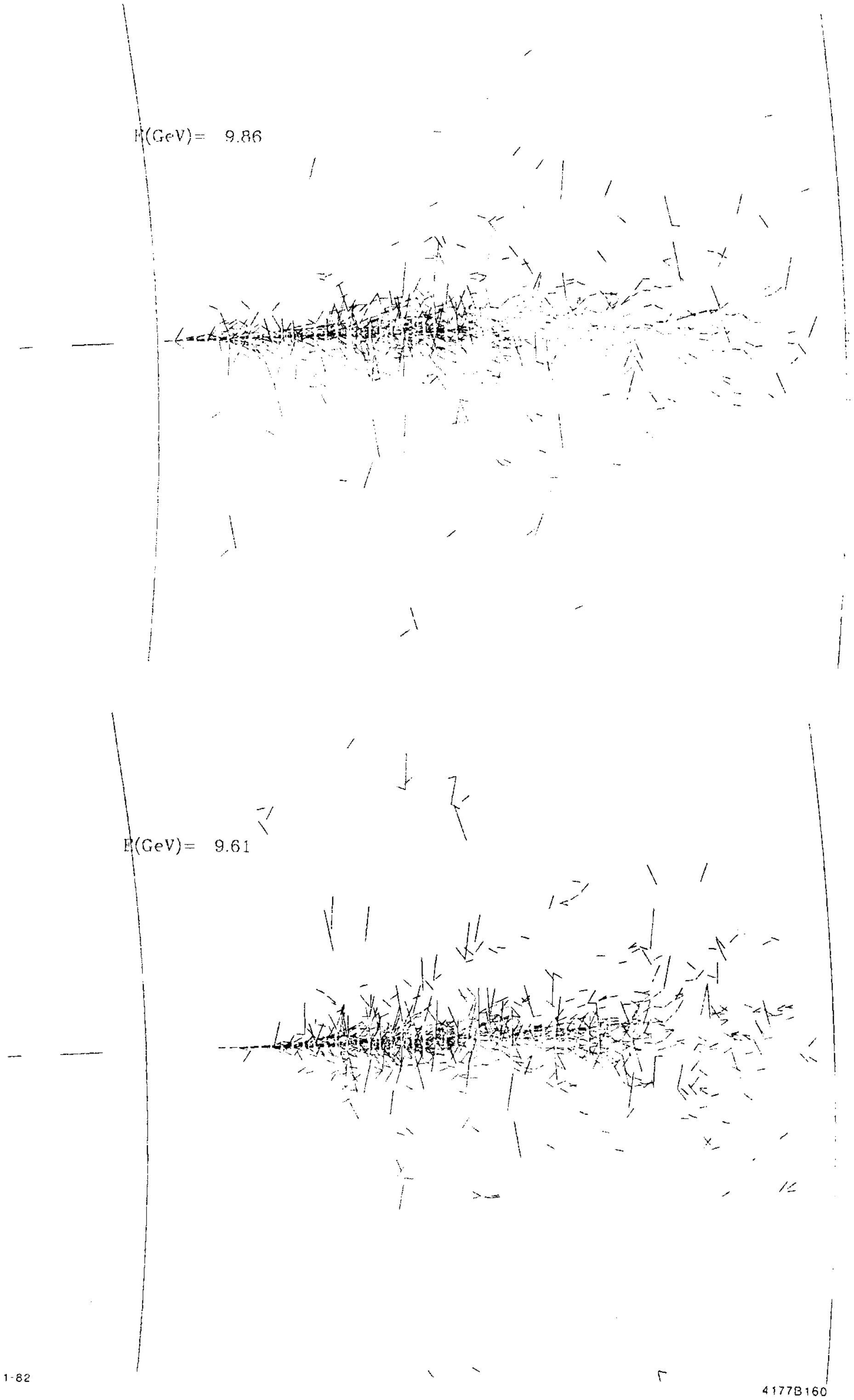

FIG. 10. Two typical showers from the simulation. The model uses 0.3 X_0 per layer with 1 cm gaps. Note the fluctuation in conversion point.

References

1. TUBES Monte Carlo, C.T. Day, SLC Workshop Note.

2. A slightly more efficient calculation of channels in the strip system would not divide the axial strips at the center, yielding $N=8R(3\pi+3)/s$. In this particular example, the axial channels and the ±60° stereo channels were separated electrically at the center of the cylinder; this introduces additional channels, but avoids the possibility of two- of three-jet events sharing ±60° stereo channels which wrap around the cylinder.

IV. PERFORMANCE OF EXISTING DETECTORS

A set of representative detectors at e^+e^- colliding-beam machines has been studied from the viewpoint of applicability at SLC energies. In this evaluation the basic ground rule adopted is that only the present detector configuration be considered: modifications would be discussed only to the extent that they would help in the understanding of deficiencies in the present detector.

Rather than assessing each detector component by component, we consider the representative physics measurements which are the crucial tasks of calorimetry. In this way, for example, detectors which rely on a combination of dE/dx and shower pulse height for electron-hadron discrimination may be fairly compared with ones which use a more purely calorimetric approach.

The measurements considered as bench marks for calorimetric performance are:

* Jet energy flow ,
* Lepton-hadron discrimination, and
* Identification of missing energy due to neutrinos.

A. The MARK II

The calorimeter system of the MARK II consists of 8 barrel modules and 2 endcap modules. The barrel system is an electromagnetic sampling calorimeter with layers of lead serving as the radiator and liquid argon as the active medium working in the ionization mode. The endcaps are a much less sophisticated system, with 2 MWPC readout layers, each behind 2.4 X_0 of Pb. Encasing 60% of the solid angle is a 4-tiered muon identification system, which uses proportional tubes between 8-12 inch layers of iron to perform π/μ separation.

The MARK II at PEP performs well as an energy-flow measuring device. Studies of jets in data and Monte Carlo indicate that 75% of the energy of the jet is measured by the combined drift chamber (for charged tracks) and liquid argon (for neutrals) energies. We conclude from this measurement that the threshold for inferring the existence of a missing neutrino in an event is ≃ 25 GeV at the SLC. The effective calorimetric performance at 14.5 GeV corresponds to a resolution of ≃ 100% $/\sqrt{E}$. To the extent that average momenta do not change significantly in scaling to SLC energies, this is probably a reasonable guess at this time of projected MARK II performance at 100 GeV. This assertion presupposes, of course, that the drift chamber reconstruction is not severely degraded by the higher SLC multiplicities. More likely, however, is a degradation induced by increased pileup and by poorer momentum definition as the momenta increase. The liquid argon performance, aside from minor leakage effects, should be enhanced relative to PEP. The expected angular resolution for jets from Monte Carlo studies is approximately 6°.

The observed performance of the MARK II drift chambers and liquid argon modules appears adequate to do jet physics at the SLC (though as noted above, the drift chamber performance must be further studied). The same conclusion is not warranted for the endcap shower counters, which are inadequate even at PEP energies. Their $50\%/\sqrt{E}$ energy resolution and insufficient depth (4 X_0) allow them presently to be used as a veto for the presence of energy flow towards the endcap region, and also as an aid in the measurement of the full jet energy. Marginal though the quality of the energy measurement may be, an increase of 40% in yield of

3 jet events may be obtained by including the endcaps in the analysis. This gain is affected mostly by the inclusion of more of the event's energy in the measurement, thus allowing more events to survive the jet energy cut.

The MARK II has the capability at PEP of rejecting pions for lepton identification at approximately the 99% level. The factor that might degrade this performance at the SLC is pileup within the detector. While software tricks might be performed with the liquid argon reconstruction programs, it seems likely that for transverse momenta less than 2-3 GeV/c pileup would be untenable and that for larger transverse momenta the PEP performance should be matched.

B. The Mark III

The MARK III shower counters consist of a single cylindrical annulus in the barrel region, together with two endcap assemblies. Performance characteristics of the barrel and endcap are identical. The radiator is 24 layers of 0.5 X_0 lead plates sandwiched between thin aluminum sheets. Gas sampling with 12 mm gap thickness is used. Each layer of the barrel contains 320 cells. On the inner layer the cell size is 25 mm, while on the outer it is 33 mm. The endcap cell size is 27 mm in all layers. Cells in the first 6 layers are individually read out; the outer 18 layers are ganged in groups of three cells in depth. Thin aluminum walls separate the cells. Position along the wire direction is determined by charge division. Thus each cell or cell grouping is read out at both ends. The most notable feature of the Mark III shower counters is their placement inside the coil of the solenoid. This was motivated by the desire for improved detection efficiency for low energy photons.

With 12 radiation lengths in the shower counter, leakage of shower energy would degrade resolution starting at 10-15 GeV. While resolution in the z direction is good (σ = 15 mm), there is a problem with confusion due to multiple hits on a wire. It is, however, possible to add multi-hit capability in z, paying a small penalty in resolution.

The solid angle coverage of the Mark III shower counters is quite complete at 95% of 4π. This is true coverage, in that there are no cracks in the azimuthal direction, and there is complete overlap between the barrel and endcap regions.

The e/π separation has not been measured, but is expected to be rather good for a shower counter in that there is good segmentation both in depth and transverse to the shower. An estimate of the π/e misidentification probability (with 85% electron detection efficiency) is 5% below 0.75 GeV/c, 2% from 0.75 to 2 GeV/c, and 1% or less above 2 GeV/c. In addition, the drift chamber has a dE/dx region in its inner layers which provides an additional 20:1 rejection of pions from 0.3 to 8 GeV/c over 94% of the solid angle.

Knowledge of total energy in an event depends on momentum resolution and angular coverage. The Mark III provides 27 measurements of track position in the xy plane with a resolution of 150 microns, in a 4.4 kG field. This results in a momentum resolution above 0.5 GeV/c of $<0.5\%\cdot p(\mathrm{GeV}/c)$. Full resolution obtains over 75% of 4π, with useful tracking continuing out to 94% of 4π (14 hits in the xy plane). The drift chamber also has multi-hit (4) capability, which would clearly be important in the SLC environment.

There is a time-of-flight system with σ=150 psec resolution at a radius of 1.17 meters, providing 2σ π/K separation to 1.3 GeV/c over 80% of 4π. This is supplemented by the dE/dx region at momenta below 0.7

GeV/c. The muon system, consisting of two layers of proportional tubes with a total of 35 cm of steel, covers 65% of 4π.

The disentangling of jets would be troublesome, just as for the Mark II. Segmentation is a problem for both these detectors, and arises from similar considerations: the multiplicities and angular collimation expected at SPEAR and PEP are not nearly so demanding in regard to pileup as is the expected situation at the SLC.

C. MAC

The electromagnetic calorimeter is a Pb-PWC device, with $0.5X_0$ sampling, and 3 readouts in depth. The azimuthal coordinate comes from parallel wires with a segmentation of 30 mrad. The z-coordinate comes from current division with an accuracy of $\simeq$ 5 cm/layer. The hadronic calorimeter has (in the central region) 24 1-inch plates followed by 3 4-inch plates, interspersed with PWC's with 30 mrad segmentation in ϕ and using current division to give the z-coordinate. The first 24 inches have 2 readouts in depth, and the last 12 inches is read out separately. The endcap hadron calorimeters have 4 longitudinal segments: the first two are more finely segmented to serve also as an electromagnetic calorimeter covering the solid angle missed by the Pb-PWC device. The hadron calorimeter is toroidally magnetized allowing (with drift chambers just inside and outside the iron) muon momenta to be measured with 20% accuracy, limited by multiple scattering. Inside the shower counter is a small solenoid with a 10-layer cylindrical drift chamber giving $\sigma(p)/p^2 = 5\%$ with p in GeV/c.

The MAC calorimeters would perform reasonably well at SLC energies; their depth is still well suited to the 50-GeV/jet environment. Leakage fluctuations would not dominate the resolution until E > 30 GeV (where

σ/E = 3-4%.) In fact, since the electromagnetic calorimeter is backed up by the hadron calorimeter, the "leakage" would be measured, although with a poorer resolution. Because multiplicities are expected to be large, hadron momenta would not grow substantially from PEP energies and leakage from the hadron calorimeter should not be important.

The π/e separation has not yet been measured at PEP so it is difficult to guess what it would be at the SLC. The MARK II achieves <0.7% $\pi \to e$ using information from 3 samples in depth with a device with somewhat better resolution and strips running in 3 directions. In the absence of confusion of overlapping tracks, MAC should be able to achieve similar results with the shower counter alone. However, with strips running in 1 dimension only, it would be much more vulnerable to having >1 particle in a given channel, and so would have difficulty in the cores of jets. On the other hand, the additional information of the hadron calorimeter would help sort out at least those cases in which a photon and a π hit the same strip.

MAC should be uniquely powerful among existing detectors for picking out single muons in hadronic events. In addition to the usual requirements of range and minimal scattering, muons can be required to be minimum ionizing, and the momentum measurements in the solenoid and the toroid can be compared. This should allow pion punch-through to be reduced below the 2% achievable with simpler techniques. Again the single strip direction would cause trouble with overlap of tracks, but less so than in the electromagnetic calorimeter because photons would be absent and many charged hadrons would not reach the back of the calorimeter.

Jet energy flow should be well measured. The expected angular resolution is ≃ 25 mr. The energy resolution would still be 75%/$\sqrt{E}$ even when the large electromagnetic component of hadronic events is considered because of the large fluctuations in how much hadronic energy is deposited in the electromagnetic section. With this resolution, jet energies would be measured with σ/E = 10%, and the center-of-mass energy should be reconstructed with σ/E = 8% giving σ = 8 GeV. Because of the large solid angle and the ability to see neutral hadrons as well as charged hadrons and photons, missing neutrino energy should be visible, at least statistically, at the level of a few GeV.

The clear weakness of MAC for the SLC is its present charged particle tracking. By design, $\sigma(p)/p$ = 80% for 15 GeV particles, which is sufficient to determine the sign of charge at that energy; one would want to meet at least this same criterion at 50 GeV for the SLC.

D. The TPC

The TPC calorimeter system consists of two endcap and six barrel modules, covering about 92% of the solid angle. The end caps have 12.2 X_0 and operate in an MWPC mode. The barrel system has 10.0 X_0 and operates in the Geiger mode.

The primary emphasis in designing the TPC facility was on detailed pattern recognition for photons. This resulted in a strip-channel width subtended from the interaction point of 8-10 mrad for all modules. The reconstructed photon angular resolution is about 3 mrad at 1 GeV, and scales roughly as 1/$\sqrt{E}$.

The strips are arrayed projectively, to increase the power of the pattern recognition algorithms. A 3-fold redundancy of the pulse height in each layer is achieved by measuring the signal on the wires and the induced cathode signals on opposite sides of the gap. At energies of several GeV these features result in high photon detection efficiency with good energy and position resolution.

At higher energies the shower counters start to suffer from leakage fluctuations out the back and from multi-track saturation of the Geiger cells. These effects become noticeable at 6 GeV, and by 10 GeV σ/E has leveled off.

The e/π separation is thought to be not much better than 10%, due to the shallow depth. However, when used in conjunction with the dE/dx capability of the TPC, an overall rejection of pions at the 0.1% level is expected.

Energy flow analysis should be good due to the fine segmentation, but limited ultimately by gross energy resolution as stated above. Jet counting should be good, again due to the fine granularity.

E. The HRS

The HRS has no hadronic calorimeter, and has as yet no experience with using tracking plus an electromagnetic calorimeter to measure total energy. Tracking is very good over 80% of 4π. The uncertainty in total energy would come from particles at small angles. The uncertainty in jet energies would come from fluctuations in the energy going to neutral hadrons and neutrinos: σ/E should be $\simeq 0.1$ or 0.2. The 4-ft iron thickness just outside the coil precludes the addition of a hadron calorimeter.

The barrel electromagnetic calorimeter is inside the coil, but has been made rather simple in order to maximize space for tracking. The Cerenkov counters allow about 25 cm expansion inward, but the outer drift chamber would have to be removed or replaced. The endcap calorimeter is also simple, but it does have room to expand. A highly segmented wire chamber front end is planned.

The HRS calorimeters are thin in radiation lengths (11) and would have significant leakage at high energies. Segmentation is low so there might be difficulty separating particles in high multiplicity jets. Photons in jets could be identified by correlating PWC hits with tracking, but energy measurement would usually be impossible. The detector should adequately determine the number of jets and measure the energy of whole jets. It would do a good job with low multiplicity events such as $e^+e^- \to Z^0+\gamma \to \gamma\nu\nu$ with a 1 to 5 GeV γ, or $Z^0 \to \gamma$ + Higgs or $Z^0 \to e^+e^-$ + H.

The table below summarizes some of the relevant detector characteristics for the detectors considered.

Properties of Some Existing Electromagnetic Calorimeters

Detector	Energy resolution at 1 GeV (σ/E, %)	$\delta\varphi$ (mrad)	$\delta\theta$ (mrad)	Depth (X_o)	π/e rej. (% punch-through)	Solid angle (% of 4π)
Mark II	12	4	4	15	1	70
(Endcap)	(50)	(11)	(6)	(5)	(10)	(15)
TPC	10-11	2	2	10-12	10(a)	90
Mark III	17	3	10	12	1(b)	95
HRS	16	5	8	11	1	60
(Endcap)	(20)	(6)	(6)	(11)	(3)	(25)
MAC (EM)	18	14	25	16	1	80
MAC (Had)	75	50	50	$5.4\ \Lambda_{abs}$	1(c)	97

(a) A multiplicative factor of 0.01 is expected from the TPC as well.

(b) The dE/dx region provides another factor of 20 rejection.

(c) This is the appropriate punch-through for π/μ discrimination.

V. CALORIMETER TECHNOLOGIES

Current technology permits a great variety of competing approaches to calorimetry, both for electromagnetic and for hadronic showers. Spatial resolution, energy resolution, mechanical and chemical stability, geometric adaptability, ease of readout, compactness, and overall cost are boundary conditions, in addition to the general requirements of reliability and ease of operation. Table I shows that the detectors presently in place at e^+e^- storage rings span only a small part of the broad spectrum of possibilities.

A. Ten Techniques

In the following, a few basic characteristics are mentioned concerning a number of new techniques for cascade generation, energy sampling, and readout that may have a strong impact on the next generation of calorimeters.

1. Compensating Absorbers: Uranium, U-Cu Compounds[1,2]

The accuracy of hadron calorimetry is limited by the energy lost in nuclear cascades to nuclear binding energies or to escaping neutrons and neutrinos. Fluctuations due to these losses have been shown to be compensated by the exploitation of nuclear fission effects in uranium. Depleted uranium-238 has been used as an absorber in conjunction with liquid argon and with scintillator material as radiators.

Secondaries of the nuclear fission component have a tendency to over-compensate for the lost energy, so that electrons will apparently deposit less energy in a calorimeter than pions of the same momentum. In recent studies hybrid devices, incorporating a mixture of uranium and Cu or Pb plates, have been demonstrated to be useful in restoring the balance.

TABLE I

PRESENTLY EXISTING DETECTORS, AT e^+e^- ($\bar{p}p$) MACHINES: CALORIMETER TYPES

ACCELERATOR	DETECTOR	ELECTROMAGNETIC CALORIMETER TYPE	INSIDE COIL	HADRON CALORIMETER TYPE	REMARKS
SPEAR	CRYSTAL BALL	NaI	No Coil	-----	Minimal Tracking.
	MARK III	Pb-PWC Sandwich	Yes	-----	Endcaps Same.
PEP	MARK II	Liquid Argon	No	-----	Presently no Liquid Argon Endcaps.
	MAC	Pb-PWC Sandwich	No	Fe-PWC Sandwich	Limited Tracking.
	TPC	Geiger-Mode Tubes, Segmented by Nylon Threads, Between Heavy Laminate	No	-----	Small-Angle Coverage From PEP-9; Intermediate-Angle Endcaps: PWC-Pb
	HRS	Segmented Pb-Scint. + PWC	Yes	-----	Endcaps Same.
	DELCO	Pb-Scint., Sandwich, BBQ	No		Thin Endcap Energy Tag.
CESR	CLEO	Crossed Proportional Tubes/ Lead Sandwich	No	-----	Endcaps Similar To Barrel.
	CUSB	NaI + Pb Glass	No Coil	-----	Little Tracking.
DORIS	ARGUS	Pb-Scint. Sandwich, BBQ	Yes	-----	Endcaps Same.
PETRA	PLUTO	Pb-Scint. Sandwich	Partly	-----	New $\gamma\gamma$ Endcap Coverage.
	TASSO	Liquid Argon Towers	No	-----	Endcaps Same.
	CELLO	Liquid Argon, Strip Geometry	No	-----	Endcaps Same.
	JADE	Pb Glass	No	-----	Pb Glass Endcaps.
	MARK J	Scint./Pb Sandwich	YES	Fe-Scint Sandwich	Limited Tracking, Magnetized Iron In Hadrometer.
FOR COMPARISON:					
SPS COLLIDER ($\bar{p}p$)	UA-2	Pb-Scint Sandwich, BBQ	No Coil For Most Of Solid Angle.	Fe-Scint Sandwich, BBQ	Strict Tower Geometry, Very Limited Tracking.
	UA-1	Pb-Scint Sandwich, BBQ	YES	Fe-Scint Sandwich	Hadrometer Integrated Into Dipole Magnet Iron.

The advantages include the compact design afforded by the short radiation length of 3 mm for uranium, and the possibility of combining electromagnetic and hadronic calorimeters. The disadvantages are in the uncertain availability of the uranium and that the machining and fabrication costs can be very high. The effect of compensation on calorimetry is discussed in part B of this section, and more information on construction with uranium is given in VI C.

2. New Extrusions[3,4]

A number of technical developments may make sampling-gas-detectors (or liquid scintillator detectors) easier to build and more economical. Mixtures of equal volumes of metal and metal oxide powders (e.g. Pb and PbO) with some acrylic make a slurry that can be poured into molds of any desired shape. Upon hardening, these serve as an absorber for integrated calorimeters with drift tube insertions. Cathode strips can be applied at 90° with respect to the anode wires; charge division would provide similar information.

In another approach plastic extrusions or moldings (linear arrays of rectangular tubes with 1.6 mm wall thickness based on 300 Angstrom diameter carbon particles) yield resistivities of up to 10^5 ohms/square; inserted between plane lead absorber sheets, they allow for insertion of cathode pad readout units.

Integrated function or separate-function extrusions can be adapted to many different geometries, are applicable to a variety of techniques from Geiger mode to proportional mode to drift mode, and should result in compact and mechanically stable systems.

3. Filamentary Arrays, Scintillating Fiber[5,6]

Active fibers both permit fine segmentation and transport light towards a photocathode or other recording device. Practical devices include liquid scintillator in a teflon tube and scintillating optical fiber (NE161).

Recent developments make rectangular fibers of ≃ 1.5 mm side dimensions appear reasonable; attenuation lengths of ≃3 m at 430 nm with a light output of about 50% of NE 110 are expected.

Layers of optical fiber between heavy absorbers can clearly lead to good spatial resolution and stereoscopic readout and would be easily placed inside magnetic fields. Readout at both ends would help localization; δx = 2 mm and pair resolution of ≃ 2 cm appear feasible. Good detection efficiency for E_γ greater than 25 MeV would be possible in a thinly layered device. There is little experience in building such devices, especially in an endcap geometry. The long term stability and calibration could be difficult.

4. Long-Distance Drift Arrays[7,8,9]

Sampling calorimeters using charge collection of gas ionization between layers of absorbers can improve segmentation by long-distance drifting of electrons, parallel to converter plates. Large numbers of readout channels are not necessary. Limitations due to high voltage practically available in a compact device may be overcome by operation in a non-saturated drift velocity mode (i.e., 150 V cm^{-1} in 90% Ar, 10% methane). Long-distance drifting demands gap widths on the order of 1 cm. Transverse cell dimensions of ≃ 30 cm or more appear reasonable. Readout by anode wire and cathode pad yields two coordinates, and drift time information gives the third. Spatial resolution is good, with δx = 2 mm and shower separation ≃ 1.2 cm. A wide variety of ganging of wire and pad information is available to reduce the number of readout channels while maintaining desired segmentation. Tower geometry is feasible. Drift field shaping by printed circuit board and low conductance surfaces is non-trivial if loss of charge is to be avoided.

5. Time Projection Calorimeters[10]

This is an application of the time projection chamber (TPC) idea to calorimetry: gas volumes between heavy absorber plates at approximately right angles to the incident particle permit the ionization to drift towards a multi-wire proportional chamber. The anode wire records one dimension; cathode strip readout provides the second coordinate, while drift time measurement gives the third. With an electric field of 40 V cm^{-1} and time windows of 300-500 nsec, $\delta x \simeq 2$ mm. The value of σ/E depends on sampling geometries and can probably approach $20\%/\sqrt{E}$. This technique has mechanical stability, homogeneity, and good pattern recognition. Charge transport efficiency in confined geometries is not easy and limits compactness of the device. Readout electronics and operation in magnetic fields are not trivial.

6. Self-Quenching Streamer Tubes[11,12,13]

One recent development in gas sampling chambers allows the discharges to develop from a Geiger into the streamer mode. If suitable quenching characteristics are devised for limiting the discharge, such techniques have the attraction of yielding large (less than 30 mV) signals into 50 ohms, while maintaining excellent localization ($\delta z \simeq 0.1$ mm). Calorimeters based on these techniques are digital devices (track counting) since the analog information is lost during streamer formation, but high position accuracy and neighboring track separation may make up for this limitation. Risetimes and decay times are on the order of some 50 nsec. The advantages include good segmentation, no need for preamplifiers or analog circuitry, simple construction at relatively low costs, and long-term stability. Track counting leads to saturation effects at high energies where individual tracks become close and non-linearity of the energy response results. It would be difficult to extract stereo information, but charge division might give longitudinal location to one part in 2000 because of the large signal to noise ratio.

7. High-Density Continuous Samplings: BGO[14,15,16]

Continuous sampling is always superior to discontinous viewing of shower build-up and decay. Bismuth germanate (BGO) has a number of attractive features that mark it as a potential successor to NaI as a compact detection device for electromagnetic showers: high-density (ρ = 7.13 g cm^{-3}), high refractive index (n = 2.13), and short radiation length (X_0 = 1.13 cm). Optical properties and radiation resistance are not yet well established, but light output is only equivalent to 1/10 of NaI. The light attentuation depends on purity: for typical samples the attentuation length ≃ 20 cm at λ = 480 nm. A BGO device would be very compact, rugged and chemically stable and non hygroscopic with an excellent energy resolution of $0.2\%/E^{.25}$ for $E \geq 1$ GeV. The costs are high, but are not yet firmly established. Such a device would have limited time resolution (risetime is equivalent to 50 nsec , fall time to 300 nsecs), a temperature dependence of 1.7%/°C, and limited e/π rejection and tracking possibilities.

8. Planar Spark Counters[17,18,19]

In this technique, developed in Novosibirsk, a spark discharge occurs between highly resistive ($10^{10}\ \Omega$ cm) electrodes in a very absorptive gas mixture such as argon or neon plus various organic admixtures.This leads to excellent time definition and spatial resolution of individual tracks. For a 0.1 mm (1 mm) gap width, 12 atm (1 atm) gas pressure, δt = 28 psec (300 psec) and δx = 0.3 mm have been reached. There is no need for preamplifiers; one volt signals into 50 ohms are easy to obtain. Neighboring spark resolution limits the application in calorimetry, where spark counting provides the basis for energy definition.

The device (multi-layer) has a recovery time of 10 to 50 msec in a 3 mm region surrounding a given spark , but is continuously active. The fabrication from very flat electrodes of conductive glass is expensive; local dead-time is non-negligible; and there would be the problem of saturation at high energy common to spark counting devices.

9. BBQ For Light Collection and Segmentation[20]

The technology of sampling calorimeters has been enormously improved by the development of wave bar readout systems. Layered devices involving scintillator and absorber can be read out by BBQ-doped acrylic strips which collect light from different layers and bring it to a photocathode in back of the device. Recent developments make longitudinal segmentation possible through the use of different wavelength shifters for different segments of the calorimeter; fluorescent converters emitting yellow (590 nm) or red (630 nm) light have been used to separate the hadron and electromagnetic parts of a calorimeter. Optical cross talk between different optical components is unavoidable, but can be suppressed to the few % level. Calibration of absorption lengths must be established for different components.

10. Microchannel Plates[21]

Precise localization information can be obtained by the use of large arrays of minuscule photomultipliers, called microchannel plate tubes. In a basic version capable of a multiplication of $\simeq 10^3$, these are glass plates perforated by tiny tubes with an electron-multiplying coating acting like an image intensifier. Fancier versions with bent tubes have gains of up to 10^6. Within one tube the information is saturated (track counting), but spatial resolution is typically about 10 nsec for this stage alone. Commercial products are available for the elements.

The costs of fabrication and readout are prohibitive for the time being; ganging of neighboring layers of sampling calorimeters is not straightforward; and presently available products deteriorate with age and radiation exposure.

B. Compensation in Hadron Calorimetry

One attraction of hadron calorimetry at SLC is the quite respectable total-energy resolution possible at these high energies: for example, a "standard" $75\%/\sqrt{E}$ device would give $\sigma \simeq 7.5\%$ for $E \simeq 100$ GeV. To achieve such resolution in actual practice, with multi-hadron events in a large detector, it is of course necessary to add up all the bits and pieces of the measurement with the right energy calibrations. Here a problem may arise because:

- a hadron calorimeter is always preceded by an electromagnetic shower detector;
- such a shower detector will absorb all the energy of photons from π^0 decay (approximately 25% of the total at PEP/PETRA energies) and, in addition, a substantial fraction of the remaining energy (up to 50% depending on the absorption lengths involved) mainly in

the form of low-momentum hadrons; and

- such a device may have a much different response to a unit of energy absorbed in a hadronic shower as compared with an electromagnetic shower. (For example, in a lead plate device the fraction is roughly one-half, and is momentum dependent.)

The net effect could be that the fluctuations in total response, due to the fluctuations in the relative amounts of energy deposited in electromagnetic and hadronic showers, will dominate the overall energy resolution.

At least two solutions may be considered:

(1) If most of the higher-energy π^0's in an event can be identified and their energy deposition separated from that of other particles, separate calibration constants can be applied. This may not be feasible in the tight, dense jets expected at SLC energies.

(2) Devices using uranium as the showering medium have been shown to give a response to hadron showers very close to that for electromagnetic showers, almost eliminating the root of the problem. Furthermore, use of uranium in the electromagnetic shower region minimizes the absorption lengths for a chosen number of radiation lengths, thereby minimizing the energy absorbed in this region from hadrons other than π^0's.

References

1. C. W. Fabjan et al., N. I M. 141, 61 (1979).

2. O. Botner, Physica Scripta 23, 555 (1981).

3. H. A. Gordon, S. D. Smith, Proc. SLAC Summer Inst. (1980).

4. M. Atac, Mashima, et al., FNAL- KEK Coll., Fermilab CDF-94 (1981).

5. S. R. Borenstein, R. B. Palmer, R. C. Strand, BNL 28195 (1980); BNL 28546 (1980).

6. D. Perrin, P. Sonderegger, CERN Note DM/SPS/81-7 (1981).

7. L. E. Price, Physica Scripta 23, 685 (1981).

8. L. E. Price, I. Ambats: IEEE NS28, 506 (1981).

9. C. A. Heusch, S. Shapiro, Y. Zhu, SCIPP note in preparation (1981).

10. H. G. Fischer, D. Ullaland, IEEE Trans. Nuc. Sci., NS-27. 38 (1980).

11. G. D. Alekseev et al., N.I.M. 177, 385, (1980).

12. Battistini et al., N.I.M. 164, 57 (1979).

13. M. Atac, A. V. Tollestrup, D. Potter, Fermilab Note FN 339 (1981).

14. D. Coyne, M. Cavalli-Sforza, SLC Workshop Note No. 34, (1981).

15. M. Cavalli-Sforza, CESR-II Workshop Notes CNLS81-490 (1981).

16. G. Blanar, H. Dietl, E. Lorenz, F. Pauss, H. Vogel, MPI-PAE/EXP E1/94 (1981).

17. Yu, Paestov et al., SLAC translation #184 (1978); SLAC Seminar (1981).

18. W. B. Atwood in: Proc. SLAC Summer Inst. (1980).

19. R. Santonico, R. Carderelli, N.I.M., 187, 377 (1981).

20. V. Eckardt, R. Karbach, A. Manz, K. P. Pretzl, N. Schmitz, D. Vranic, MPI-PAE-Exp. E1 (1978).

21. See the specification sheets of commercial manufacturers, such as Hamamatsu and Amperex (Philips).